CHALMERS
UNIVERSITY OF TECHNOLOGY

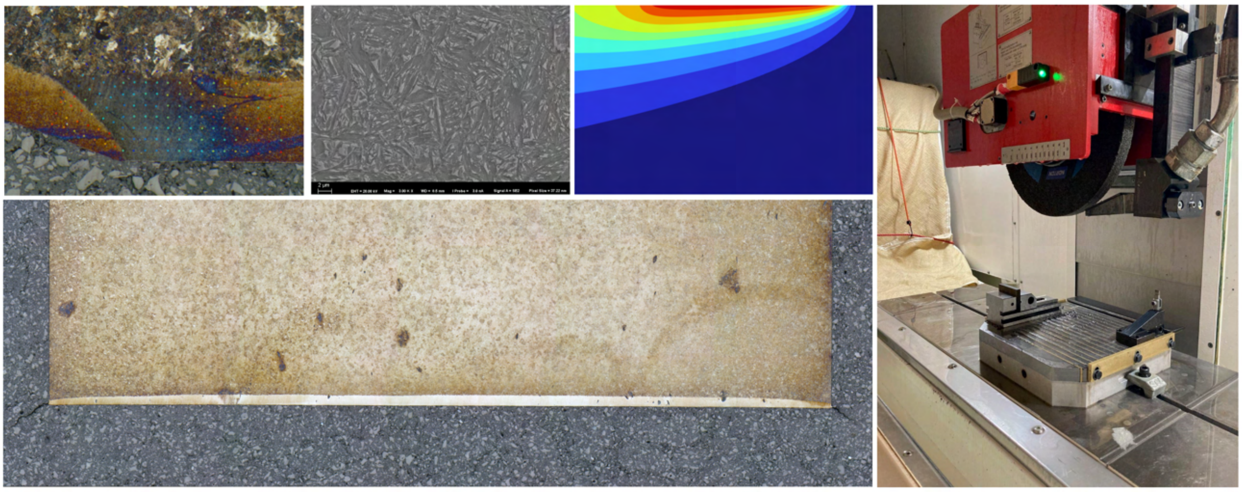

Rail Grinding Study

Laboratory Experiments, Metallography and Modelling

Master's thesis in Materials Engineering & Applied Mechanics

MARIA BÖRJESSON
PER EMANUELSSON

DEPARTMENT OF INDUSTRIAL AND MATERIALS SCIENCE

CHALMERS UNIVERSITY OF TECHNOLOGY
Gothenburg, Sweden 2024
www.chalmers.se

Master's thesis 2024

Rail Grinding Study

Laboratory Experiments, Metallography and Modelling

MARIA BÖRJESSON
PER EMANUELSSON

Department of Industrial and Materials Science
Division of Engineering Materials
Chalmers University of Technology
Gothenburg, Sweden 2024

Rail Grinding Study
Laboratory Experiments, Metallography and Modelling
MARIA BÖRJESSON
PER EMANUELSSON

Supervisor: Erika Steyn, Industrial and Materials Science
Examiner: Johan Ahlström, Industrial and Materials Science

Master's Thesis 2024
Department of Industrial and Materials Science
Division of Engineering Materials
Chalmers University of Technology
SE-412 96 Gothenburg
Telephone +46 31 772 1000

Cover image, clockwise: Optical microscopy image along with plotted hardness results, scanning electron microscope image of martensite, moving heat source simulation, set up of specimen in grinding machine, cross-sectional sample with a martensite layer.

Typeset in LaTeX
Printed by Chalmers Reproservice
Gothenburg, Sweden 2024

Rail Grinding Study
Laboratory Experiments, Metallography and Modelling
MARIA BÖRJESSON
PER EMANUELSSON
Department of Industrial and Materials Science
Chalmers University of Technology

Abstract

During maintenence grinding of pearlitic railway, the microstructure of the rails' surface layer can transform into martensite. This can have detrimental effects, such as crack formation, due to the brittleness of martensite. To investigate this phenomenon, an industrial grinding machine was used to grind the surface of specimens extracted from rail heads of two different rail grades. These were subsequently examined to see how different grinding parameters contribute to the martensite formation. Among other things, the thickness of the martensite layers was measured, the shape of the layers was examined and hardness in the heat affected region was measured.

The main takeaway from this study was that the thickness of the martensite layers decreased with an increased feedrate caused by the shorter contact time between grinding wheel and surface at higher feedrates. This motivates using a high train speed during railway grinding in-field. Several additional discoveries were made during examination. Surface discoloration correlated to different feedrates was found on the ground specimens' surfaces. A slight fluctuation in martensite layer thickness along the grinding direction was discovered and deemed to be caused by oscillations of the grinding wheel with each revolution. Tests also revealed that the difference in hardness between martensite layers formed in the two different rail grades was smaller than the initial hardness difference of the original pearlitic microstructures. Simulations of the process were made using the finite element method and analytical formulas, in an attempt to estimate the martensite layer thickness. This proved difficult and could only be done by tuning of the energy input to match the computed martensite thickness with the experimentally measured thickness. Further research is needed to predict the martensite layer thickness.

Keywords: grinding, rail, railway, martensite, pearlite, tempered martensite, hardness, finite element analysis, white etching layer (WEL)

Acknowledgements

This work is a part of the activities within the center of Excellence CHARMEC. They are funded within the European Unions's Horizon 2020 research and innovation programme in the Shift2Rail project In2Track3 under grant agreement No. 101012456 and in the Europe Rail project IAM4RAIL under grant agreement No. 101101966.

We had an amazing time working on this project and are grateful for getting to learn so much while having fun in the meantime. Many need to be thanked for the support we received along the way. Voestalpine and Trafikverket, for providing the rail samples for the project. Our supervisor Erika Steyn, who helped us with everything from SEM to the most arbitrary questions deserves all the praise she can get. Thank you for all the help and encouragement! Philipp Hoier, who performed all the grinding tests has been invaluable and a pleasure to work with. Peter Krajnik, whose extensive knowledge of grinding helped us greatly. Antonio Mulone, who trained us to use the laboratory equipment. A special mention also goes out to everyone who contributed to such a friendly environment at Chalmers during our time working on the thesis. Finally, we are so happy to have had Johan Ahlström as our examiner. Thank you for this opportunity, your enthusiasm and your guidance throughout the project. It means a lot to us.

Maria Börjesson, Per Emanuelsson, Gothenburg, July 2024

List of Acronyms

Below is the list of acronyms that have been used throughout this thesis listed in alphabetical order:

BCT	Body-Centered Tetragonal
BEL	Brown Etching Layer
CCT	Continuous Cooling Transformation
FCC	Face-Centered Cubic
MGT	Mega Gross Tonnes
OM	Optical Microscope
RCF	Rolling Contact Fatigue
SEM	Scanning Electron Microscopy
WEL	White Etching Layer

Nomenclature

Below is the nomenclature of indices, sets, parameters, and variables that have been used throughout this thesis.

θ	Temperature change
k	Thermal conductivity
l	Half of contact length
q_w	Heat flux per unit area
u	Distance along the contact length
v	Feedrate of the workpiece
x	Coordinate in the workpiece in the grinding direction
α	Thermal diffusivity
K_0	Modified Bessel function of second kind of order 0
z	Coordinate in the workpiece down into the material
Cp	Thermal conductivity
ρ	Density
l_c	Contact length
a	Depth of cut
d_e	Equivalent diameter
Q_t	Total grinding power
Q_i	Idle grinding power
Q_g	Grinding power
A	Contact area
ϵ	Heat partition
E_e	Average specific energy
w	Width of workpiece
E_e	Contact area specific energy
q	Heat flux
∇T	Temperature gradient
m, n	Solution indices
i	Index for numerical integration
j	Index for heat step
$c1$, $c2$, $c3$, $c4$	Constants for heat flux distribution
d_m	Measured martensite depth
d_a	Calculated martensite depth
d_{me}	Estimated martensite depth
Q_{ga}	Adjusted power
$_a$	Adjusted heat partition

Contents

List of Figures

List of Tables

1

Introduction

1.1 Background

Rails are during their lifetime subjected to damage-inducing load and wear from the passing trains. To remove surface damage and restore the rail to its original condition and profile, maintenance is required. Grinding is one of the common maintenance methods. The goal of the operation is to remove detrimental features close to the surface of the rail head. This includes cracks induced by rolling contact fatigue (RCF). The procedure is performed by a train equipped with multiple subsequent grinding stones that run on the railway [1] p. 72. However, by grinding, there is risk of changing the microstructure of the material closest to the surface. Pearlitic steel is commonly used for railway rails [2] [3]. Most of the energy input in the grinding operation is transformed to heat, which raises the temperature of the outermost layer of the rail enough to cause phase transformation from pearlite to austenite. Due to the ambient temperature, the material is thereafter cooled down at a fast rate. Rather than transforming back into the original pearlitic microstructure, the rapid cooling causes the formation of martensite, a harder and more brittle microstructure than pearlite. If a crack initiates in the martensitic layer and propagates into the pearlitic structure, it can cause severe damage. Depending on different grinding parameters such as the speed of the grinding train and the amount of removed material in one pass, the depth of the heat affected zone is expected to vary, along with other properties, like surface roughness. This is important to consider, as these properties also affect the quality of the railway [1] p. 66.

1.2 Objectives

This project mainly aims to investigate how grinding affects and changes the microstructure of two common rail grades, R260 and R350HT, depending on the parameters of depth of cut and feedrate. To achieve this, test specimens of both grades will be ground in an industrial grinding equipment, set to mimic on-site grinding, and subsequently analysed by microscopy, with additional tests carried out to determine the characteristics of the microstructure close to the ground surface. Among other things, the depth of the outermost layer of the ground specimens, where the material properties are expected to change, will be examined.

In order to see how changes in grinding parameters affect the outermost layer without having to do expensive and time-consuming tests, a finite element model will be made and verified with the tests from the lab. The finite element model can be used to investigate other effects of grinding that are more difficult to study in the lab environment.

The concrete goals for this project are to
- Investigate the formation and appearance of a thermally induced martensitic layer caused by grinding, in two rail grades, R260 and R350.
- Determine how the depth/thickness of the martensitic layer depends on different grinding parameters.
- Compare the behaviour and properties of the different rail grades, in relation to grinding.
- Investigate how the depth of the martensite layer can be estimated using finite element method.
- Investigate how subsequent runs, overlapping adjacent surfaces affect the intermediate region.

1.3 Delimitations and limitations

The project's delimitations, which describe choices made to narrow down the scope of the study, and the limitations concerning available equipment and processes are listed below.
- The study specifically investigates the behaviour of pearlitic rail steel.
- During this study, it is assumed that the martensitic transformation is caused by thermal effects only.
- Grinding will be performed in a laboratory, instead of in the field. The process conditions and parameters will therefore be limited to the capacity of the available grinding machine.
- Each specimen will be subjected to grinding in only one laboratory session. Therefore, the study will not include research on how the rail is affected by multiple iterations of grinding in a long-term perspective.
- For the finite element method, the grinding power will be replaced by a heat flux instead of simulating the material removal.

2

Theory

2.1 Rail damage

2.1.1 Rolling contact fatigue

Rails are subjected to mechanical loads by the railway traffic and transport, and different types of damage can emerge as a consequence of this. This can include damage such as corrugation, wear, and RCF.

RCF is a term for rail damage caused by the stresses induced by wheel-rail contact and cyclic heavy loads. This leads to, among other things, head checks and squats. Head checks are caused by micro-cracks that gather up, ultimately leading to material breaking off. Squats are another type of crack defect [1], p. 25-26. In the case of squats, cracks initially propagate in the subsurface of the rail but eventually grow downwards, potentially causing rail fracture [4].

2.1.2 White etching layers

The wheel-rail contact in pearlitic rails can cause changes in the microstructure around the contact area. The changed microstructure is often referred to as white etching layers (WEL). This term is used because during optical microscopy of these regions, they appear bright due to the light reflecting back from the smooth surface which has remained unaffected by etching.

In one study, a comparison was made between the microstructure of WEL found on initially pearlitic R260Mn rail field samples and that of specimens of the same material which had been heat-treated in a laboratory setting to produce martensite. The results indicated that the WEL found on the rails also consisted of martensite [5]. R260Mn differs slightly from the common R260 rail grade, which will be one of the grades examined in this report. The main difference is the higher Mn-content in R260Mn compared to R260. In solid state, the Mn-content range is 0.65-1.25 wt% in R260 and 1.25-1.75 wt% in R260Mn. The two grades lie within the same hardness range, 260-300 HBW [6]. R260Mn is used to facilitate welding and R260Mn rails exhibit lower residual stress than R260 rails [7]. Simulations in JMatPro based on their chemical compositions [6] show that the A_1 temperature of R260Mn is around 5 degrees lower than that of R260. The differences between R260 and R260Mn should not significantly affect their abilities to form martensite.

Another study on rail steel found that WEL, referred to as a white phase, are caused by thermal effects. Cracks were discovered in the white phases [8]. One study also suggests that cracks are prone to developing in WEL early in the rail's life [9]. If the surface microstructure changes from pearlite to martensite, the region would likely become more prone to cracking, as martensite is more brittle than pearlite. With time, cracks can propagate through the material due to the cyclic loading effect on rails, eventually causing fracture. Removing the cracks completely at an early stage would eliminate the risk of this scenario.

2.1.3 Effects of maintenance

Rail maintenance is essential to maintain a safe railway and is expected to be performed regularly enough to prevent critical damage. Common methods are grinding and milling of the rail surface [10]. Maintenance is performed to remove cracks, WEL and restore the rail profile. However, it is important to note that WEL can be caused by the grinding operations themselves. One study investigated WEL formation after in-field grinding on new rails of three different rail grades, including R260 and R350HT. It was found that WEL of varying thickness were present on all grades [11].

2.2 Grinding

2.2.1 Railway grinding

Based on 16 responses to a questionnaire sent to infrastructure managers of railways, rail grinding was revealed to currently be the most common preventive maintenance procedure for rail reprofiling [12]. Among other things, it is performed to remove defects stemming from RCF and to restore the rail geometry [13].

Grinding of rails is carried out by specialised grinding trains equipped with multiple rotating grinding stones with different inclinations [1], p. 72. The number of grinding passes required per maintenance cycle varies [14].

During rail grinding in field, the rotating grinding stones usually have a perpendicular rotation axis in relation to the rail surface (face grinding). Since this method is more common [10], the following theory described will mainly apply to this method. However, during the laboratory study this method is not used, instead a grinding wheel with a parallel rotation axis (peripheral grinding) is employed, as the available grinding equipment only permitted this. Figure 2.1 shows the orientation of the wheel in relation to the surface for the different methods.

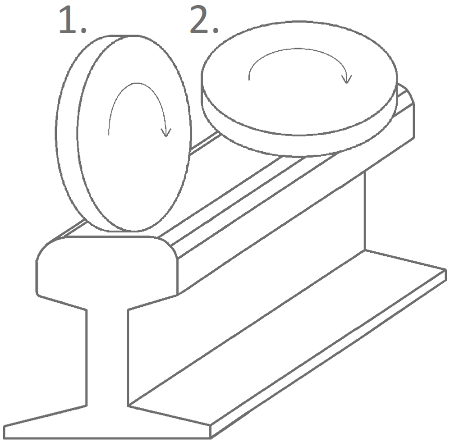

Figure 2.1: Depiction of how peripheral grinding (1) and face grinding (2) is performed.

Based on examples from literature, approximately 47 m/s can be regarded as a common peripheral speed for grinding stones [1], p. 58. The velocity at which the grinding trains travel along the rail differs, but is typically in the range of 3-15 km/h [10]. High speed grinding is a newer concept, with grinding train speeds in the range of 50-80 km/h [10]. This method is also associated with a shallow grinding depth of cut [1], p 173.

The thickness of the layer to be removed during reprofiling, is another parameter that can be adjusted to achieve optimal results. According to the European standard EN 13231-5, this is decided by the infrastructure managers [10]. However, the standard also suggests a maximum and minimum depth in the centre of the rail head of 0.2 and 0.1 mm, respectively. At the critical gauge area, which is the area of the rail in contact with the train's wheel, 0.6 mm can be removed.

The intervals between maintenance operations are often measured in mega gross tonnes (MGT), which can be defined as the total accumulated weight of the passing rail traffic. Grinding intervals vary and can range between 45 and 60 MGT for tangent (straight) tracks, with shorter intervals of 15 to 25 MGT for curves [12]. While the standard suggests that longer intervals typically can be employed for the harder R350HT grade than for R260 [10], the grade type is not considered in practice [12].

Different approaches exist for determining when and how grinding should be performed. Two strategies often used are "corrective grinding" and "preventive grinding". So called corrective grinding is typically performed with long intervals, where grinding is employed to remove defects which have developed over that time period. To ensure the removal of all defects, a relatively thick layer of material must be ground away, by several grinding passes [1]. The increasingly used strategy preventive grinding is instead performed to hinder any defects at the initiation stage [1] and is performed with less material removal than typically needed for corrective grinding. Preventive grinding is the recommended method for controlling RCF [14].

For preventive grinding, a shallow depth of cut of 0.05 mm is suggested, for one pass. This is sufficient if the grinding intervals are short, such as 15 MGT in sharp curves [1] p. 259. In conclusion, it can be stated that the depth of cut needs to be enough to remove all defects, while not removing excessive material.

In order to maintain the rail profile, the grinding stones are mounted with different angles, thus producing several facets along the rail head. Figure 2.2 shows a depiction of how different grinding wheels would be angled at the gauge corner of a rail head. To pass visual inspection, the maximum allowed width of the facets are 4, 7 and 10 mm on the gauge corner, shoulder and near the rail crown, respectively [15].

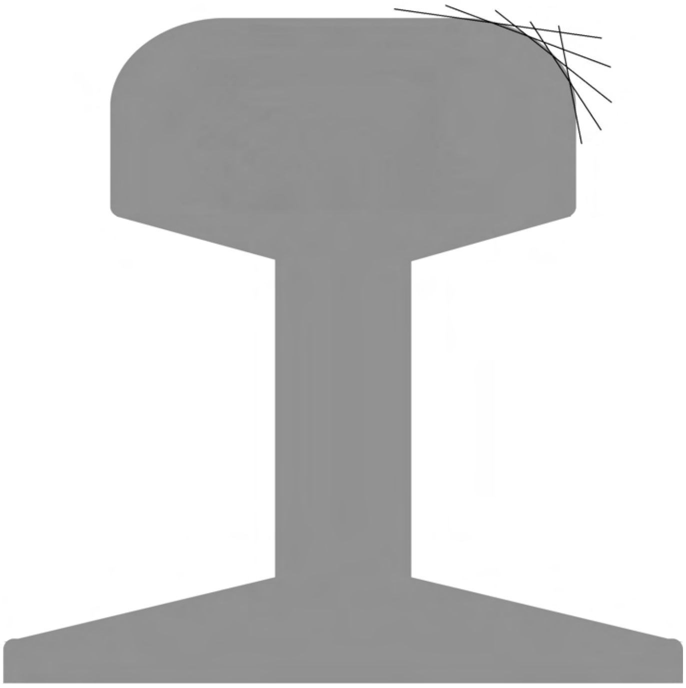

Figure 2.2: Theoretical images of how the curved angles are made.

Other aspects of surface quality are also inspected after grinding has been carried out. Continuous bluing on the surface is not acceptable [15]. Bluing is a type of thermal damage.

2.2.2 Laboratory grinding

When investigating effects of grinding, the study can benefit from implementing it in a laboratory environment, in addition to a field study or on its own. The laboratory provides a controlled environment for experiments. This includes temperature, humidity and grinding parameters. It can also facilitate recording certain aspects of the procedure, such as power used. Additionally, it eliminates the need for disrupting regular traffic and transporting grinding equipment and personnel to site, thus saving in on costs.

On the other hand, potential limitations may arise from having to adapt to the capacity of the available laboratory equipment. This can include only being able to grind small specimens of the rails, or not being able to emulate high speed operations. This could lead to the results not being fully translatable to real scenarios.

Parameters that can easily be changed in a laboratory grinding machine include the peripheral velocity of the wheel (wheel speed), the velocity at which specimen moves across the table (feedrate) and the designated thickness of the layer which is to be removed from the surface in one pass (depth of cut). The inclination of specimens can also be adjusted, if needed, to mimic facet grinding.

2.3 Rail materials

Rails are made of steel, typically with a pearlitic structure. Pearlitic steel has a high resistance to wear and plastic flow, making it a suitable material for rails [16]. Several different pearlitic rail grades exist. The ones used in this study are R260 and R350HT, which are both among the most commonly used rail grades [2] [3]. The chemical compositions of the respective grades, which have been used for simulations in this study, can be found in Table 2.3. The presented compositions are based on the maximal allowed content of each element as stated in European Standard EN 13674-1:2011+A1:2017 [6]. It should be noted that the compositions will in reality differ slightly. The chemical compositions of R260 and R350HT are very similar. The important difference between the two is instead that R350HT is head hardened. Head hardening is a method where the hardness of the rail head is increased through a heat treatment in which a finer pearlitic structure is produced by accelerated cooling [17]. R350HT is often preferred in curves with small radii or in tracks with higher loads, to reduce wear [3].

	R260	R350HT
Fe	bal	bal
Al	0.004	0.004
C	0.82	0.82
Cr	0.15	0.15
Cu	0.15	0.15
Mn	1.25	1.25
Mo	0.02	0.02
N	0.01	0.01
Nb	0.01	0.04
Ni	0.1	0.1
P	0.03	0.025
S	0.03	0.03
Si	0.6	0.6
Ti	0.025	0.025
V	0.03	0.03

Table 2.1: Composition in Wt % for R260 and R350HT.

The Brinell hardness values of R260 and R350HT, as stated in the standard EN 13674-1:2011+A1 [6] are presented in Table 2.2, along with a conversion based on ASTM's standard hardness conversion tables [18], to approximately correlating values in Vickers. Conversions for all HBW values were not provided in the conversion tables, so the closest values included were used instead and are presneted in brackets.

	HBW	HV
R260	260-300 (258-301)	272-318
R350HT	350-390 (353-390)	372-412

Table 2.2: Approximate hardness ranges in HBW converted to HV

To get a better understanding of how the materials react to heat input and cooling, JMatPro was used to create continuous cooling transformation (CCT) diagrams. Figure 2.3 and Figure 2.4 shows the CCT diagrams for R260 and R350HT, respectively. The A_1 transition temperature, where pearlite starts forming from austenite in a eutectoid composition, was calculated to 735.2 °C for R260 and 734.5°C for R350HT. The difference between the two materials is so small that it can be neglected in the forthcoming analyses. In the CCT phase diagram, phase transformations depending on cooling rate can be predicted. To achieve a fully martensitic microstructure, rapid cooling is required. This can be read in the diagrams as a cooling curve which does not cross the pearlite or bainite curves, meaning that a cooling rate above 20 °C/s would be enough to avoid pearlite or bainite formation for both compositions. The diagrams also predict martensite formation to start at around 160°C.

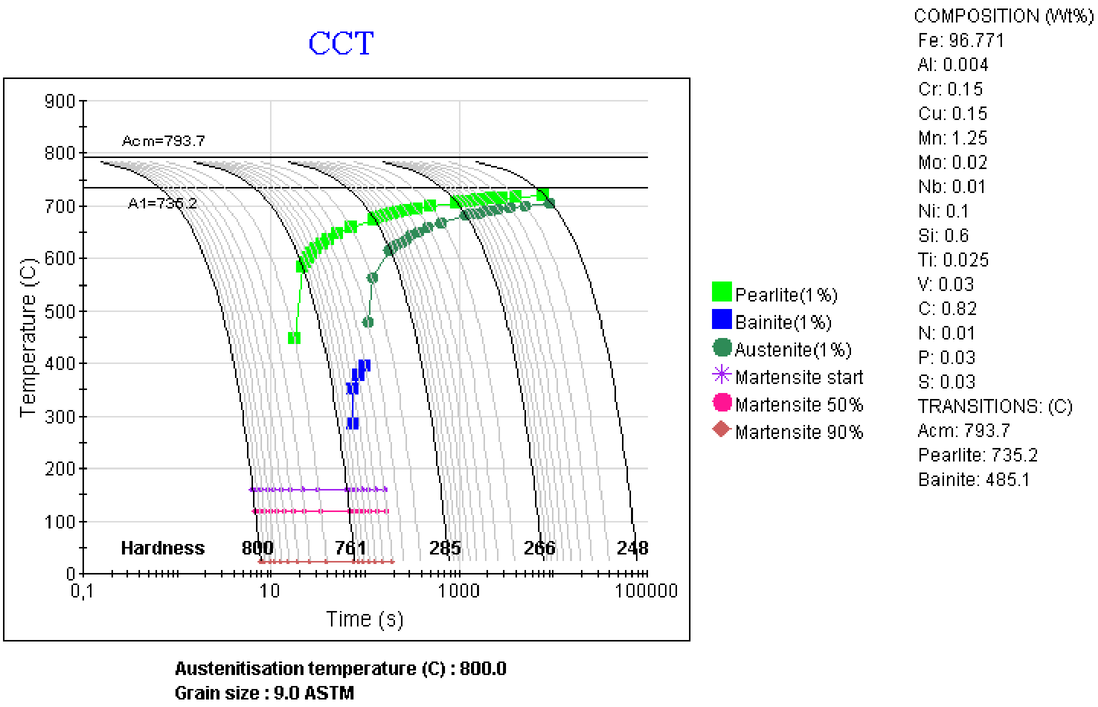

COMPOSITION (Wt%)
Fe: 96.771
Al: 0.004
Cr: 0.15
Cu: 0.15
Mn: 1.25
Mo: 0.02
Nb: 0.01
Ni: 0.1
Si: 0.6
Ti: 0.025
V: 0.03
C: 0.82
N: 0.01
P: 0.03
S: 0.03
TRANSITIONS: (C)
Acm: 793.7
Pearlite: 735.2
Bainite: 485.1

Austenitisation temperature (C) : 800.0
Grain size : 9.0 ASTM

Figure 2.3: CCT diagram for R260.

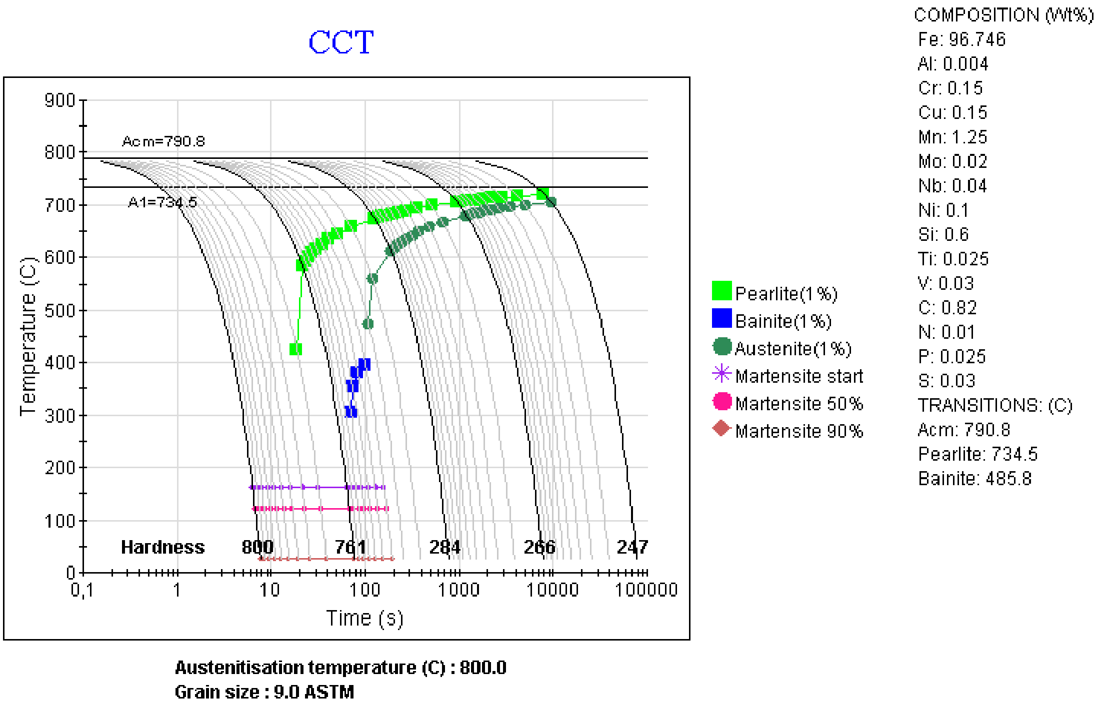

COMPOSITION (Wt%)
Fe: 96.746
Al: 0.004
Cr: 0.15
Cu: 0.15
Mn: 1.25
Mo: 0.02
Nb: 0.04
Ni: 0.1
Si: 0.6
Ti: 0.025
V: 0.03
C: 0.82
N: 0.01
P: 0.025
S: 0.03
TRANSITIONS: (C)
Acm: 790.8
Pearlite: 734.5
Bainite: 485.8

Austenitisation temperature (C) : 800.0
Grain size : 9.0 ASTM

Figure 2.4: CCT diagram for R350HT.

2.4 Microstructure and phase transformations

Steel can exist in several different phases and microstructures. Depending on the phase present, the material exhibits different properties. This means that a material can be tailored to fit a specific application. However, under certain circumstances, such as exposure to very high temperatures, the material's microstructure can be altered. As previously mentioned, pearlite's properties work well for rails, while a more brittle material, such as martensite, is less suitable. To understand the microstructures discussed in this report, short descriptions are provided in the following section.

Pearlite is a two-phase microstructure comprising ferrite (alpha-iron) and cementite, which is a compound of iron and carbon (Fe_3C). Cementite is harder than ferrite and takes the shape of lamellae [19]. It contributes to the material's wear resistance [20]. The interlamellar spacing affects the hardness of pearlite. Pearlite with lower interlamellar spacing, which can be called a finer pearlite microstructure, gives a harder material.

Austenite (gamma-iron) is a phase which forms during heating, at temperatures around 735 °C for the examined materials. It has a face-centered cubic (FCC) lattice structure [19]. When austenite is cooled slowly, it forms pearlite or bainite, depending on the cooling rate. Cooling at a fast rate instead leads to to martensite formation.

Martensite, with a body-centered tetragonal (BCT) structure, is a hard and brittle phase that forms during a diffusionless process when austenite is cooled rapidly [19]. The microstructure often appears lath-like in microscopy. As previously stated, the temperature where martensite would start to form in the examined rail grades is estimated to around 160 °C.

Tempered martensite is achieved when martensite is heated to the point where the microstructure changes. The mechanism involves segregation of carbon, and formation of carbides. This is performed in the temperature range 150 to 650 °C. The process reduces the hardness of the material [19].

Due to heat conduction, a heated thin layer at a ground surface can cool down at a rate equivalent to quenching, causing martensite transformation. According to simulations in JMatPro, a higher cooling rate than 20 °C/s would be required to fully form martensite in R260 and R350HT, avoiding onset of pearlite formation. See Figures 2.3 and 2.4 for the effect of different cooling rates.

2.5 Simulations

2.5.1 Analytical simulations

Analytical simulations are based on theory created by Jaeger [21], complemented by studies by Malkin and Guo [22]. In the simulations, the grinding process is replaced by a moving heat source. The temperature at a given point can be calculated using:

$$\theta = \frac{1}{\pi k} \int_{-l}^{l} q_w(u) e^{-v \frac{(x-u)}{2\alpha}} K_0 \left[\frac{v}{2\alpha} \{(x-u)^2 + z^2\}^{\frac{1}{2}} \right] du \tag{2.1}$$

where k is the thermal conductivity, l is half of the contact length, $q_w(u)$ is the heat flux per unit area going into the material, e is the constant eulers number (≈ 2.718), v is the feedrate of the workpiece, x is the x coordinate of the examined point, u is a x-cordinate of the heat source as seen in Figure 2.5

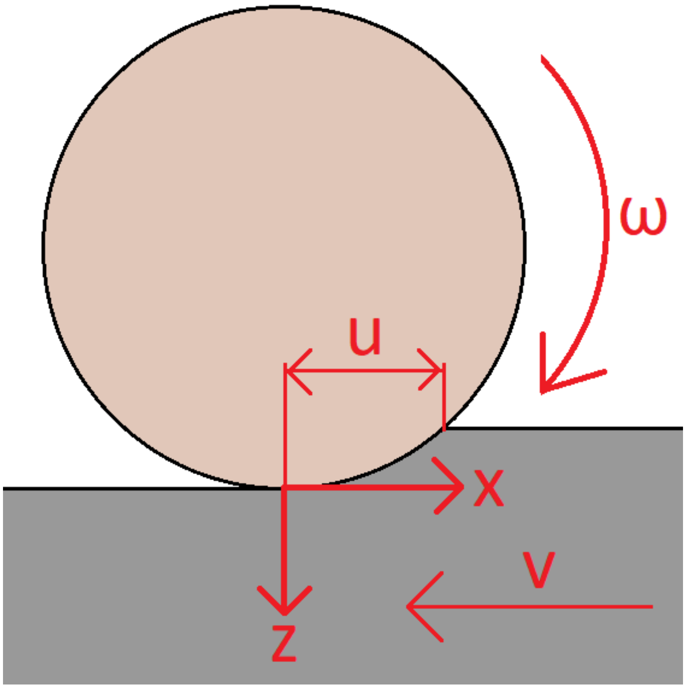

Figure 2.5: Chosen coordinate system

α is the thermal diffusivity and is defined as:

$$\alpha \equiv \frac{k}{Cp\rho} \tag{2.2}$$

with Cp and ρ being the material's specific heat and density, respectively. K_0 is the modified Bessel function of second kind of order zero. z is the downwards distance from the surface of the examined point. The length of contact can be calculated using:

$$l_c = 2 * l = \sqrt{a d_e} \tag{2.3}$$

where a is the depth of cut and d_e is the equivalent diameter. If the total power used during grinding is measured (Q_t) and the power during an "idle" state (Q_i) where the grinding wheel is spinning but the wheel is not touching the workpiece is measured, the grinding power Q_g can be found by subtracting the "idle" power from the total power. The material removal rate is significantly higher at the first point of contact than at the last. This effect can be seen in Figure 2.6 where the red area is bigger at the top than at the bottom.

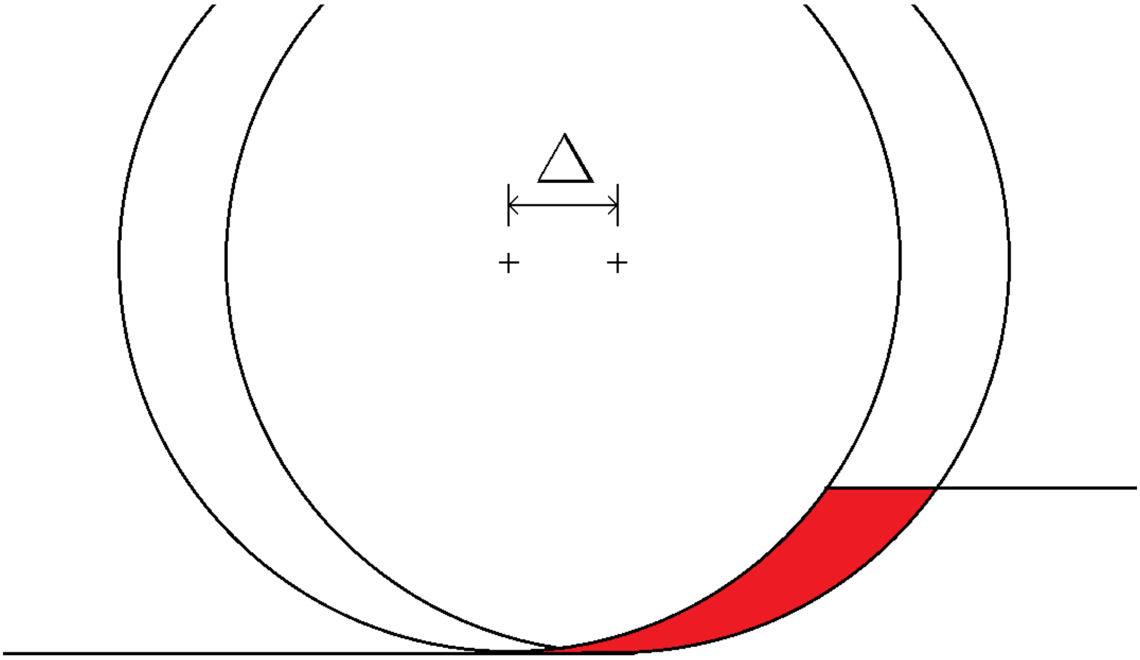

Figure 2.6: material removed after grinding wheel have moved a distance Δ

If the heat distribution is known the total grinding power can be calculated:

$$Q_g = \int_A \frac{q_w}{\epsilon} dA \tag{2.4}$$

Where ϵ is the fraction of grinding power entering the workpiece, and A is the contact area. In grinding it is common to use the average specific energy as a measurement on how efficient the grinding process is. The average specific energy is defined as:

$$E_e = \frac{Q_g}{vwa} \tag{2.5}$$

Where w is the width of the workpiece. With the average specific energy the contact area, specific energy can be calculated using:

$$E_c = E_e * a \tag{2.6}$$

The contact area specific energy is the energy per surface area and should be able to give a good estimation of the martensite depth. The thermal properties of the two materials are assumed to be same since the compositions are almost the same.

The material properties can be seen in Figure 2.7, where the properties of density, thermal conductivity and specific heat are calculated with JMatPro. The thermal diffusivity is then simply calculated using equation 2.2.

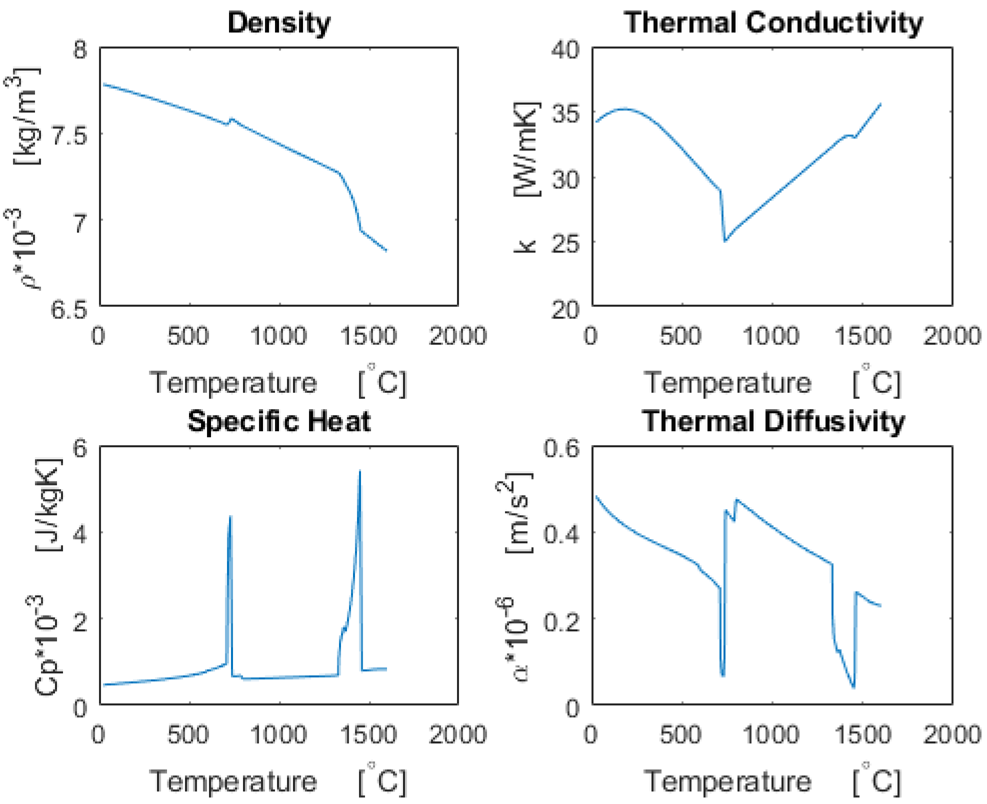

Figure 2.7: Thermal properties with respect to temperature

It can be seen that phase transformations occur at around 700 ° C and around 1400 ° C. The spikes in specific heat at the phase transformations are due to the latent heat.

2.5.2 Finite element simulation

The heat flow into the material can be explained by Fourier's law:

$$q = -k\nabla T \tag{2.7}$$

Where ∇T is the temperature gradient. Finite element method is a method where the field of study is discretised and Fourier's law can be solved for this field. Due to the short amount of time being simulated, the heat convection is assumed to be negligible resulting in the sides being insulated. With the sides being modeled as insulated and a heat source that does not vary in the width direction of the sample there should be no variation in the result in the width direction. This means that the problem can be modelled in two dimension.

3

Methods

This chapter includes detailed descriptions of the test and examination processes performed during the study and how calculations and simulations were made.

3.1 Grinding and sample preparation

Specimens with dimensions 10x40x70 mm^3 were extracted from the rail heads of R260 and R350HT virgin rails. A sketch of a specimen is shown in Figure 3.1. Approximate locations of the specimens in the rail head are shown in Figure 3.2

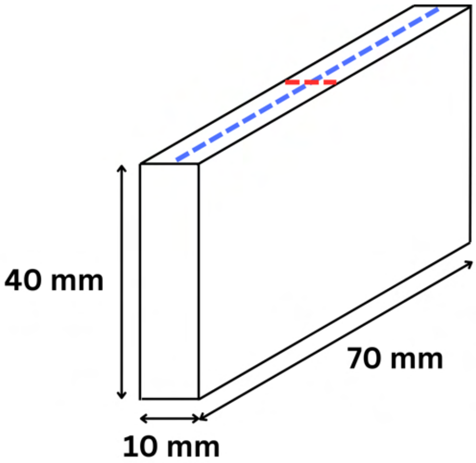

Figure 3.1: Specimen dimensions/specifications.

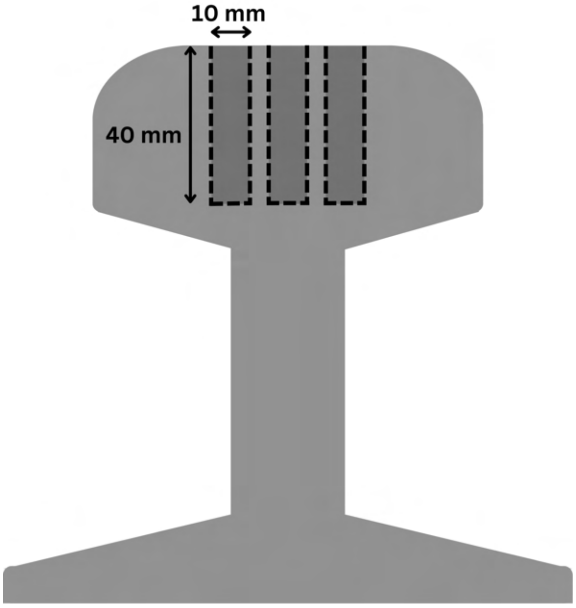

Figure 3.2: Sketch of the cross-section of a rail and approximate location of the extracted specimens.

The specimens were mounted in an industrial grinding machine, Blohm Planomat HP408, and ground in the longitudinal direction with a coarse-grained aluminum oxide, resin-bonded wheel with a 400 mm diameter and 30 mm width. The longitudinal and transverse directions are indicated with a dashed blue and red line, respectively, in Figure 3.1. The wheel is manufactured by Norton Saint-Gobain and has the specification A16Q5B28. The wheel was redressed before each test sequence was started. This was done using a stationary dressing tool with an overlap ratio of 1.5. This wheel is tailored to have the same abrasive specification as a grinding stone used for railway grinding, but the geometry was adapted to fit the grinding machine.

The specimens moved horizontally at varying feedrates, with a stationary wheel grinding the surface of the specimens. Figure 3.3 shows the machine with a specimen. Motions of the wheel and specimen can be seen in Figure 2.5. The tests were conducted using four different feedrates, 2500, 5000, 10000 and 15000 mm/min. Feedrate refers to the (linear) velocity of the workpiece in relation to the position of the grinding wheel. Three different depths of cut, 0.03 mm, 0.06 mm, 0.09 mm, were used, during testing with the highest feedrate. The actual cut depth can deviate from the settings. The combinations of feedrates and depth of cut used during the grinding tests are presented in Table 3.1 The chosen feedrates fall within the range of the grinding machine's capacity. All grinding procedures were conducted with the same wheel (peripheral) speed, 47 m/s.

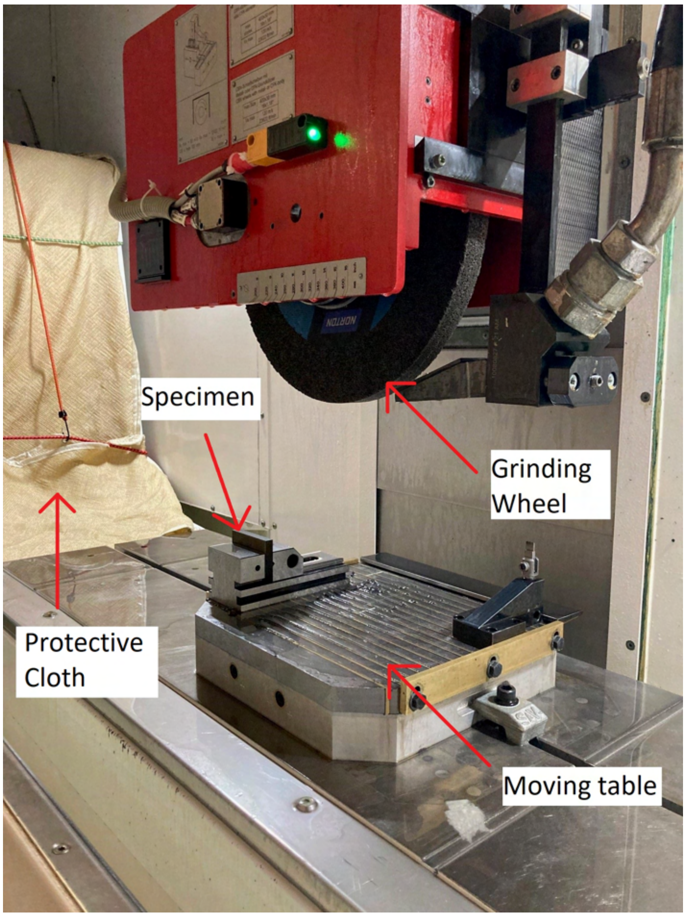

Figure 3.3: Blohm Planomat HP408 set up to grind a specimen.

Feedrate (mm/min)	Depth of cut (mm)
2500	0.03
5000	0.03
10000	0.03
15000	0.03
15000	0.06
15000	0.09

Table 3.1: Grinding parameter setups for the two rail grades, R260 and R350HT

Grinding was performed without coolant, to mimic the conditions of regular railway grinding, where no additional cooling is implemented. This meant that there was nothing to inhibit sparks generated by the grinding, which could potentially damage the machine. To protect the interior and components of the machine itself, protective cloths were put up inside the machine, which also can be seen in Figure 3.3.

To confirm that the values of power were consistent, each specimen was ground five times with the settings and method described above. The only exception is specimen R350HT with feedrate 2500 mm/min, which was ground six times. The difference should not influence the results. Fluctuations are known to occur in tests like these, due to the wheel's microtopography changing. Between these testing sessions, the specimens were ground ten times with coolant applied, at a feedrate of 800 mm/min and depth of cut of 0.02 mm for each pass, to restore a pearlitic surface microstructure. Evaluation of surface and microstructure was only performed after the final grinding session, for each specimen.

In addition to the planar grinding procedure described so far, facet grinding was also performed. To replicate profile grinding, two specimens of each rail grade, meaning four in total, were ground to produce a surface with two facets along the longitudinal direction, as presented in Figure 3.4.

Figure 3.4: The angle between facets.

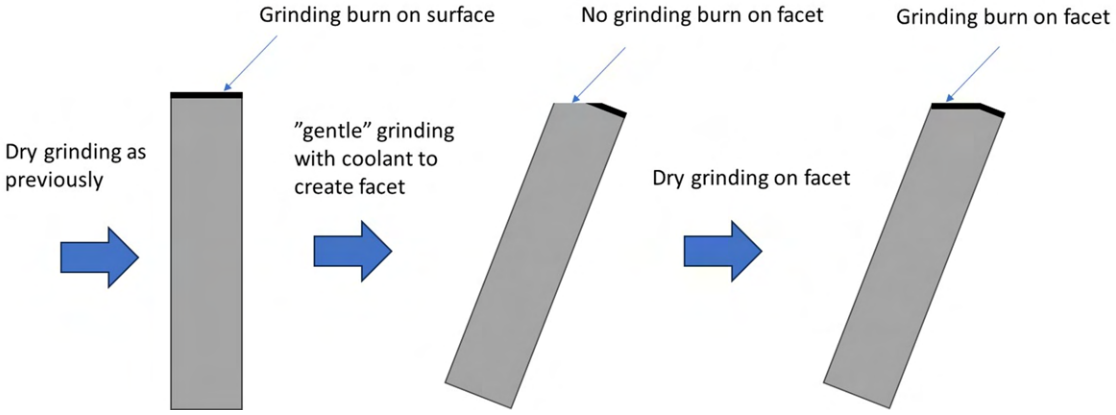

Figure 3.5: Procedure to create the faceted samples. Image created by Philipp Hoier

This was accomplished by first grinding the entire surface of the extracted specimens. This was followed by tilting the specimen with the vice and grinding slowly, with cooling, in order not to alter the microstructure before-hand. This produced a second surface with an angle of approximately 20° in relation to the original plane, and a width of ca 5 mm. This facet surface was subsequently ground using the same parameters as for the first as seen in Figure 3.5. The parameter combinations used were a feedrate of 2500 mm/min along with a depth of cut of 0.03 mm and a feedrate of 15000 mm/min along with a depth of cut of 0.09 mm, for both rail grades.

Another facet grinding test, with a feedrate of 20000 mm/min was performed, but the appearance of the surface martensite layer was uneven and not satisfactory in comparison with the other specimens. Therefore, no results of this test are presented in this report.

3.2 Visual examination

The ground specimens were examined using a Zeiss Stereo Discovery V20 stereo optical microscope and a Zeiss Axioscope 7 optical microscope. The surfaces and areas close to the surface on each side were scanned and documented. Any oddities or damage, such as possible cracks, were recorded.

Repetitive patterns were observed on the ground surfaces. The distance between the occurrences was measured manually, using a ruler. The distance was also measured in ZenCore, for one sample, and in AxioVision for another sample, to verify that the manual measurements were accurate. As the distance between the repeating marks was suspected to be dependent on the revolutions of the grinding wheel, the workpiece's traveled distance between revolutions was also estimated, using the following calculations:
The circumference of the wheel is:

$$400 * \pi = 1256.6 \ [mm] \tag{3.1}$$

To calculate the time for one revolution, the circumference (1.2566 m) is divided by the peripheral wheel speed (47 m/s). This results in a revolution time of 0.0267 seconds. That multiplied with the feedrates (2500, 5000, 10000, 15000 mm/min) gives the resulting travelled distance of the workpiece during one revolution of the grinding wheel.

3.3 Surface roughness measurements

Surface roughness measurements were made on the planar ground specimens with Mitotuyo Surftest SJ-210, calculating the R_a and R_z values. Five measurements were made for each sample, in the transverse direction. The measurements were taken at approximately 5, 20, 35, 50 and 65 mm of the total specimen length. These locations are referred to 1, 2, 3, 4 and 5, respectively, and can be seen in Figure 3.6. The averages of the R_a and R_z values of these individual measurements were then calculated for each specimen. Surface roughness was not measured on the facet ground specimens.

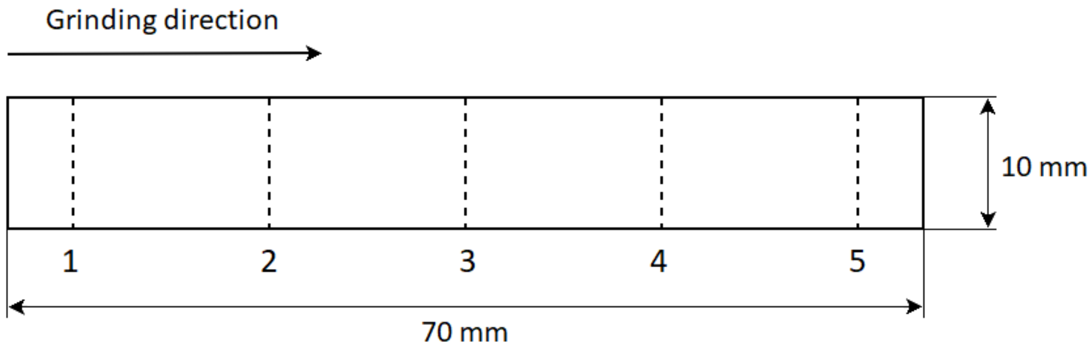

Figure 3.6: Sketch of top view of the sample. The dashed lines represent the locations of surface roughness measurements.

3.4 Sample preparation

After surface roughness was measured, the planar ground specimens were cut into smaller samples with two different machines: Struers Discotom-2 and Buehler IsoMet High Speed Pro Precision Cutter. Struers Discotom-2 was used for the transverse cuts, while Buehler IsoMet High Speed Pro Precision Cutter was used for cuts in longitudinal direction, mainly to reduce the amount of material consumed. The location of the cuts were the same for all specimens and are presented in Figure 3.7. The three transverse cutting locations were chosen to provide a sample from the middle (marked as 4 in Figure 3.7) and samples close to the ends of the specimen (marked as 2 and 5 in Figure 3.7). However, the distance from the ends needed to be enough to avoid effects caused by the initiation and completion stages of the grinding procedure.

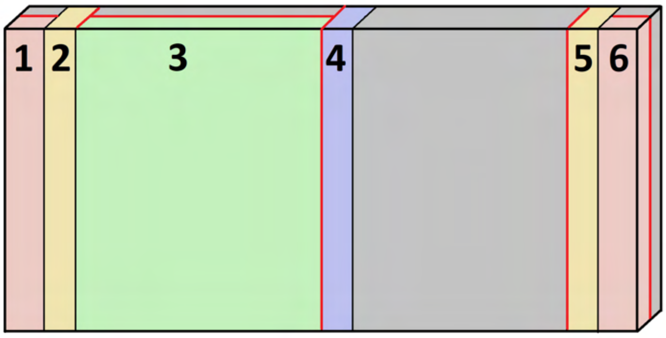

Figure 3.7: Sketch of the sample with the location of cuts indicated by lines. Different types of samples are indictated by different colors and different samples are numbered. The surface that was investigated is also marked with a red line.

One sample, around 20 mm long, was made in the longitudinal direction (marked as 3 in Figure 3.7), to examine indications of an uneven heat affected layer, to measure its minimum and maximum depth and to look for other inconsistencies, which could stem from machine vibrations or out-of-roundness of the grinding wheel. Some surface cracks, which were observed on one specimen (R260, feedrate: 5000 mm/min) during visual examination of the ground surfaces, were present within this zone. Therefore, the layer and the cracks could be examined simultaneously.

The zone closest to the edges, where grinding started and ended was also cut longitudinally (marked as 1 and 6 in Figure 3.7), for the samples with feedrate 2500 mm/min and depth of cut 0.03 mm and feedrate 15000 mm/min and depth of cut 0.09 mm to ensure that the heat affected layer reached a consistent depth within that zone. This is done since the effects of the start/end of grinding is not within the scope of this project and must not affect the results of the study.

Only one sample was cut from each of the facet ground specimens. The location of these samples correspond to the region marked as 4 in Figure 3.7.

In preparation for microscopy, the samples were mounted in Polyfast resin, using a Struers CitoPress-20. The surfaces of the mounted samples were first ground with Struers Abrapol-2, using silicon carbide discs starting with a rough 220 grit and step by step proceeding to finer grits, up to 2000. Water was used as coolant throughout the process. To finish the surface preparation, the samples were mechanically polished with a Struers TegraForce-5 in two steps: first with a 3 µm diamond suspension, and then with a 1 µm suspension. The polished surfaces were then etched by dipping in 2% Nital until the microstructure was revealed.

3.5 Optical microscopy

After the preparation process, the samples were examined in the Zeiss Axioscope 7. The main focus was to take measurements and capture the appearance of the transverse sample corresponding to region 4 and the longitudinal sample corresponding to region 3 in Figure 3.7. The samples from the other locations were also examined, but will not be described in this report. They only served the purpose of confirming that the chosen samples are good representations to show the effects of the grinding process as a whole.

To determine the volume affected by the heat input from grinding, to the point of phase transformation, depth measurements were made in the Zen Core 2.7 software. The presented values for depth were measured in the middle and at the edges of the cross-sectional transverse samples. For the longitudinal samples, the minimum and maximum depth of the layer was instead measured. For the facet ground samples, depth measurements were taken at the left and right edge of the samples, in the middle of both facets and at the "intersection" of the two facets, where one measurement was taken of each layer. This is, in total, six measurements for each facet ground specimen. Figure 3.8 shows a sketch with the measurement locations of the transverse samples, indicated with dashed lines, and Figure 3.9 shows the measurement locations for the facet ground specimens.

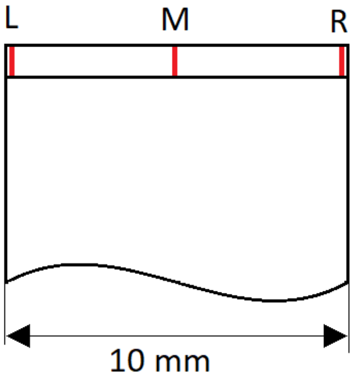

Figure 3.8: Locations of the measurements in the cross-sectional planar samples.

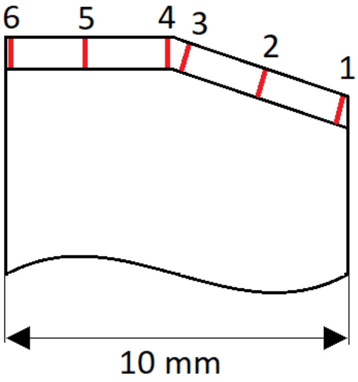

Figure 3.9: Locations of the measurements in the cross-sectional, facet ground samples.

3.6 Micro hardness testing

Vickers hardness tests were conducted using Struers Emcotest Durascan-70 G5 hardness tester, with a 0.05 kg load. For each sample, a series of indentations were made in the middle and close to the edges of the heat-affected layer, extending further into the pearlitic region. The distance between indentations was set to be at least three times the indentation width. During measuring, any indentations that were too blurry in the images were excluded.

3.7 Scanning electron microscopy

Scanning electron microscopy (SEM) was performed, using a LEO Gemini 450 field emission gun scanning electron microscope, running in secondary electron mode. The voltage used was 20 kV and the working distance was 8.3-8.9 mm. A number of images were taken of cracks, transition zones and the general appearance of the microstructure, especially the martensite with varying degrees of tempering.

3.8 Analytical simulations

In order to calculate a temperature field, the grinding equation 2.1 was rewritten as:

$$\theta_{m,n} = \sum_{j=1}^{100} \frac{1}{\pi k_{j-1}} \sum_{i=1}^{100} \frac{q_{w,i}}{100} e^{-v\frac{(x_m - u_i)}{2\alpha_{j-1}}} K_0 \left[\frac{v}{2\alpha_{j-1}} \{(x_m - u_i)^2 + z_n^2\}^{\frac{1}{2}} \right] \Delta u_i \qquad (3.2)$$

Where j is a counter used to apply the heat in steps which enables the material parameters α and k to be temperature dependent. For simplicity they are chosen to be calculated by the previous heat step. These calculations are done using Matlab, where the highest number precision is double (32 bites). This number precision would lead to problems when $\alpha < 5 * 10^{-6}$ so the material data is altered where the spikes due to latent heat are spread over a bigger temperature span as shown in Figure 3.10

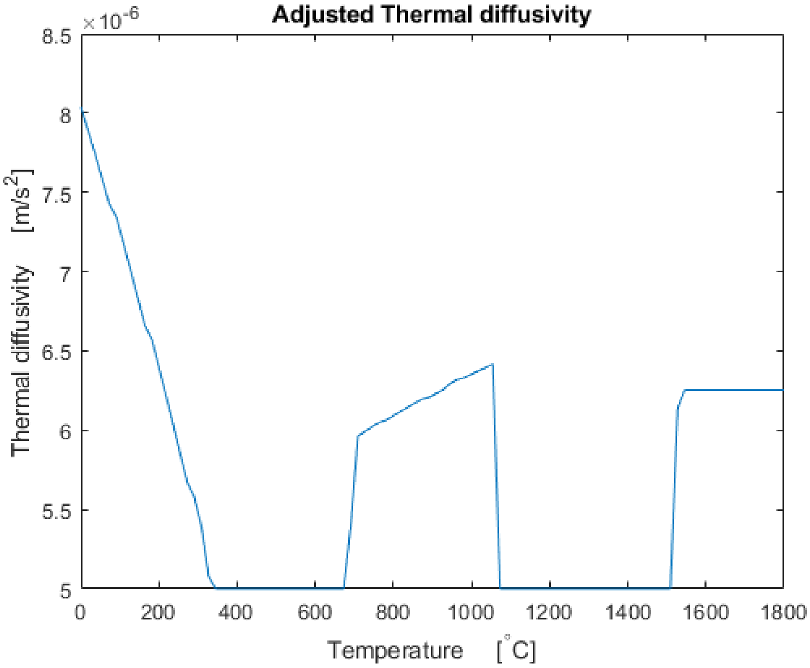

Figure 3.10: Thermal diffusivity (α) vs temperature

The heat source stepsize (Δu) is chosen be constant and u varies from 0 to l_c. q_w is constructed by combine four different heat flux distributions:

$$q_w = q_{w1} + q_{w2} + q_{w3} + q_{w4} \qquad (3.3)$$

The first one is assumed to be constant over the entire domain and is simply:

$$q_{w1}(x) = \begin{cases} c_1 \frac{\epsilon Q}{l_c * w} & \text{for } 0 < x < l_c \\ 0 & \text{otherwise} \end{cases} \qquad (3.4)$$

where w is the sample width, c_1 is the fraction of the energy that is assumed to be constant over the contact length and x is a coordinate in the grinding direction where

$x = 0$ is directly under the center of the wheel. The other heat flux distributions are set to be triangular and are set up in following way:

$$q_{w2}(x) = \begin{cases} c_2 \frac{\epsilon Q}{w} \frac{2x}{l_c} & \text{for } 0 < x < l_c \\ 0 & \text{otherwise} \end{cases} \tag{3.5}$$

$$q_{w3}(x) = \begin{cases} c_3 \frac{\epsilon Q}{w} \left(\frac{8x}{l_c} - 4 \right) & \text{for } \frac{l_c}{2} < x < l_c \\ 0 & \text{otherwise} \end{cases} \tag{3.6}$$

$$q_{w4}(x) = \begin{cases} c_4 \frac{\epsilon Q}{w} \left(\frac{32x}{l_c} - 24 \right) & \text{for } \frac{3l_c}{4} < x < l_c \\ 0 & \text{otherwise} \end{cases} \tag{3.7}$$

For no energy to be added or subtracted in rewriting the heat flux in this way it is required that:

$$c_1 + c_2 + c_3 + c_4 = 1 \tag{3.8}$$

The constants are iterated in such a way that the temperature along the contact length should be close to constant. The chosen set of constants where:

c_1	0.45
c_2	0.3
c_3	0.1
c_4	0.15

Table 3.2: Constants chosen to produce the desired temperature field.

The final heat flux distribution can be seen in figure 3.11

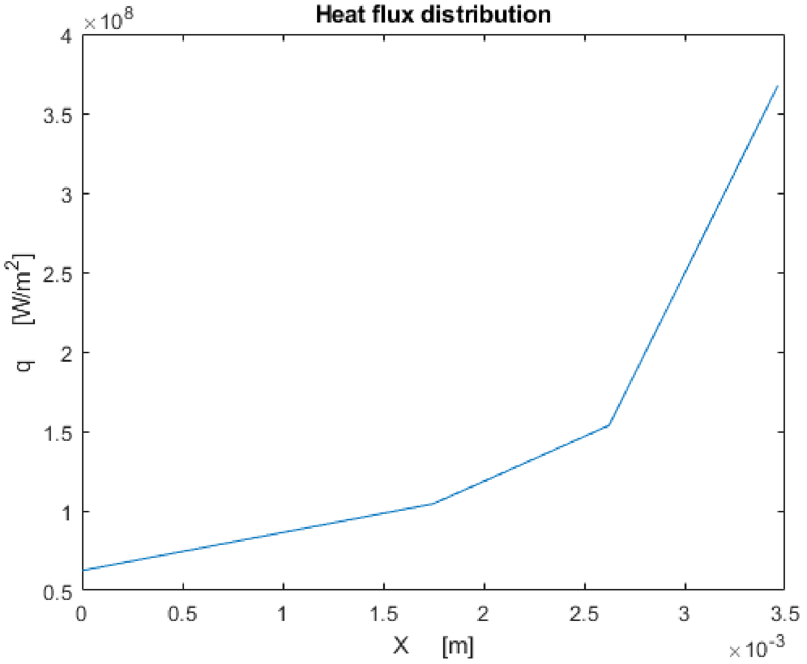

Figure 3.11: The heat flux distribution below the grinding wheel

By equation 3.2 the temperature is calculated in a 100 by 100 grid. If the temperature between two adjacent points is assumed to be linear the discretised field becomes continuous. The martensite depth is now estimated as the highest distance between the grinding surface and the z-coordinate where $\theta = 715°C$. with a assumed ambient temperature of 20 °C this results in a austenitisation temperature of $735°C$.

There is a large difference between the martensite depth from the analytical calculations and the measured martensite depth with optical microscope. Because of this a new grinding power is calculated by iterating:

$$Q_{g+1} = Q_g * \left(\frac{d_m}{d_a}\right)^{0.3} \tag{3.9}$$

Where d_m is the measured depth in optical microscope and d_a is the result from the analytical simulations. The grinding power is accepted when $\frac{d_m}{d_a}$ is in the range 1 ± 0.05.

3.9 Finite element simulations

In the finite element program COMSOL the regular specimens are simulated in 2D. The grinding process is replaced with a heat source on the surface. This is done by applying a heat flux on the entire top surface and multiplying with a function that returns a non zero value if the node position is within the contact length distance ahead of the heat source position. All other surfaces except the grinding surface are set to be insulated. The heat flux distribution is set up in the same way as the analytical with one constant and three triangular parts. The material parameters k, Cp and ρ are set to be temperature dependent making the finite element simulation non linear.

The simulation is time dependent and is set to run for a time period slightly longer than the time it takes for the heat source to travel the specimen length of 70 mm. The finite element mesh size is quite rough over the majority of the domain (max 0.7 mm), with a zone 14 mm wide and 5 mm deep along the top surface with smaller element size (max 0.1 mm). Inside this zone there is a 8 mm wide zone and 2 mm thick where the element size is further decreased (max 0.01 mm). This approach is chosen to give a place where the result should be reliable while keeping computational times low. To check how quickly the cooling of the martensite layer happens the simulation time is set to 10 seconds.

4

Results

In this chapter the results and findings of the experiments and simulations are presented. The main focus is the influence of different parameters on the thermally induced formation of martensite. This includes the martensite layer depth and how it is related to the heat input.

4.1 Grinding measurements

Blohm Planomat HP408 gives the power used during grinding. In Table 4.1 the average values of five power measurements (Q_g) of each specimen are presented for various feedrates (v) and depths of cut (a). The table also shows the calculated contact length (l_c), the average specific energy (E_e) and the contact area specific energy (E_c).

Material	v [mm/min]	a [mm]	Q_g [W]	l_c [mm]	E_e [J/mm^3]	E_c [J/mm^2]
R260	2500	0.03	5337	3.5	426	12.81
R260	5000	0.03	6140	3.5	245.6	7.37
R260	10000	0.03	6124	3.5	122.5	3.67
R260	15000	0.03	6480	3.5	86.4	2.59
R260	15000	0.06	8453	4.9	56.4	3.38
R260	15000	0.09	11394	6	50.6	4.56
R350HT	2500	0.03	4675	3.5	369.9	11.22
R350HT	5000	0.03	4882	3.5	195.3	5.86
R350HT	10000	0.03	6135	3.5	122.7	3.68
R350HT	15000	0.03	6815	3.5	90.9	2.73
R350HT	15000	0.06	9215	4.9	61.4	3.69
R350HT	15000	0.09	11472	6	51	4.59

Table 4.1: Grinding data related to power

It is clear from this table that the grinding power increases with both feedrate and depth of cut. Also, the specific energy decreases with an increasing feedrate and depth of cut, making the grinding more energy efficient. The contact area specific energy decreases with feedrate and increases with depth of cut.

4.2 Surface examination

Microscopy provided clear images of the ground surface. Upon inspection, several phenomena were noted and examined. These results, as well as surface roughness measurements, are presented below.

4.2.1 Surface pattern

Periodic patterns, consisting of marks and lines in the transverse direction, had emerged on the surface of all specimens as a result of grinding. The shape of the patterns appear different from specimen to specimen but certain trends are obvious. The distance between the repeating sets of marks varies depending on feedrate. The frequency of the recurring pattern seemed to correspond to the distance the specimens travel between each revolution of the grinding wheel and was confirmed by manual measurements on all specimens and digital measurements made on two specimens, which can be viewed in Figure 4.1 and Figure 4.2.

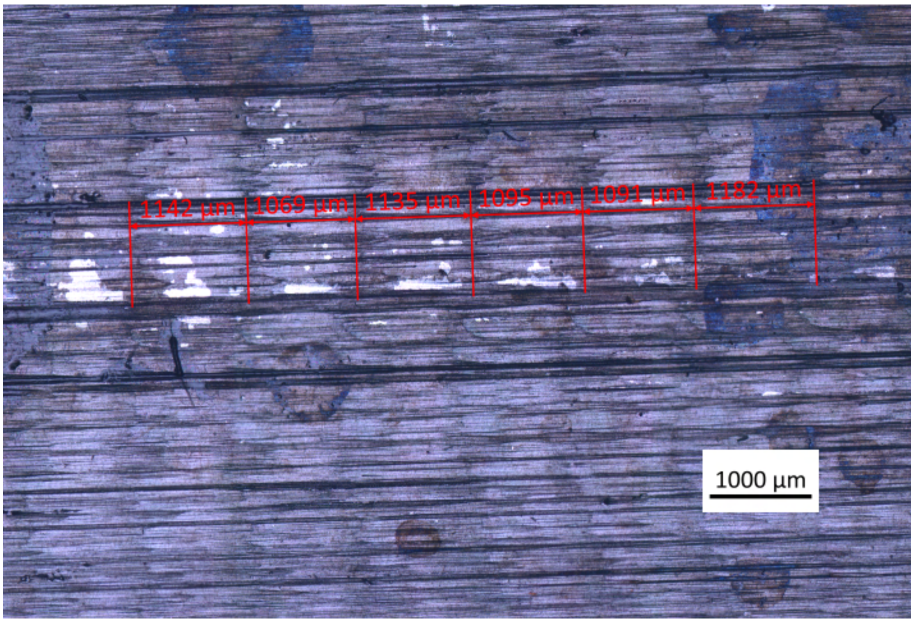

Figure 4.1: Measurements between patterns on the surface of a sample of material R260 ground with feedrate 2500 mm/min and with depth of cut 0.03 mm.

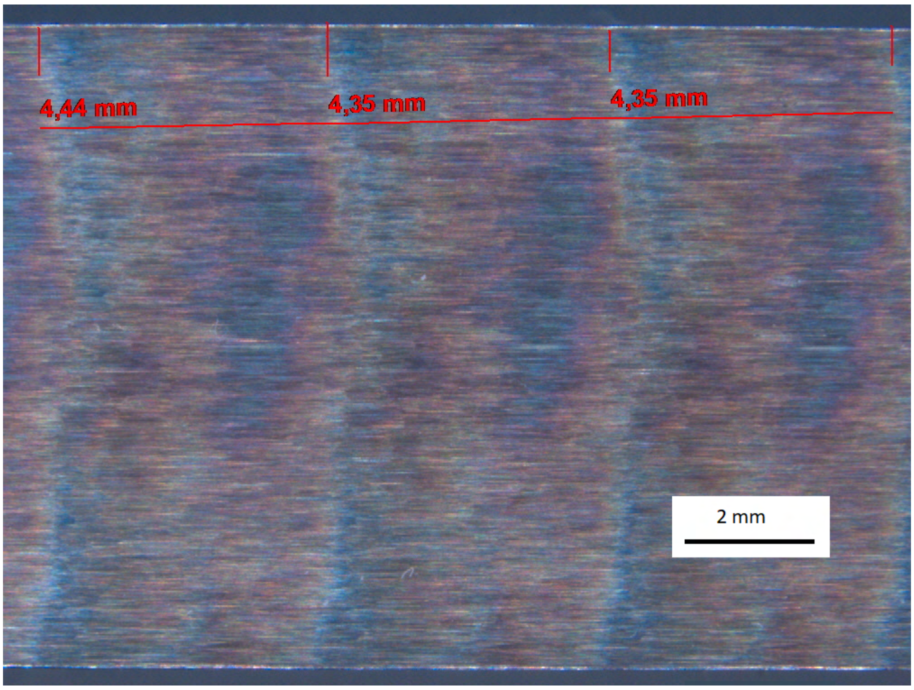

Figure 4.2: Measurements between patterns on the surface of a sample of material R260 ground with feedrate 10000 mm/min and with a depth of cut 0.03 mm.

In Table 4.2, the calculated travelled distances are presented and can be compared with the manually measured distances between the surface marks. The results of the manual measurements are approximate since it is difficult to measure precisely.

Feedrate [mm/min]	Calculated distance [mm]	Measured distance [mm]
2500	1.11	1
5000	2.23	2.5
10000	4.46	4.5
15000	6.68	7

Table 4.2: Travelled distance of specimens during one revolution and approximate measured distances between periodic surface marks, depending on feedrate.

4.2.2 Surface discoloration

The ground surfaces also exhibit discloration. This is likely related to an oxidation phenomenon which can turn the surface into shades of blue [23] [24], though it is difficult to draw any significant conclusions based on this. The feedrate seemingly has an effect on the phenomenon. Images of all surfaces are shown in Figure 4.3.

For R260, the surfaces ground with feedrates of 2500 mm/min and 5000 mm/min look relatively unchanged colorwise. At the feedrate of 10000 mm/min, the surface had received a golden tone, with some brown marks. At 15000 mm/min blue areas had also appeared, along with the golden/brown shades. R350HT show slightly different results. The surfaces ground at 2500 and 5000 mm/min appear dark, but without any indication of a golden shade. Furthermore, the blue discoloration appeared already at 10000 mm/min along with the golden shade. The surfaces of the specimens ground at a feedrate of 15000 mm/min (depth of cut: 0.03 and 0.06) appear almost completely blue, while the specimen ground at 15000 mm/min (depth of cut: 0.09) had turned golden and blue.

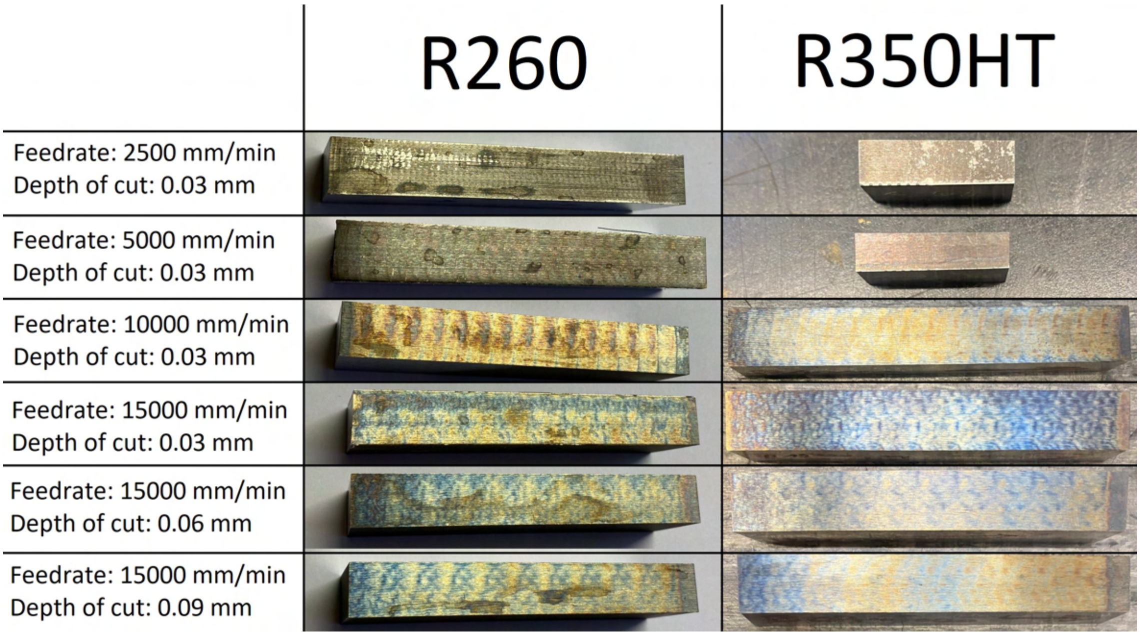

Figure 4.3: Surfaces of specimens after grinding.

4.2.3 Surface roughness

The surface roughness measurements for each specimen are presented in Table 4.3, and Table 4.4 for R260, and Table 4.5 and Table 4.6 for R350HT. The numbers in the top row of the tables represent the different measurement locations, which are shown in Figure 3.6. The surface roughness values R_a and R_z were both recorded.

	1	2	3	4	5	Average
A2500	0.570	0.635	1.185	1.301	1.014	0.9
A5000	0.769	0.799	0.786	1.237	0.931	0.9
A10000	0.308	0.374	0.488	0.451	0.357	0.4
A15000	0.48	0.456	0.466	0.394	0.371	0.4
A06_15000	0.537	0.581	0.626	0.641	0.638	0.6
A09_15000	0.5	0.62	0.79	0.77	0.862	0.7

Table 4.3: Recorded R_a values for R260, in µm.

	1	2	3	4	5	Average
A2500	4.642	4.573	7.852	9.807	7.776	6.9
A5000	5.786	5.211	6.490	8.090	6.353	6.4
A10000	2.730	4.208	3.525	3.856	2.974	3.5
A15000	3.127	3.404	3.577	2.592	2.339	2.9
A06_15000	3.738	4.054	3.948	5.159	3.826	4.1
A09_15000	3.436	4.327	8.077	5.501	5.989	5.5

Table 4.4: Recorded R_z values for R260, in μm.

	1	2	3	4	5	Average
B2500	0.701	0.403	0.902	1.190	0.897	0.8
B5000	0.385	0.413	0.491	0.444	0.748	0.5
B10000	0.679	0.813	0.667	0.765	0.756	0.7
B15000	0.632	0.603	0.583	0.603	0.655	0.6
B06_15000	0.540	0.680	0.592	0.551	0.836	0.6
B09_15000	0.462	0.493	0.441	0.740	1.621	0.8

Table 4.5: Recorded R_a values for R350HT, in μm.

	1	2	3	4	5	Average
B2500	9.874	3.635	6.010	8.720	6.478	6.9
B5000	3.327	3.217	3.011	3.313	10.545	4.7
B10000	4.691	7.957	4.682	4.708	5.111	5.4
B15000	4.352	4.000	4.034	4.066	5.163	4.3
B06_15000	4.770	4.926	4.923	4.283	8.959	5.6
B09_15000	4.489	4.482	3.780	6.535	12.401	6.3

Table 4.6: Recorded R_z values for R350HT, in μm.

Based on these results, there seems to be a general decrease in surface roughness with increasing feed rate and an increase in surface roughness with increasing depth of cut. However, this is not true for the R_a values of R260, with the increase from 5000 to 10000 mm/min and both the R_a and R_z values of R350HT for the increase from 5000 to 10000 mm/min.

4.2.4 Comparison to in-field ground rail

During the project, two 60 EI rail pieces of rail grade R260, which had been ground in-field were provided. These will serve as a simple comparison to the literature and laboratory studies. Images of the rail heads are provided in Figure 4.4. Rail piece 1 is taken from straight track and rail piece 2 from a transition curve. The different facets produced by grinding are easily distinguishable on both pieces. Measurements confirm that the width of the facets align with the recommendations previously described [15]. No surface roughness measurements were made, but by visual examination it is evident that the surfaces of both pieces have a rougher finish than the surfaces of the laboratory ground specimens. Surface burn is visible on some facets on rail piece 2, indicated with arrows in Figure 4.4f but most of the areas have not received any thermal damage.

(a) Cross-section of rail piece 1.

(b) Cross-section of rail piece 2.

(c) Top view of rail piece 1.

(d) Top view of rail piece 2.

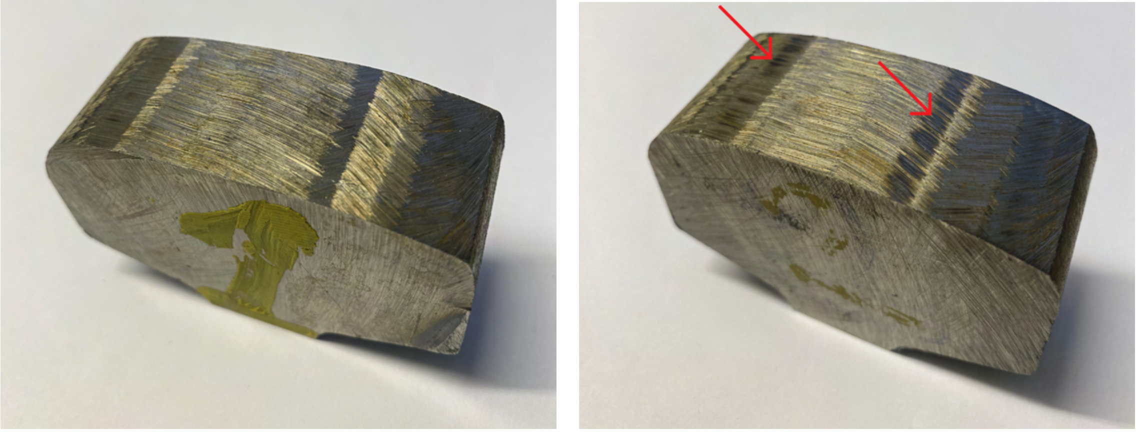

(e) Additional image of ground facets on rail piece 1.

(f) Additional image of ground facets on rail piece 2.

Figure 4.4: Images of rail heads ground in-field.

4.3 Microstructure

From this section onwards, transverse cross-sectional samples are referred to by their grade, feedrate and if necessary, depth of cut. Examples of this are: R260, 2500 and R350HT, 15000, 0.09. The longitudinal cross-sectional samples and the faceted transverse cross-sectional follow the same naming rule, but are indicated at the end by -L and -F, respectively. Examples are: R350HT, 15000, 0.09-L and R260, 15000-F.

Optical microscopy of the cross-sectional transverse and longitudinal samples revealed that WEL had formed along the surfaces, as expected. The general appearance of the layers in the transverse samples is relatively uniform in depth/thickness and bright, clearly distinguishable from the original pearlite. The layers have formed at the ground surface and extend deeper into the specimens to varying degrees, depending on feedrate. In the longitudinal samples, the layers look similar. Since the layers visually appeared similar to WEL described in literature, it is reasonable to assume that they are martensitic. SEM produced improved images of the microstructure which provided further proof that the so-called WEL mostly consisted of martensite.

In some samples, parts of the martensite layer appear dark. This is an indication of tempered martensite. An example of this is the R260, 2500 shown in Figure 4.5. SEM images of the two sides are also shown in Figure 4.6 and 4.7 where the right side is more affected by etching.

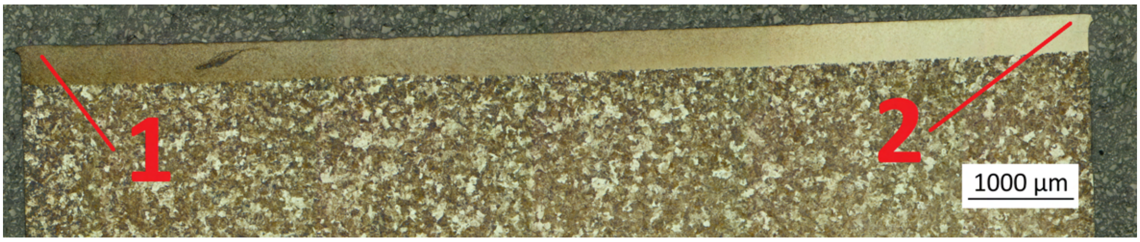

Figure 4.5: Cross-section of sample R260, 2500.

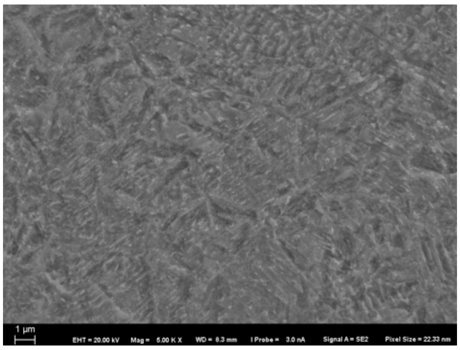

Figure 4.6: SEM image from area 1 in Figure 4.5

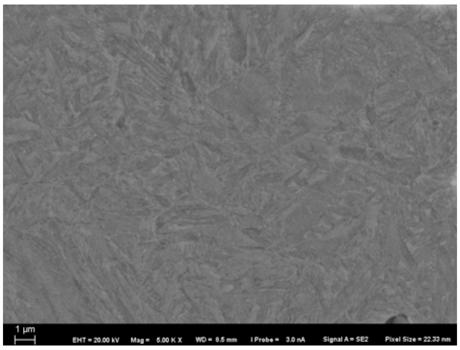

Figure 4.7: SEM image from area 2 in Figure 4.5

Figure 4.8 shows R260, 15000, 0.03. Compared to the rest, the appearance of this sample is different. The bright martensite layer is uneven, meaning that the depth varies a lot. It looks uniform close to the right edge, but becomes thinner in the middle section and towards the left side. At the left edge, it increases in depth again. Additionally, there is an arc-shaped brown area on the right side of the sample, between the bright martensite layer and the pearlite.

Figure 4.8: Cross-section of sample R260, 15000, 0.03.

Figure 4.9 shows R350HT, 10000, which represents the general appearance of the transverse samples well. It has a bright layer across the whole subsurface. Note how the layer decreases in thickness close to the edges.

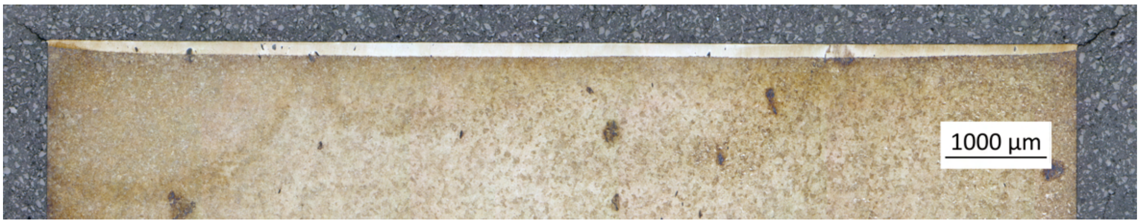

Figure 4.9: Cross-section of sample R350HT, 10000.

Figure 4.10 shows a longitudinal sample, R350HT, 15000, 0.09-L. Here, a slight waviness of the layer can be observed, typical for the longitudinal samples.

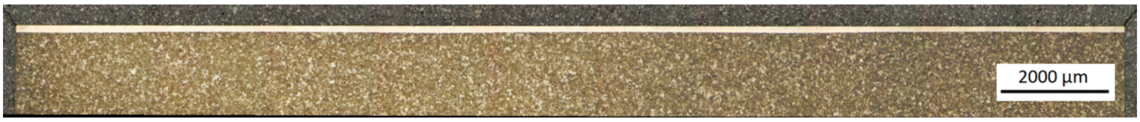

Figure 4.10: Cross-section of sample R350HT, 15000, 0.09-L

Figure 4.11 shows R260, 2500-F. The martensite layer has been heavily affected by etching. The surface to the left side of the picture was ground first. It can be seen that the martensite layer has its maximum depth close to the center and decreases in depth towards the edge of the sample, following the same trend as the non-faceted samples. The layer to right side is arc-shaped, with a significant decrease in thickness towards the edges of the layer. The decrease in depth is most prominent at the right edge of the layer. This trend is also observed in the three other facet ground samples.

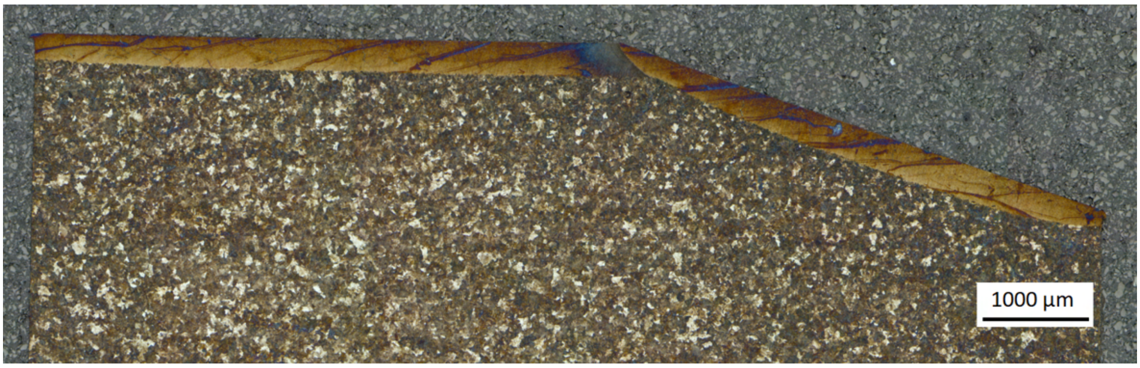

Figure 4.11: Cross-section of sample R260, 2500-F.

Figure 4.12 shows a close up of the overlap zone of the martensite layers formed by the two facet grinding procedures, previously shown in 4.11. During grinding of the second surface, a new martensite layer formed (zone 3 in Figure 4.12). Part of the martensite layer formed during grinding of the first surface austenitised, reaching the A_1 temperature, and transformed into martensite again at cooling. Beyond that layer, the temperature was high but remained below A_1 and the existing martensite was instead tempered. This is marked as zone 2 in Figure 4.12. The rest of the original layer (zone 1) was seemingly unaffected by the heat input during grinding of the second facet.

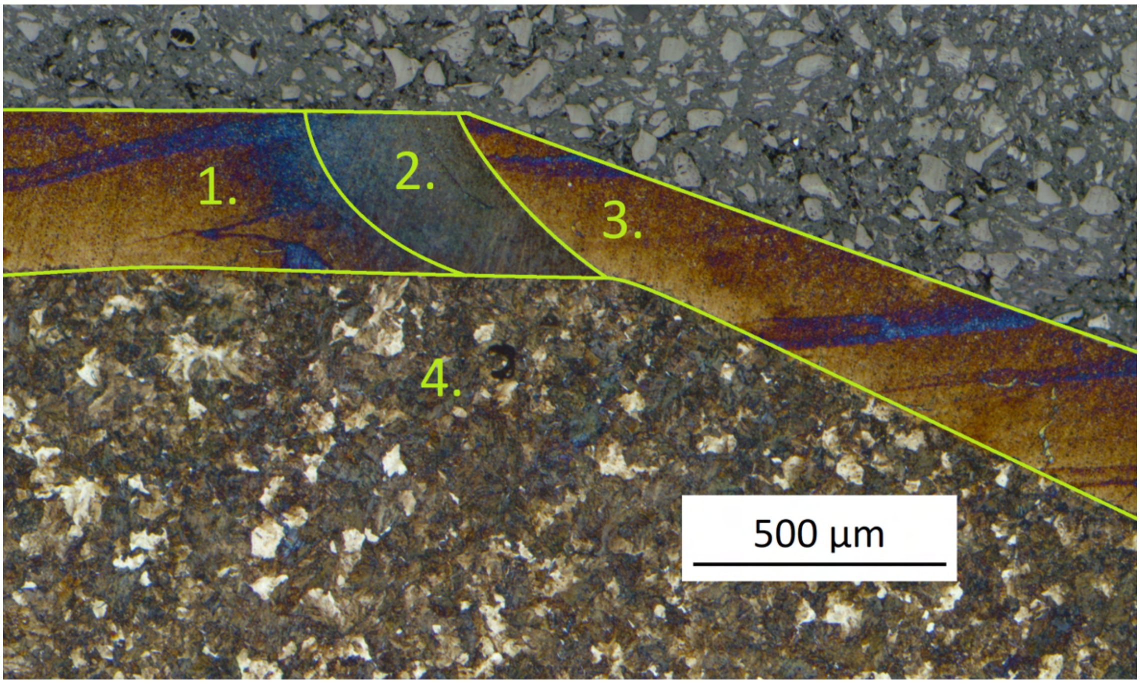

Figure 4.12: Close-up of cross-section of sample R260, 2500-F with 4 visually different zones.

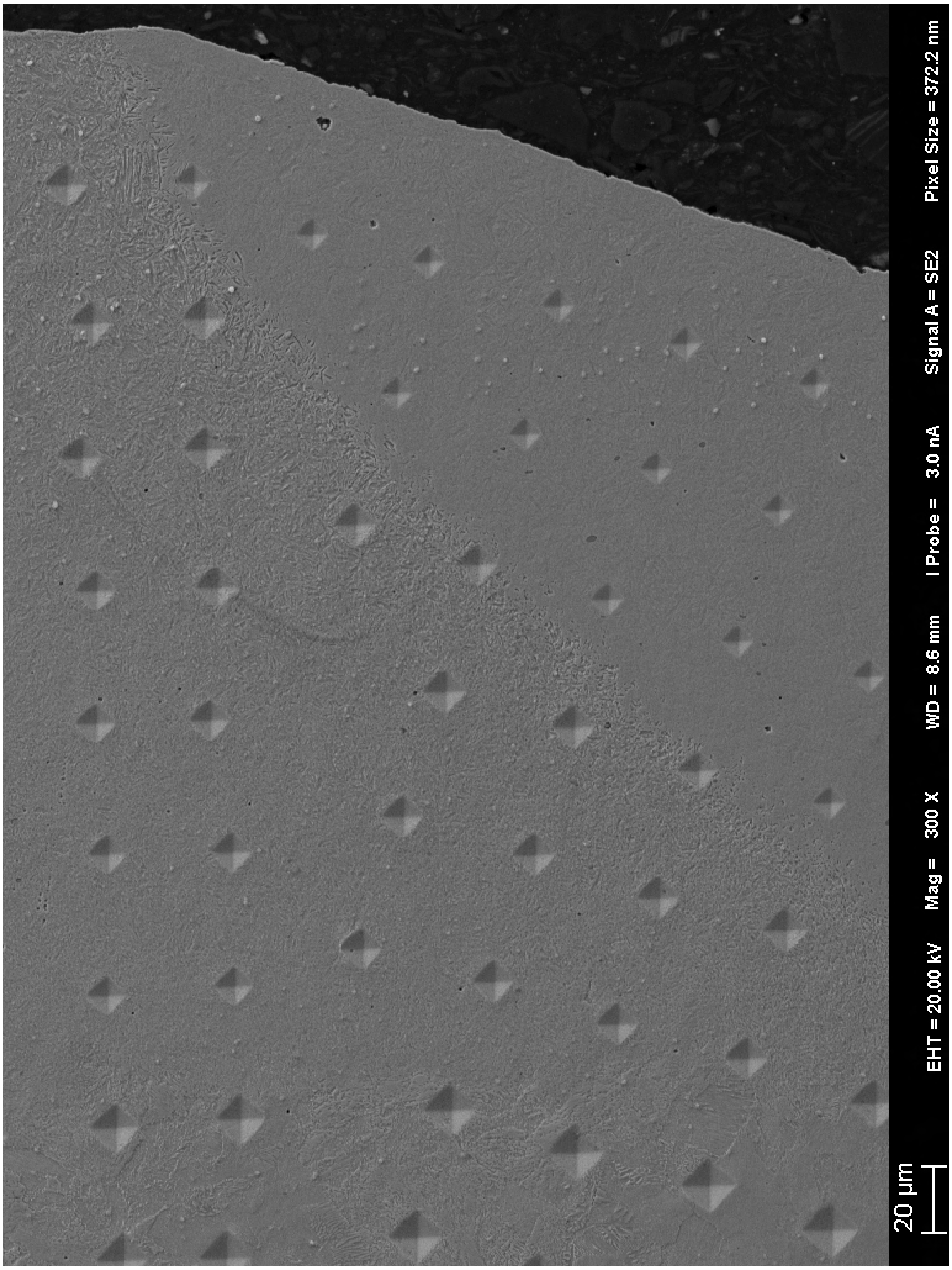

Figure 4.13: Overlapping martensitic layers at the corner of R260, 2500-F.

Figure 4.13 shows an image from SEM of the same overlap zone. Small indentations can be seen in the martensite layer of the second ground surface, indicating high hardness in this region. The adjacent zone has larger indentations and in the pearlite in left side of the picture, there are even larger indentations.

4.4 Depth of martensite layer

While the layers in most samples were relatively uniform in shape along of the cross-section, it is worth noting that the layers are thinner at the edges than in the middle part of the samples. Depth measurements taken on the transverse samples at locations shown in Figure 3.8, are presented in Table 4.7, for R260 and in Table 4.8, for R350HT. In the tables, L represents the values measured at the left edge of the layer, as they are seen in the pictures. M is measured in the middle of the layer and R at the right edge.

For depth measurements analyses,the measurements from the middle of the cross-sectional transverse samples are used, as the layers in all but one case (R260, 15000) have a relatively uniform shape when excluding the edges, and the middle measurements should be good representations of the depth with minimal influence of boundary effects. The measurements of R260, 15000 are included in the results, but should be considered less reliable.

	L	M	R
2500	365	382	359
5000	243	262	195
10000	85	136	71
15000	120	100	118
15000, 0.06	41	92	92
15000, 0.09	132	129	135

Table 4.7: Measured depths in R260 for different grinding conditions, in µm.

	L	M	R
2500	395	433	402
5000	209	255	222
10000	64	141	61
15000	49	98	33
15000, 0.06	114	112	105
15000, 0.09	128	133	138

Table 4.8: Measured depths in R350HT for different grinding conditions, in µm.

The measurements of the longitudinal samples will be used as a comparison to those of the transverse samples. The comparisons can be viewed in Figures 4.14 and 4.15, where the transverse measurements are symbolised by an asterisk and the longitudinal measurement range by a line.

The difference in layer depth in the longitudinal samples was also examined to see if it was possible to relate it to the phenomenon of the previously mentioned repeating grinding marks. While the layers do seem to have a slightly uneven profile, it was not possible to directly relate this to the frequency and position of the grinding marks. The boundary between the pearlite and martensite regions was not distinct enough, and the difference between peaks and valleys in the profile was too small to be able to distinguish a clear trend.

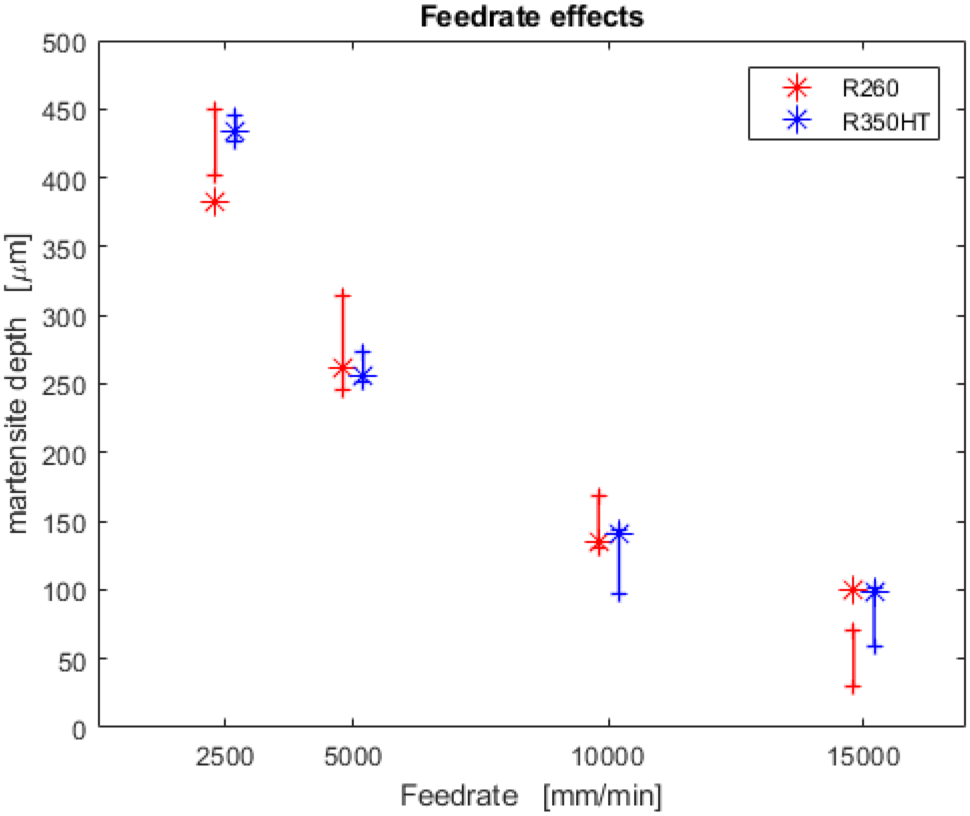

Figure 4.14: Martensite depth versus feedrate

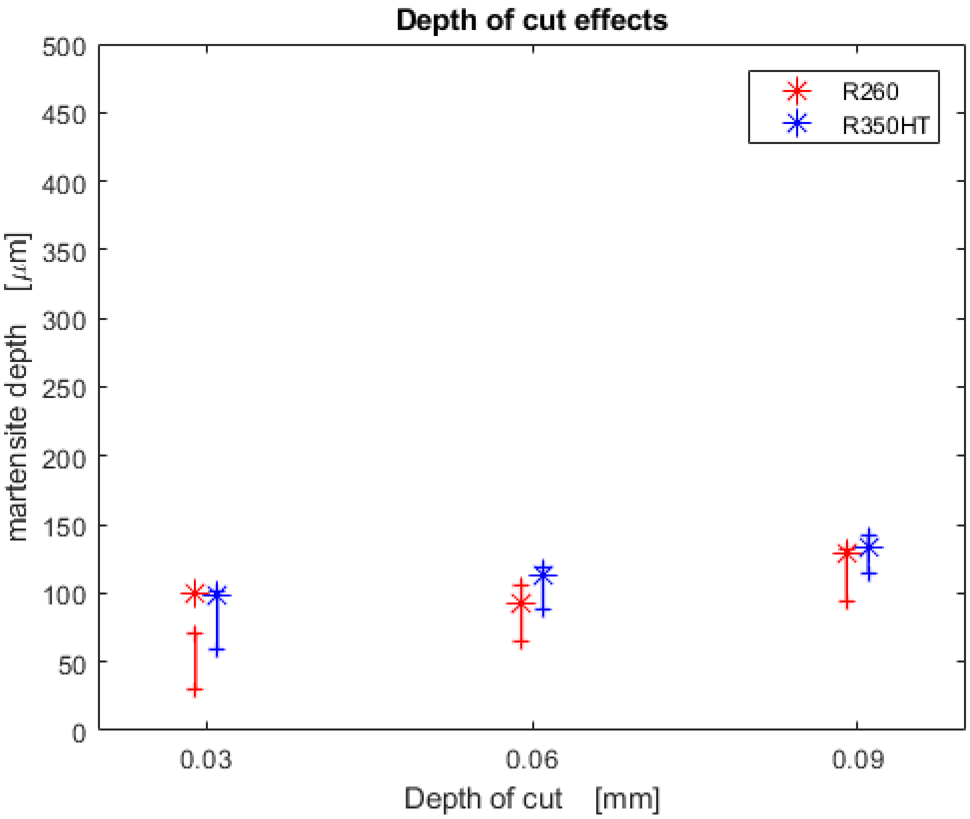

Figure 4.15: Martensite depth versus depth of cut

The results of the measurements say that for both R260 and R350, the martensite depth in the middle of the cross-sectional transverse samples consistently decreased with increasing feed rate.

The effect of an increased depth of cut, which was investigated using the feedrate 15000 mm/min, is a bit more difficult to determine. Based on the recorded values, it seems that an increased depth of cut also leads to a deeper martensite layer. However, this is not completely true for the switch from 0.03 to 0.06 mm in the transverse samples of R260, where there instead is a slight decrease. As previously mentioned, the measurements from the sample R260, 15000, 0.03 are considered less reliable. In the corresponding longitudinal sample, the depth follows the expected trend. As visualised in the graphs, the depth measurement of the transverse sample lies outside of the range of the longitudinal sample.

In the Depth of cut effect plot, the martensite layers are on average thicker in R350HT than in R260. The same trend cannot be seen in the Feedrate effect plot.

Dividing the middle depth measurement of the martensite layer from Tables 4.7 and 4.8 with respective contact area specific energy from Table 4.1 and taking the average for each material gives a number that multiplied with any contact area give a good estimation of the martensite depth. This is because the contact area specific energy should be close to proportional to the martensite depth (d_m). The average of the measured martensite layer divided by the contact area specific energy for the two materials is $3.275 * 10^{-5}$ for R260 and $3.596 * 10^{-5}$ for R350HT. The estimation d_{me} is created by multiplying the averaged d_m/E_c with the contact each samples contact area specific energy and is shown in table 4.9. Together with the error d_m/d_{me}.

Material	v [mm/min]	a [mm]	d_{me} [μm]	d_m/d_{me} [%]
R260	2500	0.03	420	-9
R260	5000	0.03	241	+9
R260	10000	0.03	120	+13
R260	15000	0.03	85	+18
R260	15000	0.06	111	-17
R260	15000	0.09	149	-14
R350HT	2500	0.03	403	+7
R350HT	5000	0.03	211	+21
R350HT	10000	0.03	132	+6
R350HT	15000	0.03	98	±0
R350HT	15000	0.06	133	-15
R350HT	15000	0.09	165	-19

Table 4.9: Estimated martensite depth based on the average measured martensite and contact area specific energy.

Depth measurements for each of the facet ground samples, in the different locations specified in Figure 3.9, are presented in Table 4.10. These results are not further analysed.

	1	2	3	4	5	6
R260, 2500, 0.03	168	326	206	323	308	252
R260, 15000, 0.09	77	138	77	129	131	113
R350HT, 2500, 0.03	144	340	204	333	326	236
R350HT, 15000, 0.09	92	171	106	149	141	116

Table 4.10: Depth measurements of the facet ground specimens, in µm.

4.5 Cracks

In sample R260, 5000, transverse cracks were found on the surface. Figure 4.17 shows the approximate area where they were observed on the sample surface. When averaging the distance between the cracks, measured along a line which crosses each crack at an equal distance from the edge, the result is 2115.4 µm. This is close to the distance between revolutions which has been previously calculated (2230 µm). However, the deviation in distance of the individual measurements between cracks is large and ranges from 1483 to 2775 µm.

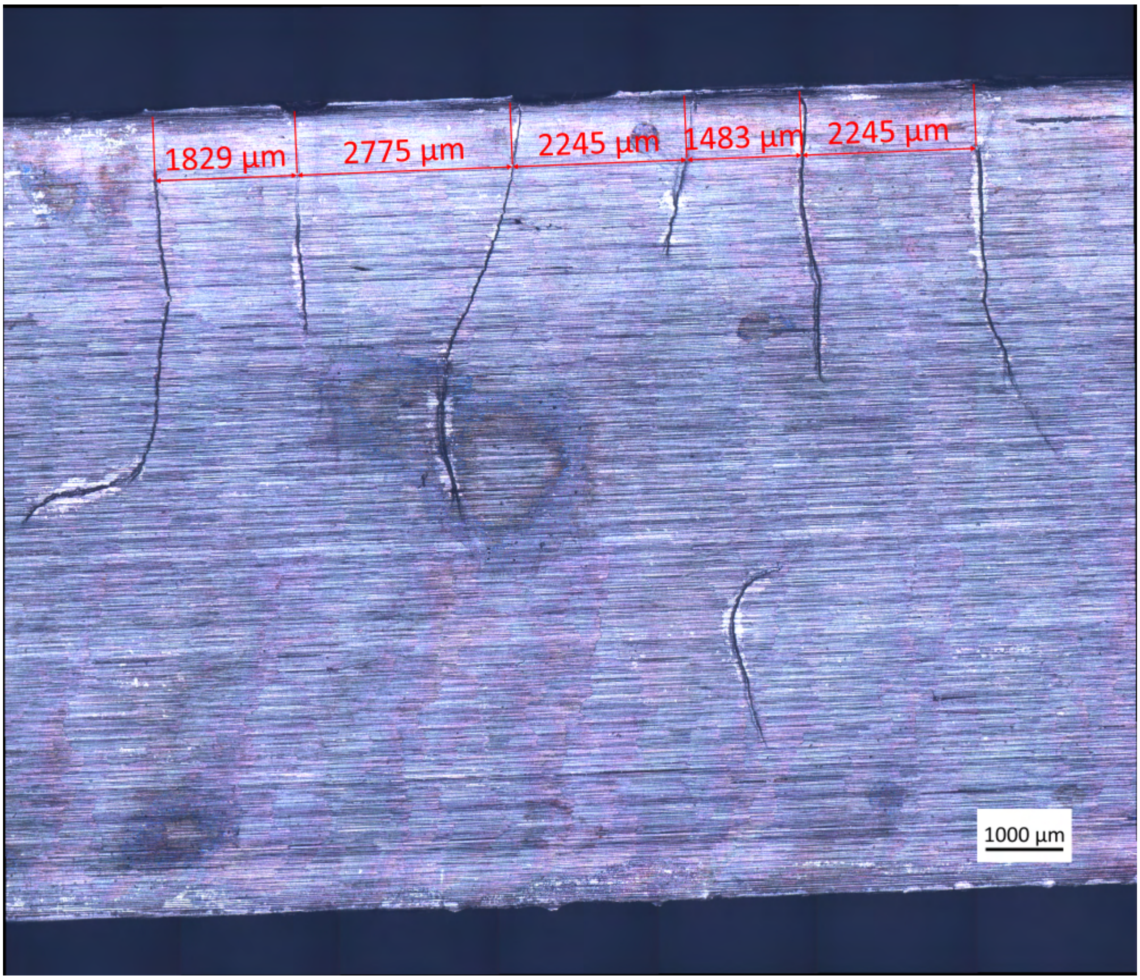

Figure 4.16: Cracks on the surface of R260, 5000, with measurements.

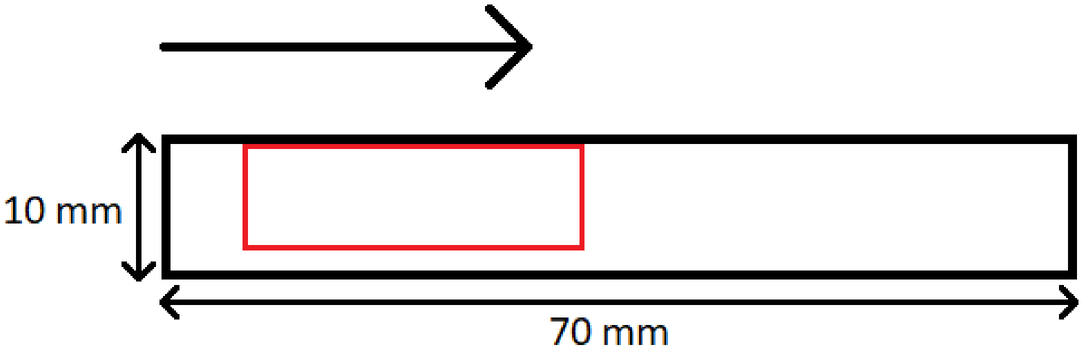

Figure 4.17: The approximate location of the surface cracks on R260, 5000, indicated by the red box. The arrow shows grinding feed direction.

Figure 4.18 shows cracks in the transverse sample taken from the same specimen. Here it can be seen how the cracks propagate through the martensite layer and stop when they reach the pearlite region.

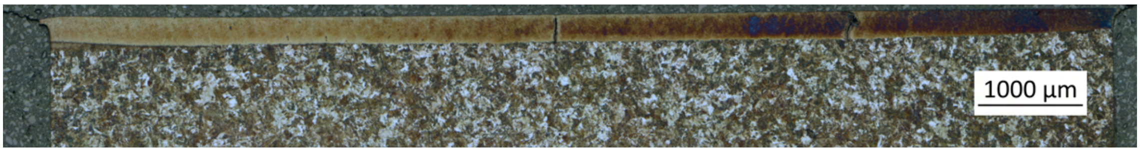

Figure 4.18: Transverse cross-section of sample R260, 5000 mm/min.

Close-ups of these cracks, as seen in SEM, are shown in Figures 4.21, 4.22, 4.19 and 4.20. In relation to Figure 4.18, the images are rotated 45° anti-clockwise. Here it can be seen that the cracks only reach approximately 40 µm into the pearlite in 4.19 and 4.20 and approximately 20 µm in 4.21 and 4.22.

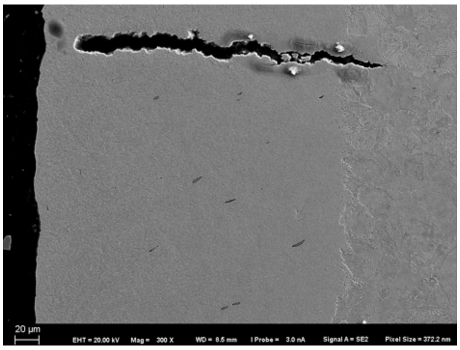

Figure 4.19: SEM image of a crack.

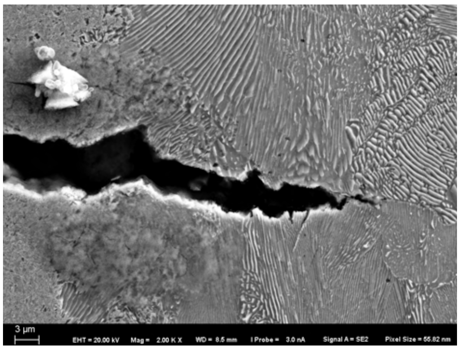

Figure 4.20: Close-up of crack in 4.19.

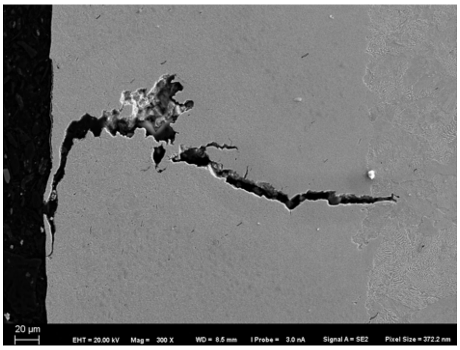

Figure 4.21: SEM image of a crack.

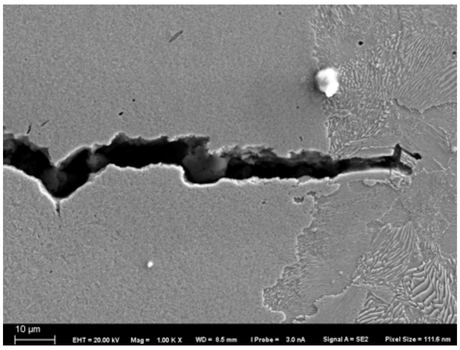

Figure 4.22: Close-up of crack in 4.21.

Smaller cracks, growing almost parallel to the surface at depths of only a few µm were found in some samples. An example of this can be seen in Figure 4.23. In this state, the crack is not deemed to cause any major damage because of the very small volume that would break off. However, cracks like this could cause issues if they instead grew deeper into the material and eventually broke off. Cracks can also appear deeper in the martensite layer, without an origin at the surface.

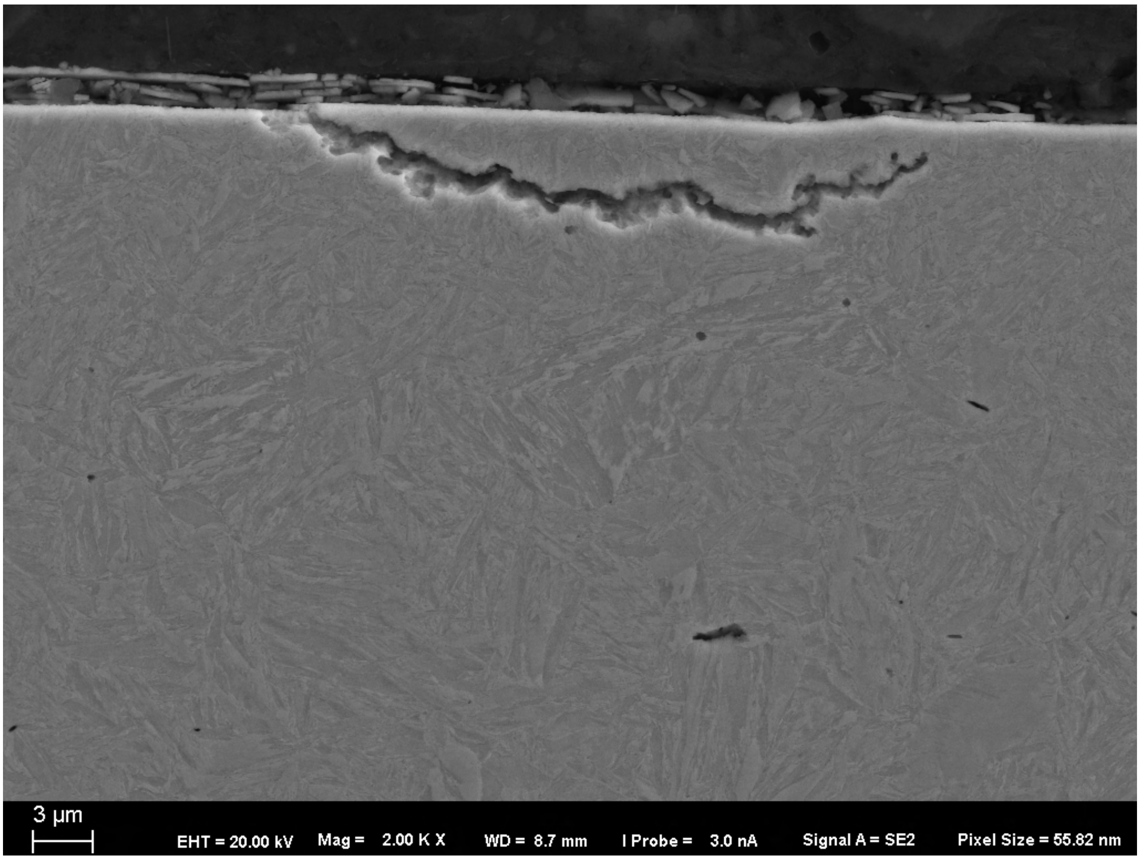

Figure 4.23: Small crack in the martensite layer. R260, 5000-L.

In several samples, a crack parallel to the surface, growing from the edge of the sample, were found in the martensitic layer. One example of this is shown in Figure 4.24. This is assumed to occur in the specimens because of their shape, where the sharp edge has deformed during grinding and stresses are induced. This should not be an issue in real life grinding, as the geometry of the rail head would prevent this type of crack.

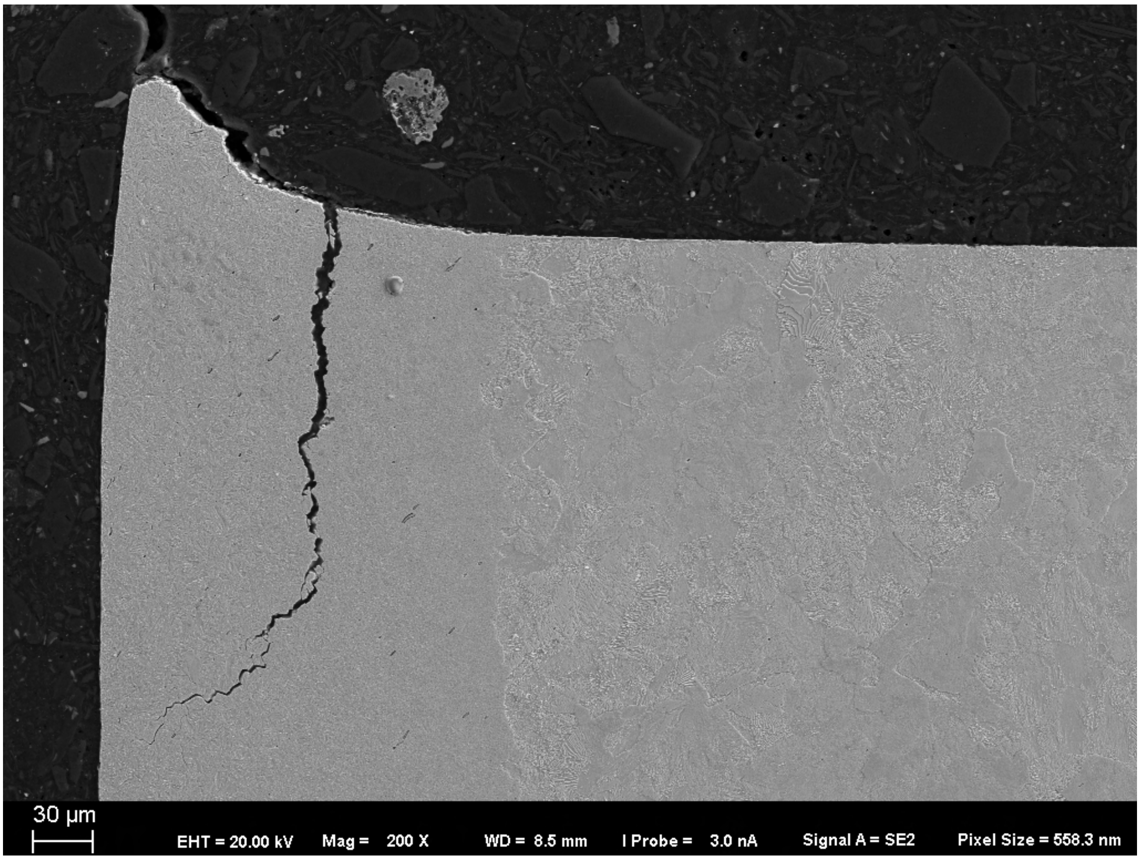

Figure 4.24: Crack in the martensite layer of R260, 5000, growing from the side.

4.6 Hardness

The results of the hardness tests are presented in Figures 4.25 and 4.26. The indentations made in the martensite layer of the samples gave hardness results which fall within a reasonable range for martensite [25]. The sharp decrease in hardness seen in the graphs as the distance from edge increases is due to the shift from martensite to pearlite in that region.

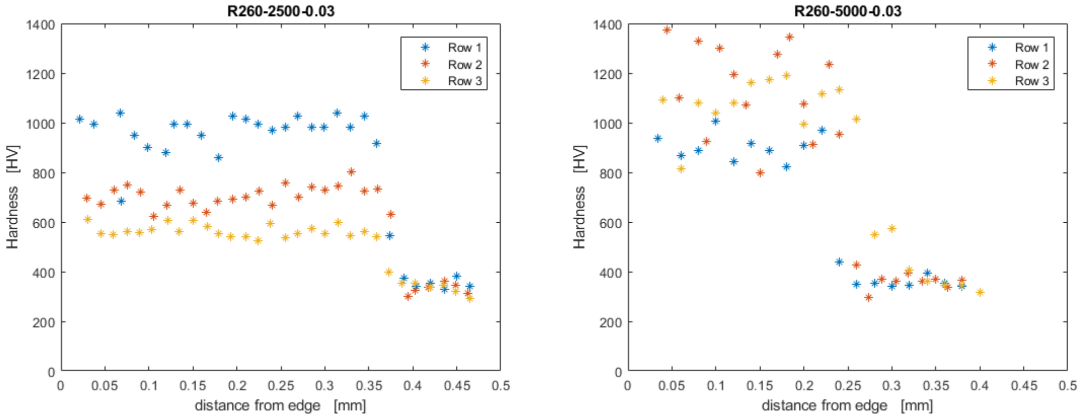

(a) Feedrate: 2500 mm/min
Depth of cut: 0.03 mm

(b) Feedrate: 5000 mm/min
Depth of cut: 0.03 mm

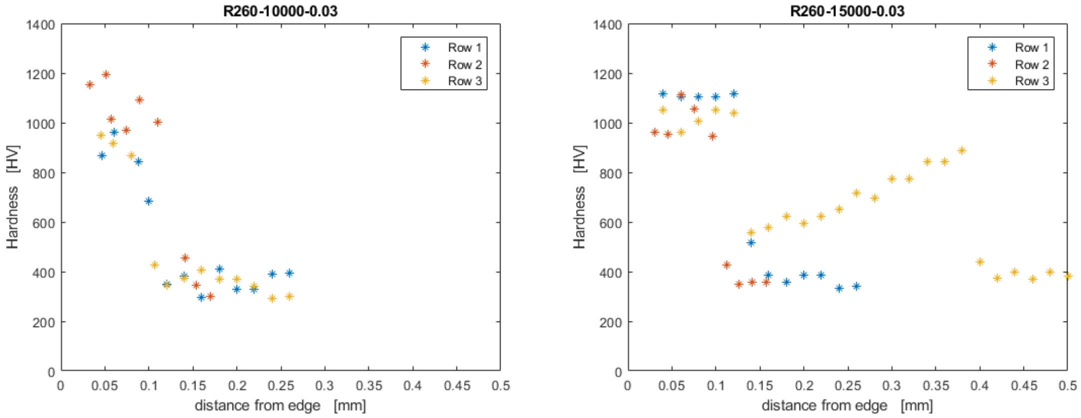

(c) Feedrate: 10000 mm/min
Depth of cut: 0.03 mm

(d) Feedrate: 15000 mm/min
Depth of cut: 0.03 mm

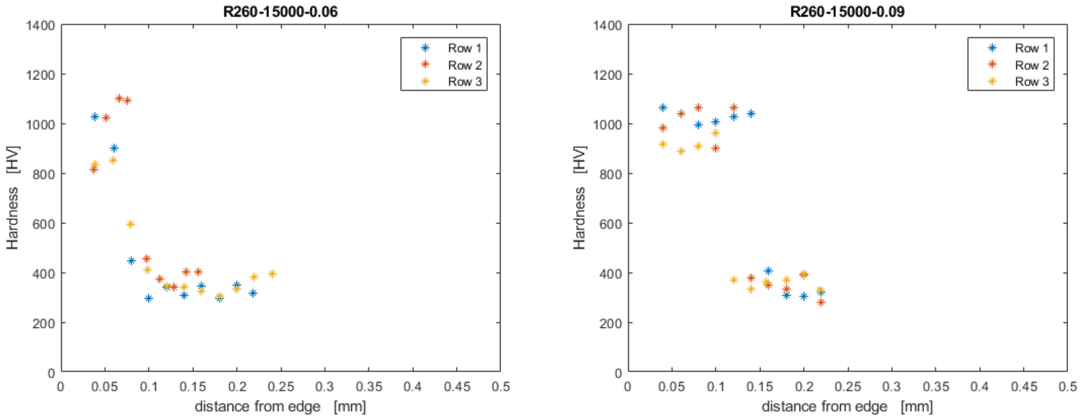

(e) Feedrate: 15000 mm/min
Depth of cut: 0.06 mm

(f) Feedrate: 15000 mm/min
Depth of cut: 0.09 mm

Figure 4.25: Hardness results of R260 samples.

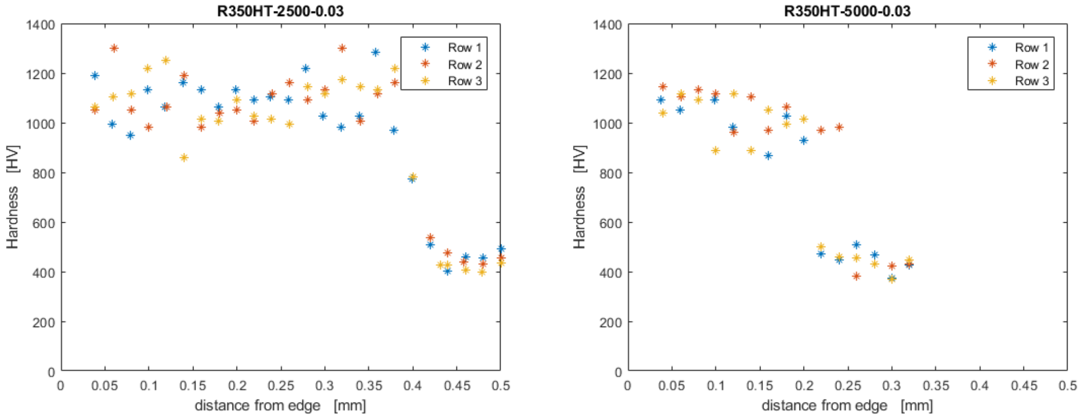

(a) Feedrate: 2500 mm/min
Depth of cut: 0.03 mm

(b) Feedrate: 5000 mm/min
Depth of cut: 0.03 mm

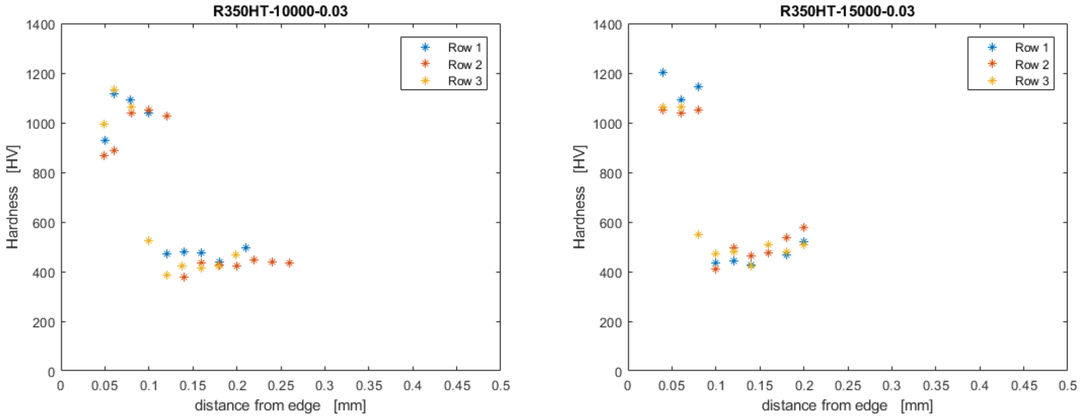

(c) Feedrate: 10000 mm/min
Depth of cut: 0.03 mm

(d) Feedrate: 15000 mm/min
Depth of cut: 0.03 mm

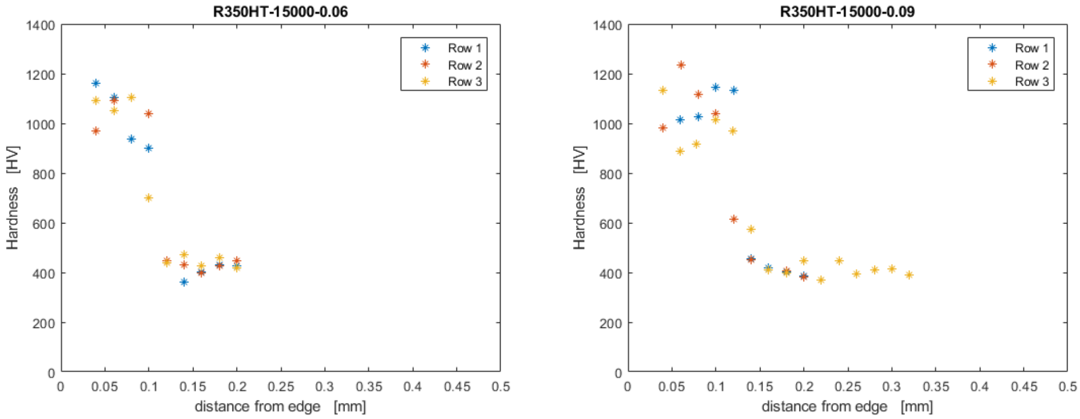

(e) Feedrate: 15000 mm/min
Depth of cut: 0.06 mm

(f) Feedrate: 15000 mm/min
Depth of cut: 0.09 mm

Figure 4.26: Hardness results of R350HT samples.

Within the martensite layers and in the pearlite region, the hardness values are similar regardless of the depth they were measured at. Table 4.11 shows a comparison of the hardness mean values of the two grades. Some of the hardness results presented in the graphs were excluded in the mean value calculations. The results of sample R260, 2500, seen in Figure 4.25a, were completely removed because of the gradient switch from bright to darker colors in the layer observed in Figure 4.5, and the clear difference in hardness between indentation rows. The results from row 3 in R260, 15000, seen in Figure 4.25d, were also removed because of the brown zone above the martensite layer seen in Figure 4.8. Additionally, the 10 lowest and the 10 highest values found in both the martensite and the pearlite regions in each grade were excluded. As the indentations in some cases are in the transition zone of the two microstructures, values above 600 HV were classified as martensite and values below were classified as pearlite. The results show that the hardness mean values for both martensite and pearlite are higher in the head hardened R350HT. The difference between the tro grades is 44 HV in the martensite layer and 81 HV in the pearlite. Important to note is that the standard deviation for the martensite hardness for both grades is high. As previously stated in Table 2.2, the expected hardness in the rail grades is in the range 272-318 HV (mean 295 HV) for R260 and 372-412 HV (mean 392 HV) for R350HT. The table also shows the difference in % between the mean of expected hardness and the measured mean hardness in the pearlite.

	R260	R350HT
Mean value hardness (HV) martensite	1014	1058
Standard deviation hardness (HV) martensite	86.6	68.3
Mean value hardness (HV) pearlite	360	441
Standard deviation hardness (HV) pearlite	28.3	28.4
Mean value difference hardness (HV) pearlite	22%	12.5%

Table 4.11: Mean hardness values from hardness test of transverse samples

Hardness tests were also done on the facet ground samples. In Figure 4.27, the results of R260, 2500 are plotted onto the picture of the sample. Hardness results for the remaining facet ground samples can be found in Appendix C. The results clearly show that there is a zone in the layer from the first grinding session that is significantly softer than the rest of the layer. As mentioned before, this is result of tempering.

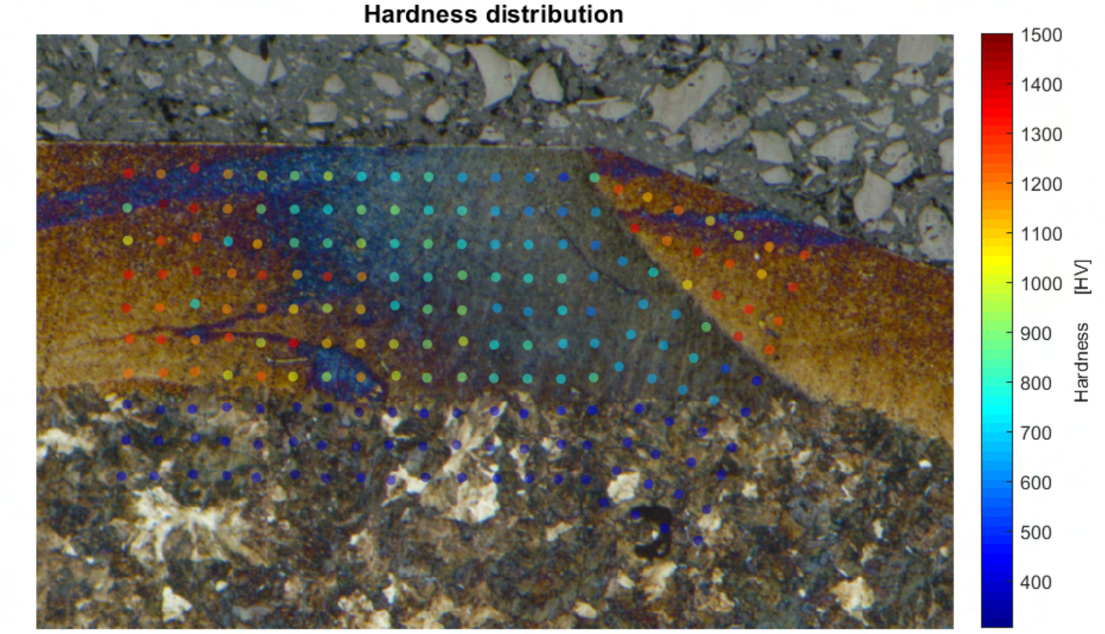

Figure 4.27: Hardness test of a facet ground sample, R260, 2500.

4.7 Analytical simulations

By using equation 3.2 in a 100 by 100 grid for material R260 with feedrate 2500 mm/min and depth of cut 0.03 mm, Figure 4.28 and Figure 4.29 are created, where Figure 4.29 is the result when the heat input is adjusted to match the measured martensite depth. Figure 4.28 is created using the heat input from the grinding machine. Results from the other feedrates, depth of cut and material are seen in Appendix B.

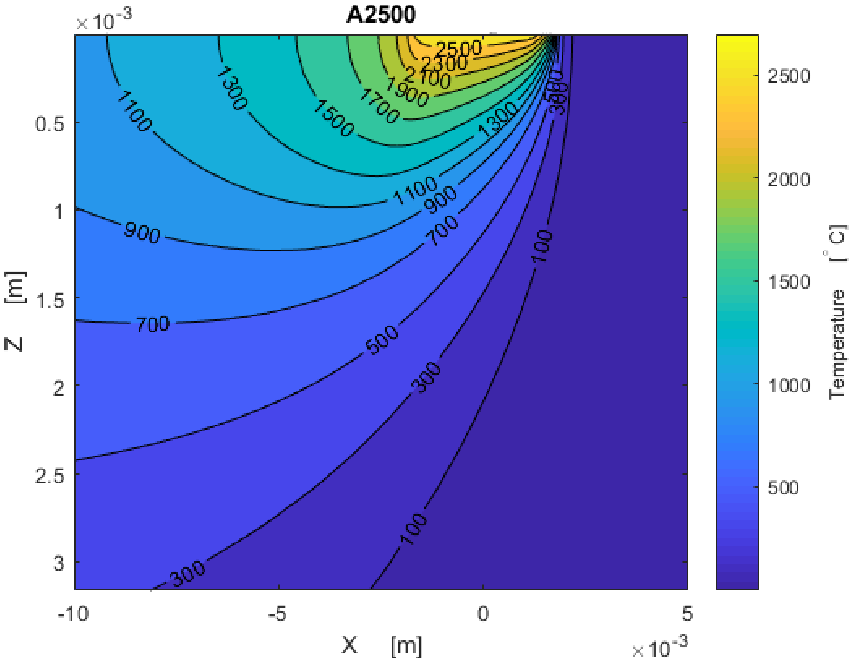

Figure 4.28: Heat distribution by analytical formula, with power from the grinding study

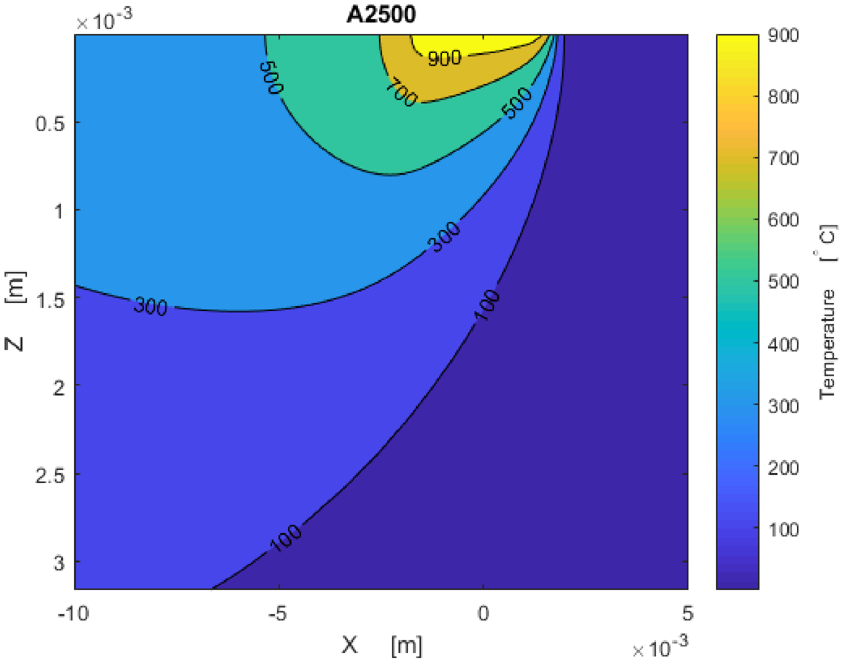

Figure 4.29: Heat distribution by analytical formula, with power iterated to match martensite depth

The power iterated to match the martensite depth (Q_{ga}) for all the samples and the heat partition (ϵ_a) that would give the same result as the iterated power can be seen in table 4.12.

Material	v [mm/min]	a [mm]	Q_g [W]	Q_{ga} [W]	ϵ_a
R260	2500	0.03	5337	1862	0.314
R260	5000	0.03	6140	2576	0.378
R260	10000	0.03	6124	3262	0.479
R260	15000	0.03	6480	3891	0.540
R260	15000	0.06	8453	4415	0.470
R260	15000	0.09	11394	5097	0.402
R350HT	2500	0.03	4675	1985	0.382
R350HT	5000	0.03	4882	2542	0.469
R350HT	10000	0.03	6135	3304	0.485
R350HT	15000	0.03	6815	3877	0.512
R350HT	15000	0.06	9215	4636	0.453
R350HT	15000	0.09	11472	5181	0.406

Table 4.12: Power from the machine, power iterated to match the martensite depth and heat partition that would produce the same result

4.8 Finite element simulations

In finite element, the heat distribution can be seen in Figure 4.30 for R260 with feedrate 2500 mm/min and depth of cut 0.03 mm. The power was set as the power to match the martensite depth from analytical simulations seen in Table 4.12. Results for the other feedrates, depths of cut and material are included in Appendix A.

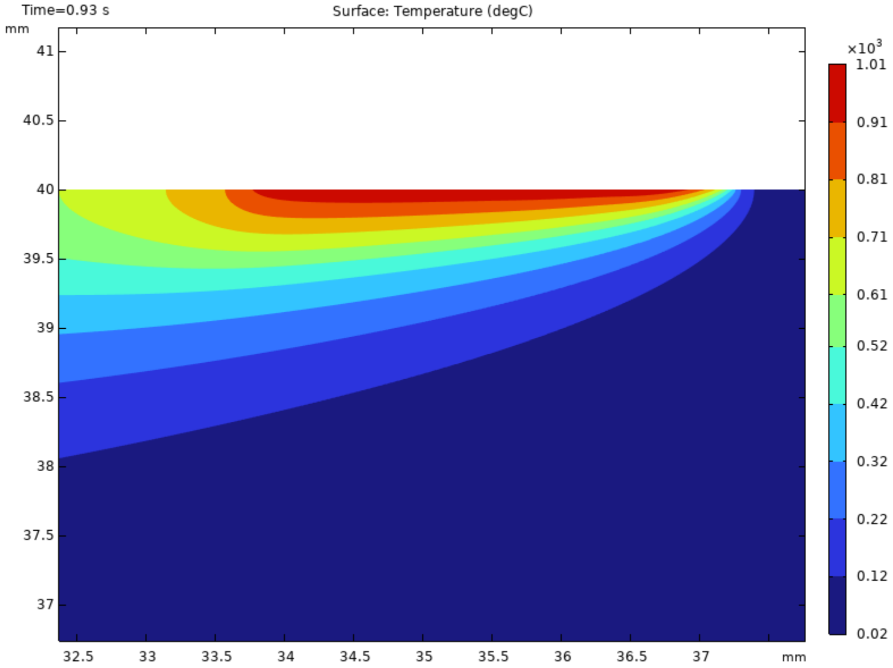

Figure 4.30: Heat distribution for sample R260, 2500 mm/min obtained with finite element method.

The temperature of a point 0.2 mm from the ground surface is also plotted versus time.

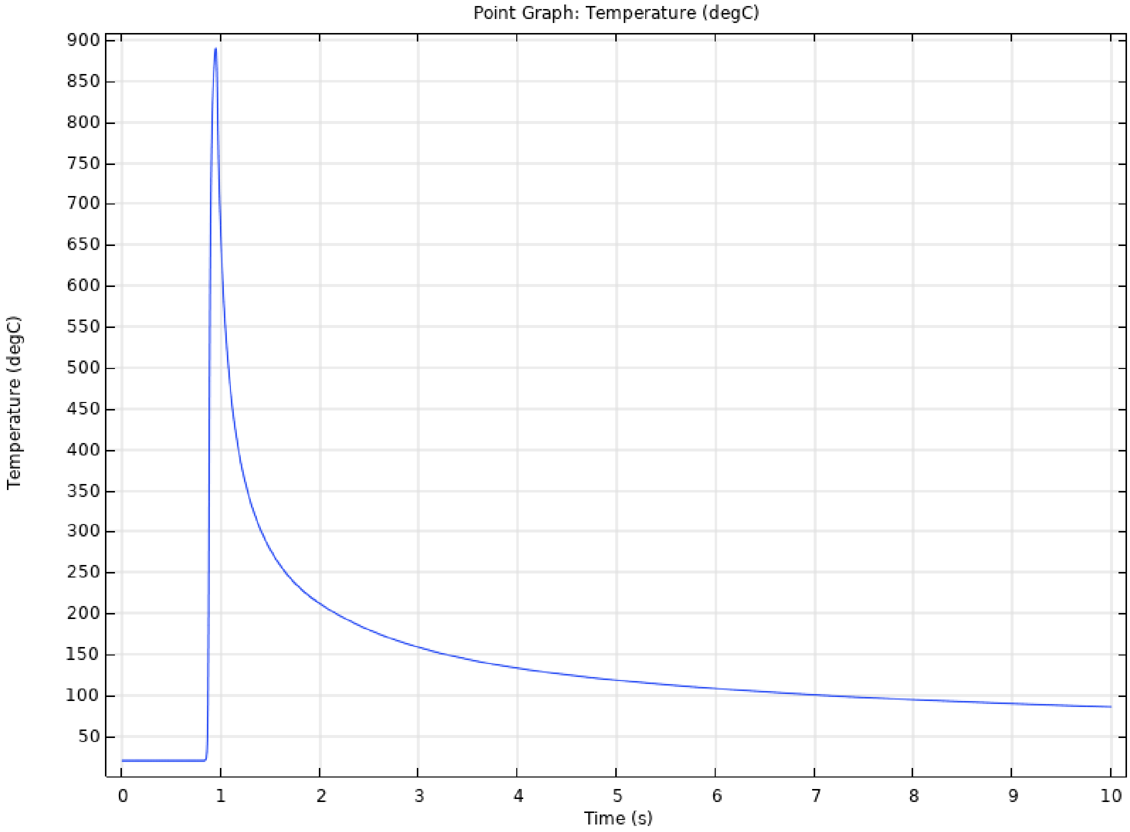

Figure 4.31: Temperature of a point 0.2 mm down from the ground surface. Grinding done with feedrate 2500 mm/min, depth of cut 0.03 mm on material R260 with the iterated power

5

Discussion

In this chapter, the obtained results are discussed. Explanations and/or theories are presented for the different phenomena. In some cases, no explanations could be provided. Additionally, comparisons to other studies are included and a few important differences between this study and regular railway grinding are described.

5.1 Assumptions

The martensite formation is expected to be purely thermal as plastic deformation should not contribute to the effect, in this study. With uniform layers achieving a significant thickness, it can be assumed that it is caused by elevated temperatures.

5.2 Differences between rail grinding and this study

- Typically, grinding stones used in field have an outer diameter of 250 mm [1], p. 61. The wheel used in this study is 400 mm in diameter, made to fit the grinding machine used, while having the characteristics of a common rail grinding stone. But, the main difference concerning the wheel is its orientation during grinding. Most descriptions of the railway grinding process involve so called face grinding, instead of peripheral grinding, which was used for this study. This difference could have an effect. For instance, face grinding will likely have a larger contact length and therefore a bigger contact surface. A longer contact length might require a faster feedrate in order not to increase the specific energy. A longer contact length also means longer contact time which for the same specific energy would reduce the temperature.
- The corners produced between facets in this study, as depicted in 3.4 are sharper than the corners between facets in a regular rail profile. One reason to do this is to investigate how the material reacts to multiple grinding passes. This includes the effect of tempering the already existing martensite by creating overlapping heat affected zones. It is, however, important to remember that this effect likely would look different in real life and is not possible to directly translate to a real life scenario.
- The feedrates used during this study, 2500-15000 mm/min, which equals 0.15-0.9 km/h, are significantly slower than the commonly used train speeds during railway grinding. This caused thicker martensite layers than what would be produced during grinding in real life.

5.3 Surface

5.3.1 Surface roughness

The surface roughness results were different than expected. A study with similar experiments found that increased feedrate lead to increased surface roughness [26]. However, the measurements previously presented in the Results chapter seemed to indicate the opposite, meaning that the increased feedrate generally produced a less rough surface. No clear answer to why this occurs can be provided.

5.3.2 Discoloration

The discoloration of the specimen surfaces is related to a phenomenon called bluing. Bluing is known to occur during rail grinding, when the grinding trains are run at speeds that are below 2.5 km/h [1], p. 79. The train speed can be translated to feedrate. As the feedrates used in this study correspond to train speeds in the range 0.15-0.9 km/h, the results seem to be in agreement with the statement above.

Another example of discoloration, described as surface burn, of rail surfaces is mentioned in [27] where using a "feedrate" of 1 km/h resulted in some blue discoloration on the surface. The experiments that produced these results were not conducted in the same way as the ones described in this report, and the surfaces look different in general. Additionally, the temperatures [27] suggested to be related to the phenomenon do not align with the temperature simulations presented earlier in this report. This means that no conclusions can be made but the similarities are worth noting.

The periodic pattern appears to be correlated to the grinding wheel's revolutions. It is suspected that the out-of-roundness of the wheel creates oscillations in the grinding wheel. The oscillations would cause uneven grinding that could show in the surface color.

5.3.3 Surface cracks

Several cracks were observed on the surface of R260, 5000, shown in Figure 4.16. As this phenomenon was not observed on any other specimen, it can be assumed that something different occurred during grinding of this particular specimen. The average spacing between the cracks is close to that of the periodic pattern so one theory is that the phenomenon can be related to the wheel's suspected oscillations.

5.4 Martensite layers

5.4.1 Planar grinding

As described, the martensite depth was measured at multiple locations in the specimens and was found to be roughly the same along the longitudinal middle line.

Therefore, it was deemed sufficient to only analyse the measurements of one transverse sample, and the longitudinal sample, for each ground specimen. The variation of martensite depth within the specimens appeared to be low that presenting measurements from multiple locations would be redundant.

The martensite layers in the transverse samples were relatively uniform in thickness along most of the surface, but in some samples the layers attenuated close to the edges. The reason for this is unclear. The thermal conductivity of steel is so much higher than that for air that the surrounding environment should not contribute to faster cooling close to the edges. It could, however, be explained by the slight deformation of the edges which can be seen in Figure 4.24. The corners of the specimens had during grinding slightly extended and curved over the edges. This might lead to less energy required to grind away the material. The phenomenon is not deemed to be generally important to this study.

5.4.2 Facet grinding

In Figure 4.11, which shows a transverse facet sample, the martensite layer on the angled side clearly decreases in thickness both close to the edge and the corner. This shape is caused by the fact that heat can conduct not only perpendicular to the surface but also to the sides, as shown in Figure 5.1.

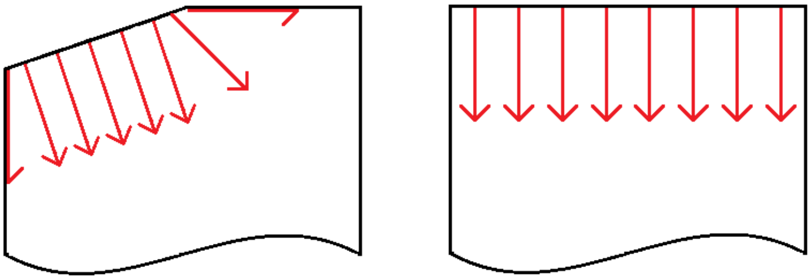

Figure 5.1: Heat input distribution for faceted and planar samples.

5.4.3 Tempered martensite

The layers were expected to be appear bright in microscopy. However, in some cases, their appearance varied from bright to darker, brown shades. When it comes to sample R260, 25000 (Figure 4.5)), the gradual shift from the expected bright appearance to a darker shade is assumed to be because of tempering effects. The darker shades occur because tempered martensite reacts differently to etching, being less resistant to the etchant [28]. The SEM images, Figure 4.6, taken in the darker region, and Figure 4.7, taken in the bright region, show that the texture has a higher contrast in the assumed tempered area than in the as-quenched martensite, indicating that etching has been more efficient in the tempered region. In this case, the effect was likely caused by elevated temperatures during cutting while preparing samples for microscopy, resulting in the martensite partly being tempered. It is therefore not an effect of the grinding tests. However, this does provide an insight in how the microstructure can quickly change when exposed to high temperatures.

The hardness test results, which can be viewed in Figure 4.25a can further motivate a tempered state. The difference in hardness between the left and right side is large. The side with as-quenched martensite has results around 1000 HV while the other has results around 550 HV.

As for the phenomenon found on R260, 15000, shown in Figure 4.8, where there are darker regions sandwiched between the bright martensite layer and the pearlite, the darker region is also most likely tempered martensite. A thick layer of martensite might have formed at some point during the grinding tests, and not been sufficiently removed, but instead tempered during the following grinding session. Perhaps the specimen became slightly skewed at some point. This could also explain the uneven layer. The hardness results of this sample can be viewed in 4.25d. In the presumed tempered martensite region, the range is 559-888 HV. This can be compared to hardness tests conducted on brown etching layers (BEL) in R260Mn rail [29] which gave similar results, ranging from 542.6 ± 26.4 HV to 840.6 ± 32.9 HV. It is suggested that the BEL is tempered martensite. In the article, the hardness of WEL is also measured. The result was around 882.7 ± 63.3 HV, which is lower than the hardness results (946-1118 HV) of the martensite layer in the discussed sample.

5.5 Hardness

There is a difference between expected hardness in the pearlite and the measured hardness. This is probably because the hardness indentations were made and measured on an already etched surface. This made the hardness indentations blurry and difficult to measure. To facilitate measurements, the focus of the microscope was adjusted. This approach appears to, in general, increase the hardness. The same problem occurred with the hardness measurements in the martensite layer, and since the indentations are smaller in the martensite, this effect has an even bigger impact. So, in general, the measured hardness is likely higher than the real hardness. Relative hardness between samples should still be comparable even if there can be differences in how much etching has affected the samples.

For Table 4.11, 600 HV was chosen as the divider between martensite and pearlite and the 10 highest and lowest values of both pearlite and martensite were removed. The divider was chosen since the hardness of martensite is expected to be much higher than the hardness of pearlite. Changing the divider hardness would change the result but 600 HV is likely a good divider since the lowest martensite hardness away from the transitioning zones is visually estimated to around 800 HV from Figures 4.25 and 4.26. For pearlite the highest value is estimated to be around 400 HV.

5.6 Temperature and cooling rate estimations

The cooling rate from the austenite phase controls the microstructure of the material. The actual cooling rate during grinding was not measured. However, calculations could be made using FEM. From Figure 4.31 it can be seen that most of the cooling happens during the first second where the temperature goes from around 900 °C to around 220 °C. As can be seen from Figure 2.3, the martensite starts to form at around 160 °C. This temperature is reached approximately two seconds after the heat source has passed the point. This cooling rate is significantly faster than 20 °C/s, which would be the limit for when pearlite could start to form according to the CCT diagram.

The calculations in JMatPro, seen in Figure 2.3 and Figure 2.4, estimated an austenitisation temperature of around 735 °C for both grades. Based on this estimation, and the measured martensite layer depth, a FEM model was made to find the temperatures in the material. However, since no measurements of the actual temperatures were made during the grinding process, there is no way of verifying the results of the model.

5.7 Martensite layer thickness prediction

Using the power from the machine does not seem to work with either finite element method or with the analytical formulas. Both methods result in temperatures that are way above the melting temperature for the material with the assumed heat partition of 90%. To reach the power that would match the measured martensite depth with the power from the machine, the heat partition that enters the workpiece would be in the range 31% to 55% as can be sen in table 4.12. This number is usually in the range 60-90% [22] and in this case, where no coolant was used, it is expected to be in the upper part of this range. So the heat partition is likely not the solution.

The grinding wheel has been assumed as stiff. This is not true and deformations in the grinding wheel and workpiece could result in a significantly larger contact area. A larger contact area would enable a higher spread of the heat and bring the simulation result closer to the measured result. There are studies that suggest that the actual contact length is around 2-3 times higher then the geometrical one [30]. This has been done in Figure 5.2, where the contact length is assumed to be 2.5 times higher then the theoretical.

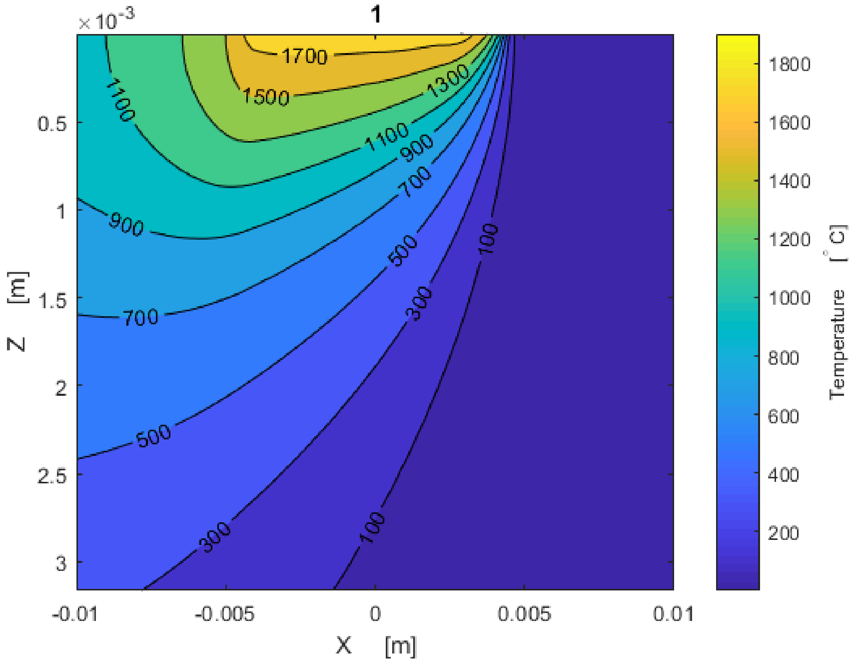

Figure 5.2: Temperature distribution when contact length is 2.5 times the theoretical contact length. Material: R260, Feedrate: 2500mm/min, depth of cut: 0.03 mm, Power from the grinding machine

Comparing this to Figure 4.28, the surface temperature drops a lot. Temperatures above the melting point should not be possible so the fact that the maximum surface temperature drops seems promising. But the temperature iso-curve for 700 °C has only moved marginally, meaning that the error for expected martensite depth is close to the same. The error between measured martensite layer thickness and the simulated layer thickness is highest for the lowest feedrate and then decreases with increasing feedrate. Deformation of the wheel should be proportionate with the force which should be increasing with an increasing feedrate. So deformation of the wheel should not be the main source of error since the error does not match the expected force. It is still possible that deformation of the grinding wheel matters in some way.

The grinding energy distribution was chosen to create an even surface temperature. This would result in a martensite layer thickness that is quite low since the heat is more evenly spread. There are arguments for this type of energy distributions, such as where the material removal rate is on the wheel and how the mechanical properties of the material changes with temperature. The real heat distribution is unknown but reasonable changes in heat distribution do not make a large difference to martensite layer thickness but could increase the maximum surface temperature.

The material data in the analytical simulations were calculated based on temperatures of the previous heat step, For a non infinite number of heat steps this will lead to an error. Since the α is mostly decreasing in the relevant temperature interval it is likely that the average α is slightly higher then the correct value leading to higher values for temperatures. For thermal conductivity this could be true as well but the curve for thermal conductivity is not as clearly decreasing or increasing, the number of heat step has a more unclear effect on the result. Overall the effect of this is assumed to be quite small.

5.8 Suggestions/recommendations

Due to discrepancies in the grinding process, and the results of the facet grinding, it was also found that tempered martensite can form by multiple heat inputs over the same area. If the previously formed martensite is not fully removed by following passes and the heat reached the A_1 temperature, it could also lead to re-austenitisation, followed by a new martensite layer forming. Tempered martensite is softer than as-queched martensite, which could be beneficial, specifically in terms of preventing cracks. However, it is still undesirable since the original pearlitic microstructure is preferable.

In Table 4.1, it can be seen that the specific energy is decreasing for an increasing feedrate and decreases further with increased depth of cut. The high specific energy for low feedrates is likely because the grinding stone slides against the surface and the friction gives rise to an energy loss.

The feedrates used during this study are relatively slow speeds, the highest being 15000 mm/min (0.9 km/h). It is evident from the tests, that slower feedrates yield thicker martensite layers. This serves as confirmation that slower grinding procedures can have detrimental effects on the rail surface. The possibility of unpredicted effects, thermal or other, when using significantly higher feedrates also need to be considered. However, purely based on the results in this study it would be recommended to use high speeds to avoid thick WEL.

With the deeper cut, the martensite layers grew thicker. As mentioned, it is these days preferred to use preventive grinding, where only a thin layer is removed, but with shorter grinding intervals.

6

Conclusion

Martensite layers formed on every ground specimen. The layers were proven to be martensitic by examining the appearance of the microstructure and measuring the hardness. The martensite layer depth depends on feedrate and depth of cut. Increasing the feedrate leads to a thinner layer, and increasing the depth of cut leads to a thicker layer. Considering that limiting the martensite formation would be preferable, a higher speed/feedrate should be recommended for rail grinding.

No major difference caused by the effects of grinding could be established between the two grades R260 and R350HT. The two materials seem to react in similar ways to different parameters. The differences that occur seem random and/or accidental, and there is no clear trend that can be proven to be true.

Large cracks and tempered martensite could be found in some planar samples, but both of these phenomena are caused by unknown factors or errors during the study, and are likely not general issues when it comes to rail grinding.

Analytical and finite element simulations were not able to give a usable result with the power recorded with the machine. Further studies need to be done in order to see how grinding power corresponds to martensite depth.

Many parameters and conditions, which in reality would effect the results, were not included in this study. To gain more knowledge and understanding of the topic, more research should be done. Suggestions for future studies include:

- The potential mechanical impact on martensite formation.
- Stresses within the material due to grinding.
- The effect of even higher feedrates
- Comparison to specimens from non-virgin rail.
- Temperature measurements during the grinding operation to improve the models used in this report.

Bibliography

[1] Zarembski, A. M. (2005). *The Art and Science of Rail Grinding* (First edition). Simmons-Boardman Books, Inc.

[2] Lundén, R., and Paulsson, B. (2009). Introduction to wheel-rail interface research. In R. Lewis and U. Olofsson (Eds.), *Wheel-rail interface handbook* (p. 9). Woodhead Publishing Limited.

[3] International Union of Railways. (2015). *UIC Code 721. Recommendations of the use of rail steel grades* (Third edition).

[4] International Union of Railways. (2002). *UIC Code 712. Rail defects* (Fourth edition).

[5] Wu, J., Petrov, R. H., Naeimi, M., Li, Z., Dollevoet, R., and Sietsma, J. (2016). Laboratory simulation of martensite formation of white etching layer in rail steel. *International Journal of Fatigue,* 91. https://doi.org/10.1016/j.ijfatigue.2016.05.016

[6] European Committee for Standardization. (2017). *Railway applications - Track - Rail - Part 1: Vignole railway rails 46 kg/m and above.* (EN 13674-1:2011+A1:2017).

[7] Turan, M. E. Ozcelik, S., Sun, Y., Ahlatci, H. and Cetin, M. (2016). Residual Stress Measurement in R260 and R260mn Quality Rails. 3. Uluslararası Raylı Sistemler Mühendisliği Sempozyumu. https://www.researchgate.net/publication/322301094

[8] Clayton, P., and Allery, M. B. P. (1982). Metallurgical aspects of surface damage problems in rails. *Canadian Metallurgical Quarterly,* 21(1), 31–46. https://doi.org/10.1179/cmq.1982.21.1.31

[9] Dikshit, V., Clayton, P., and Christensen, D. (1991). Investigation of rolling contact fatigue in a head-hardened rail. *Wear,* 144(1–2). https://doi.org/10.1016/0043-1648(91)90008-I

[10] European Committee for Standardization. (2018). *Railway applications - Track - Acceptance of works - Part 5: Procedures for rail reprofiling in plain line, switches, crossings and expansion devices.* (EN 13231-5:2018).

[11] Bedoya-Zapata, A. D., León-Henao, H., Mesaritis, M., Molina, L. F., Palacio, M., Santa, J. F., Rudas, J. S., Toro, A., and Lewis, R. (2022). White Etching Layer (WEL) formation in different rail grades after grinding operations in the field. *Wear,* 502–503. https://doi.org/10.1016/j.wear.2022.204371

[12] Steyn, E., Paulsson, B., Ekberg, A., and Kabo, E. (2024). Rail machining – current practices and potential for optimisation. Proceedings of the Institution of Mechanical Engineers, *Part F: Journal of Rail and Rapid Transit,* 238(2). https://doi.org/10.1177/09544097231187978

[13] Marich, S. (2009). Managing the wheel-rail interface: the Australian experience. In R. Lewis and U. Olofsson (Eds.), *Wheel-rail interface handbook* (p. 778). Woodhead Publishing Limited.

[14] Sroba, P., and Roney, M. (2003). Rail grinding best practices. Proceedings of the 2003 American Railway Engineering and Maintenance of Way Association Annual Conference.

[15] European Committee for Standardization. (2020). *Railway applications - Track - Acceptance of works - Part 2: Acceptance of reprofiling rails in plain line, switches, crossings and expansion devices.* (EN 13231-2:2020).

[16] Llewellyn, D. T. (1994). *Steels: Metallurgy and Applications* (Second edition). Butterworth-Heineman Ltd.

[17] Moser, A. and Pointner, P. (1992). Head-Hardened Rails Produced from Rolling Heat. *Transportation Research Record*, 1341. 70-74. https://onlinepubs.trb.org/Onlinepubs/trr/1992/1341/1341-008.pdf

[18] ASTM International. (2019). *Standard Hardness Conversion Tables for Metals Relationship Among Brinell Hardness, Vickers Hardness, Rockwell Hardness, Superficial Hardness, Knoop Hardness, Scleroscope Hardness, and Leeb Hardness.* (E140 - 12b (2019)).

[19] Kalpakjian, S. and Schmid S. R. (2006). *Manufacturing Engineering and Technology* (Fifth edition). Pearson Education, Inc.

[20] Mädler, K., Zoll, A., Heyder, R., and Brehmer, M. (2008). *Rail Materials - Alternatives and Limits.* 8th World Congress on Railway Research, May 2008.

[21] Jaeger, J. C., 'Moving Sources of Heat and the Temperature at Sliding Contacts', Proceedings of the Royal Society of New South Wales, 76, 1942, p. 203.

[22] Malkin, S., Guo, C. (2008). *Grinding Technology: Theory and Applications of Machining with Abrasives.* Industrial Press Inc., New York

[23] Mackenzie, D.. (2017). Metallurgical Reasons for Grinding Cracks and Their Detection. *Gear Solutions* 25. https://www.researchgate.net/publication/318467909

[24] Badger, J. A., and Torrance, A. (2000). Burn awareness. Cutting Tool Engineering, 52(12).

[25] Krauss, G. (1999). Martensite in steel: Strength and structure. *Materials Science and Engineering: A,* 273–275. https://doi.org/10.1016/s0921-5093(99)00288-9

[26] Uhlmann, E., Lypovka, P., Hochschild, L., and Schröer, N. (2016). Influence of rail grinding process parameters on rail surface roughness and surface layer hardness. *Wear,* 366–367. https://doi.org/10.1016/j.wear.2016.03.023

[27] Zhou, K., Ding, H., Steenbergen, M., Wang, W., Guo, J., and Liu, Q. (2021). Temperature field and material response as a function of rail grinding parameters. *International Journal of Heat and Mass Transfer,* 175. https://doi.org/10.1016/j.ijheatmasstransfer.2021.121366

[28] Tung, P. Y., Zhou, X., Morsdorf, L., and Herbig, M. (2022). Formation mechanism of brown etching layers in pearlitic rail steel. *Materialia,* 26. https://doi.org/10.1016/j.mtla.2022.101625

[29] Li, S., Wu, J., Petrov, R. H., Li, Z., Dollevoet, R., and Sietsma, J. (2016). "Brown etching layer": A possible new insight into the crack initiation

of rolling contact fatigue in rail steels? *Engineering Failure Analysis,* 66. https://doi.org/10.1016/j.engfailanal.2016.03.019

[30] Qi, H. S., Rowe, W. B., and Mills, B. (1997). Experimental investigation of contact behaviour in grinding. *Tribology International,* 30(4). https://doi.org/10.1016/S0301-679X(96)00057-6

A

Results from finite element simulations

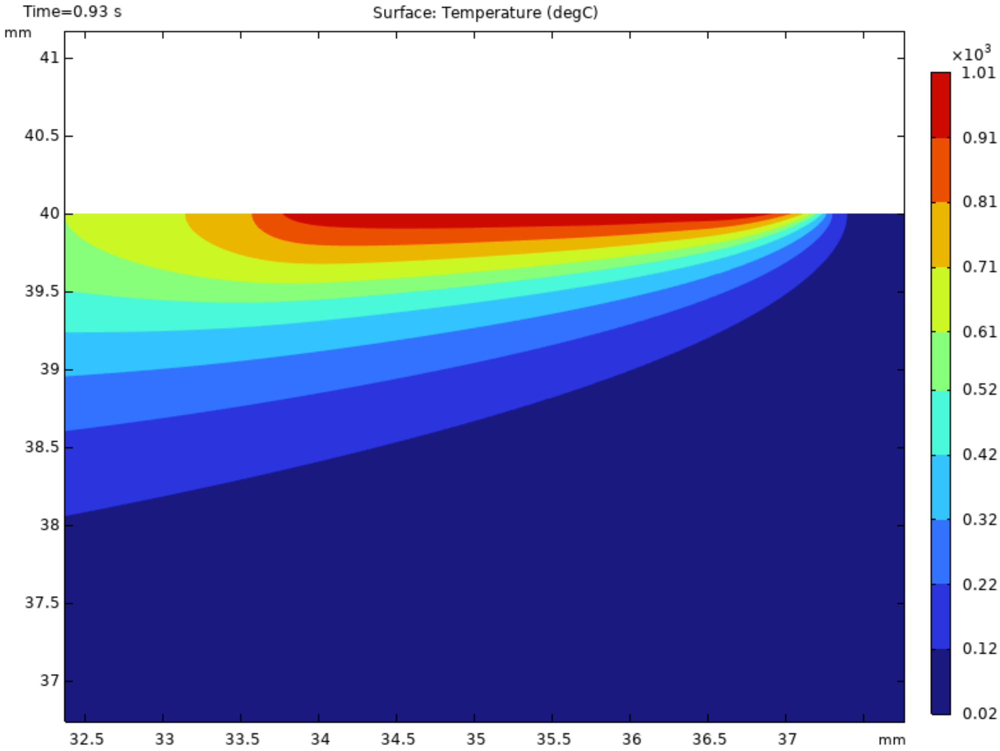

Figure A.1: Feedrate: 2500 mm/min, depth of cut: 0.03 mm, Material: R260

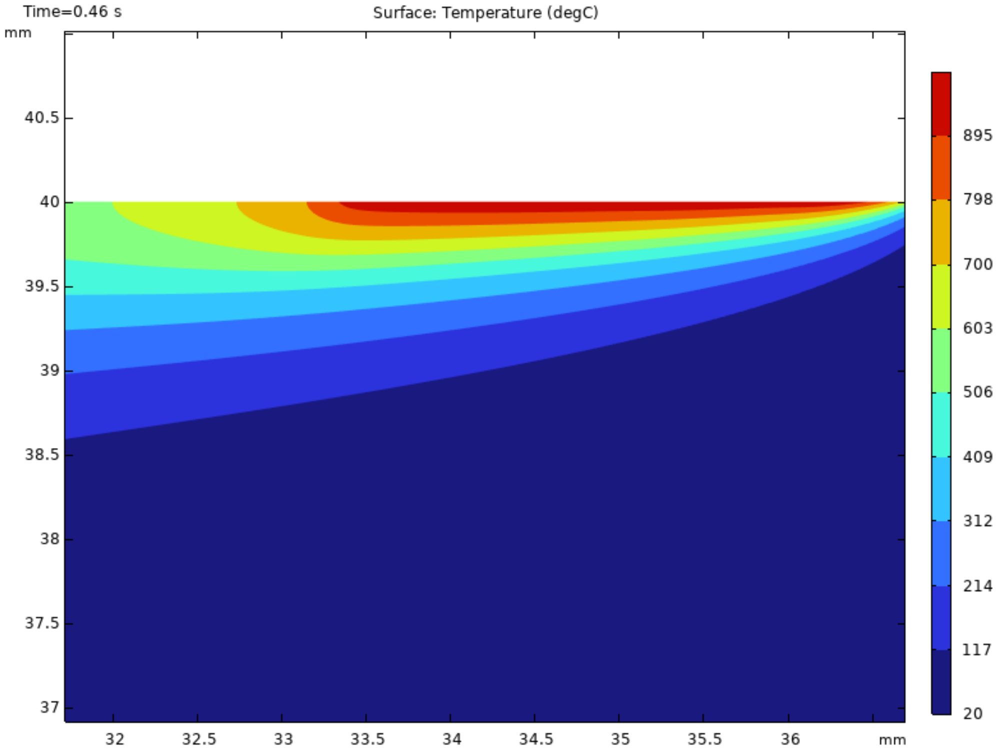

Figure A.2: Feedrate: 5000 mm/min, depth of cut: 0.03 mm, Material: R260

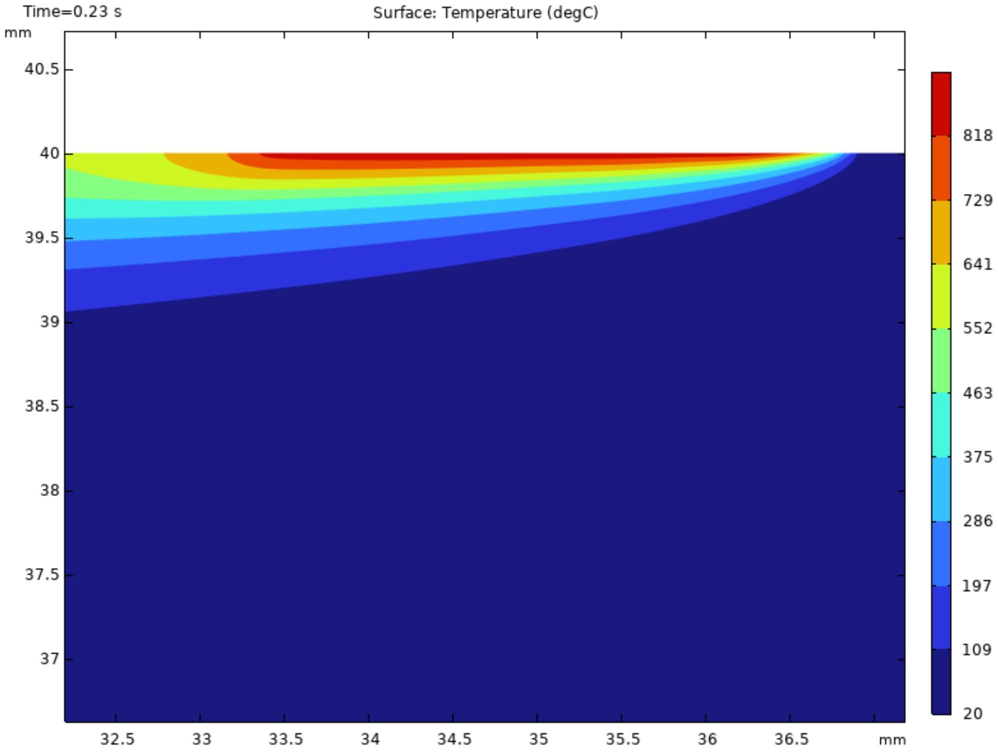

Figure A.3: Feedrate: 10000 mm/min, depth of cut: 0.03 mm, Material: R260

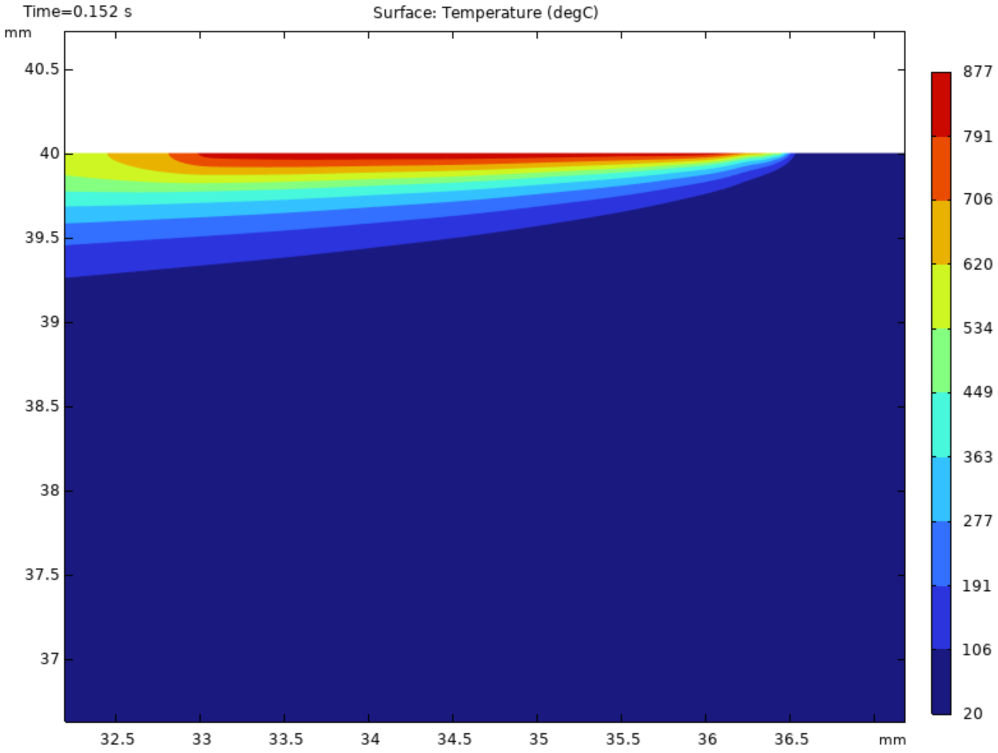

Figure A.4: Feedrate: 15000 mm/min, depth of cut: 0.03 mm, Material: R260

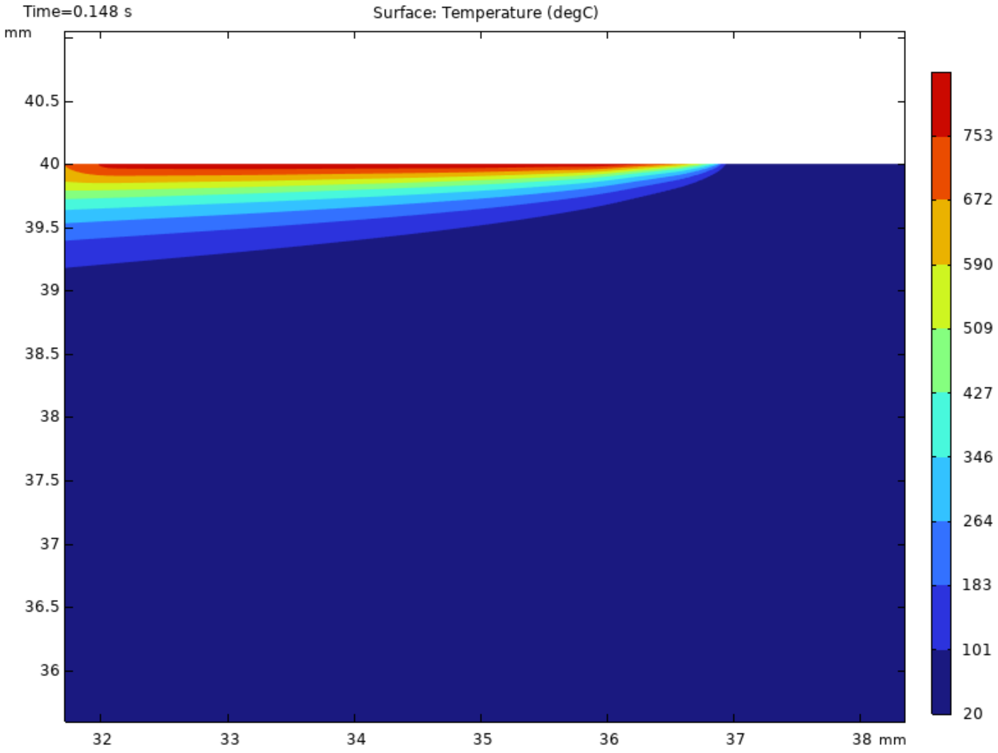

Figure A.5: Feedrate: 15000 mm/min, depth of cut: 0.06 mm, Material: R260

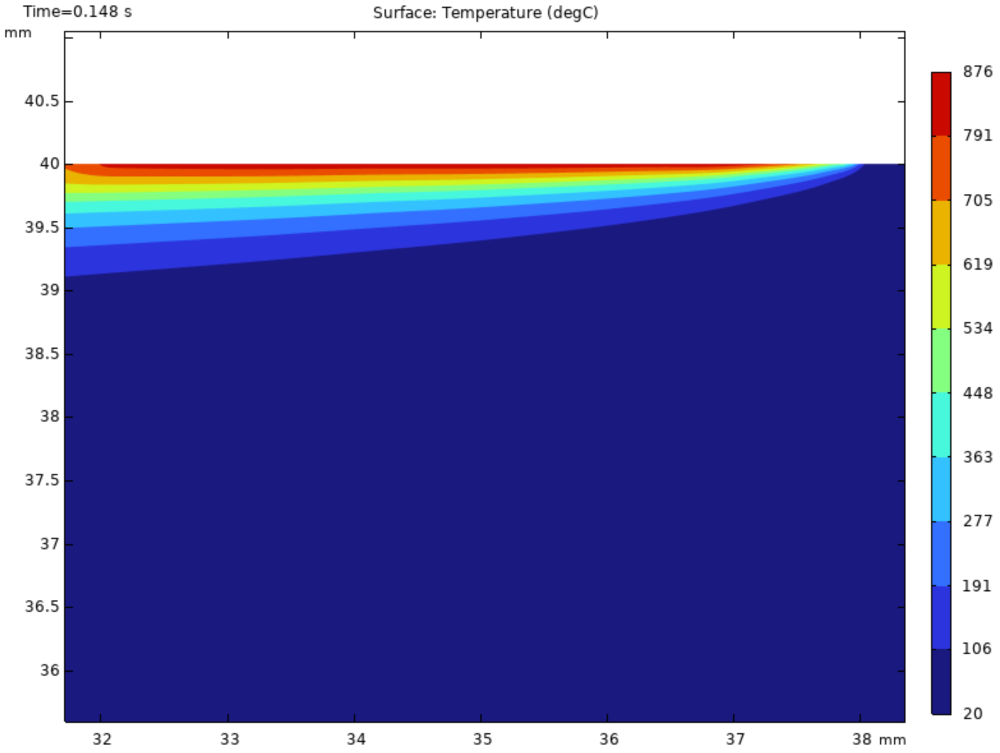

Figure A.6: Feedrate: 15000 mm/min, depth of cut: 0.09 mm, Material: R260

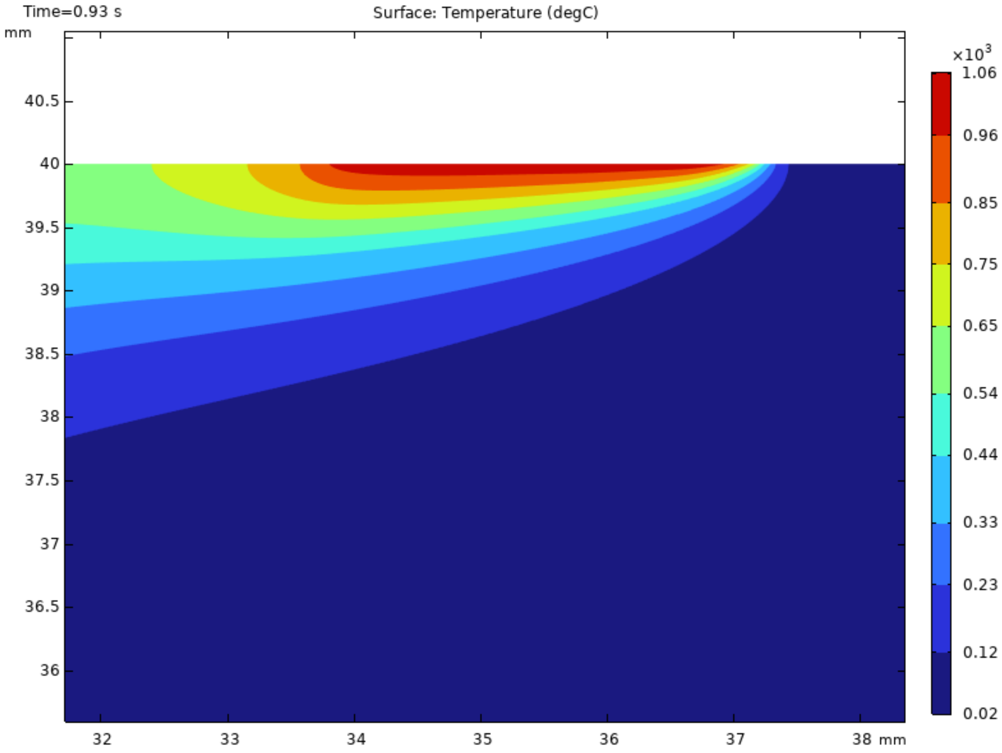

Figure A.7: Feedrate: 2500 mm/min, depth of cut: 0.03 mm, Material: R350HT

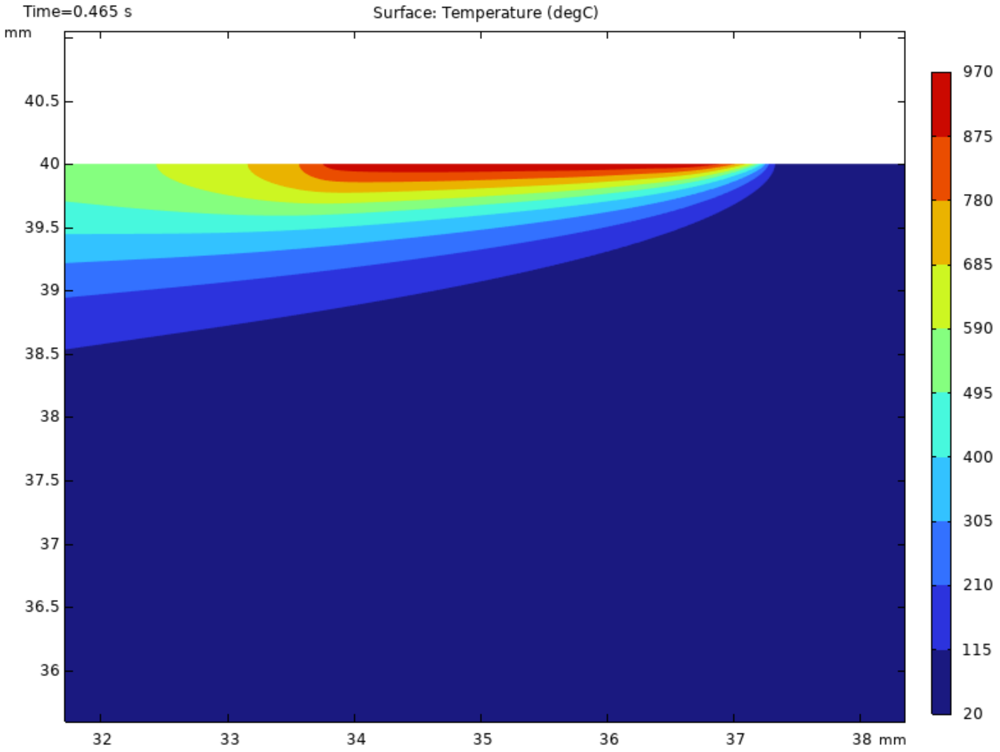

Figure A.8: Feedrate: 5000 mm/min, depth of cut: 0.03 mm, Material: R350HT

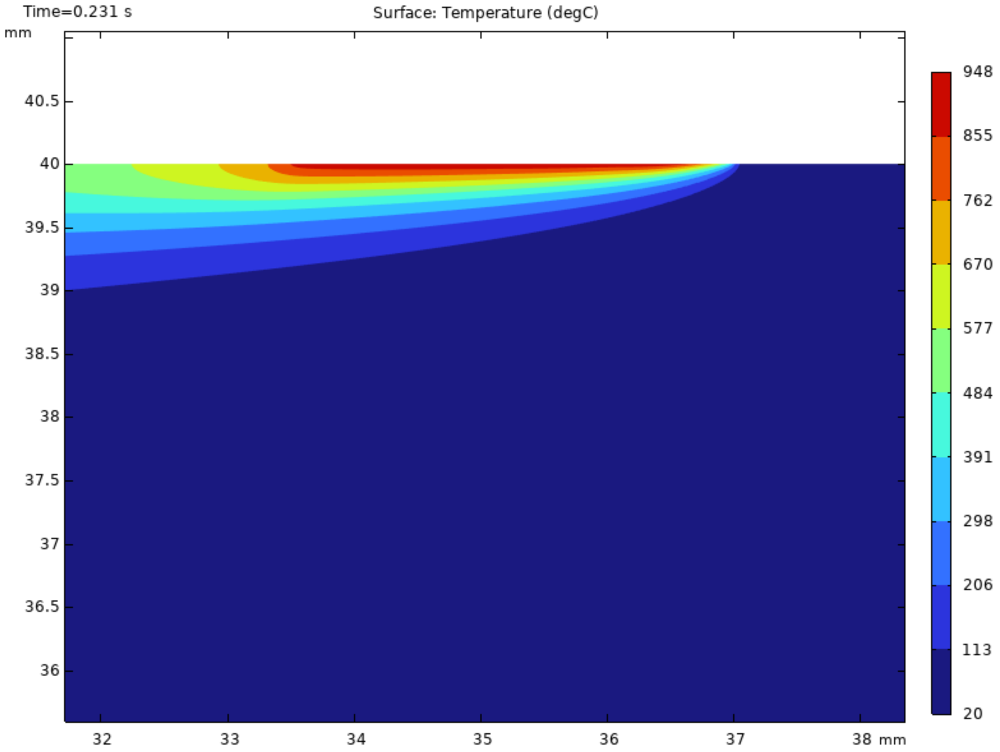

Figure A.9: Feedrate: 10000 mm/min, depth of cut: 0.03 mm, Material: R350HT

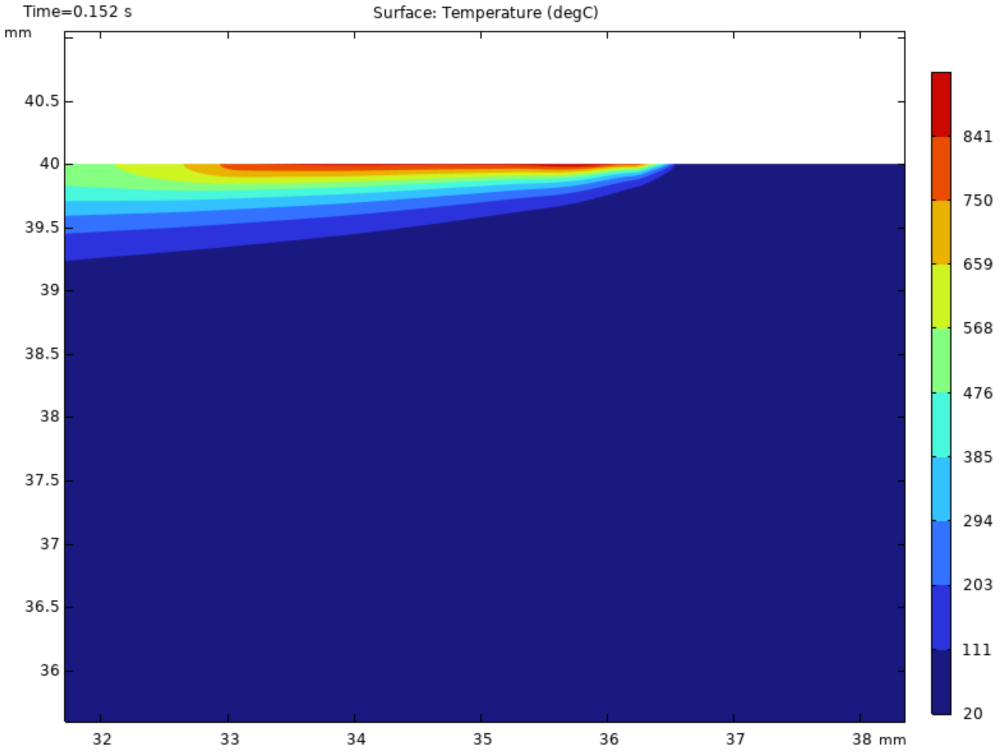

Figure A.10: Feedrate: 15000 mm/min, depth of cut: 0.03 mm, Material: R350HT

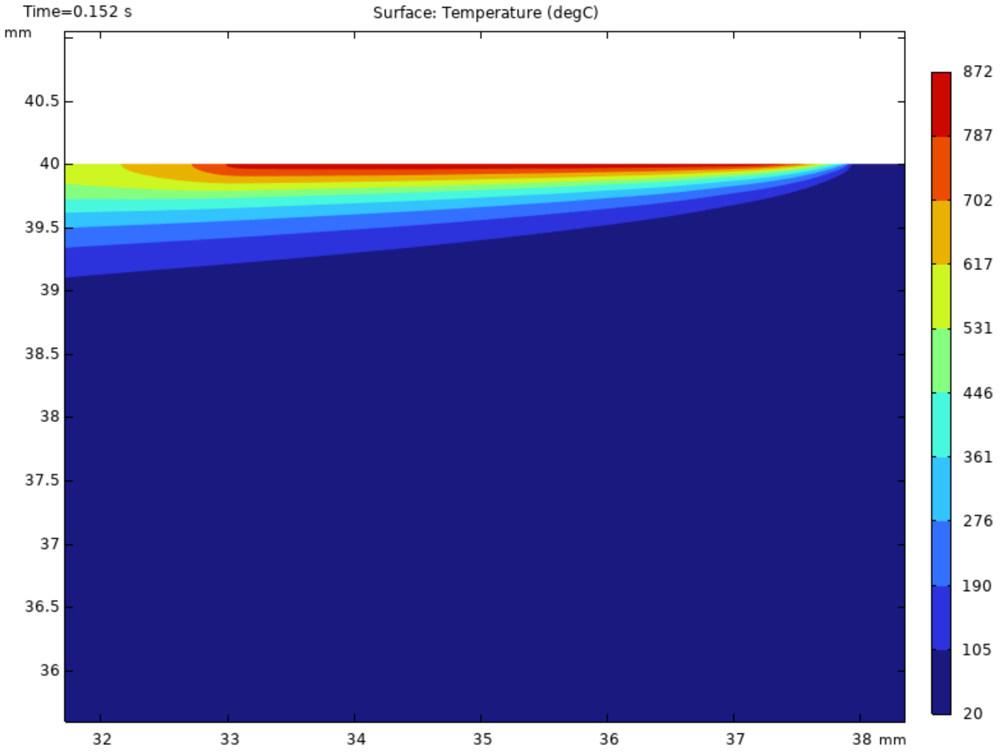

Figure A.11: Feedrate: 15000 mm/min, depth of cut: 0.06 mm, Material: R350HT

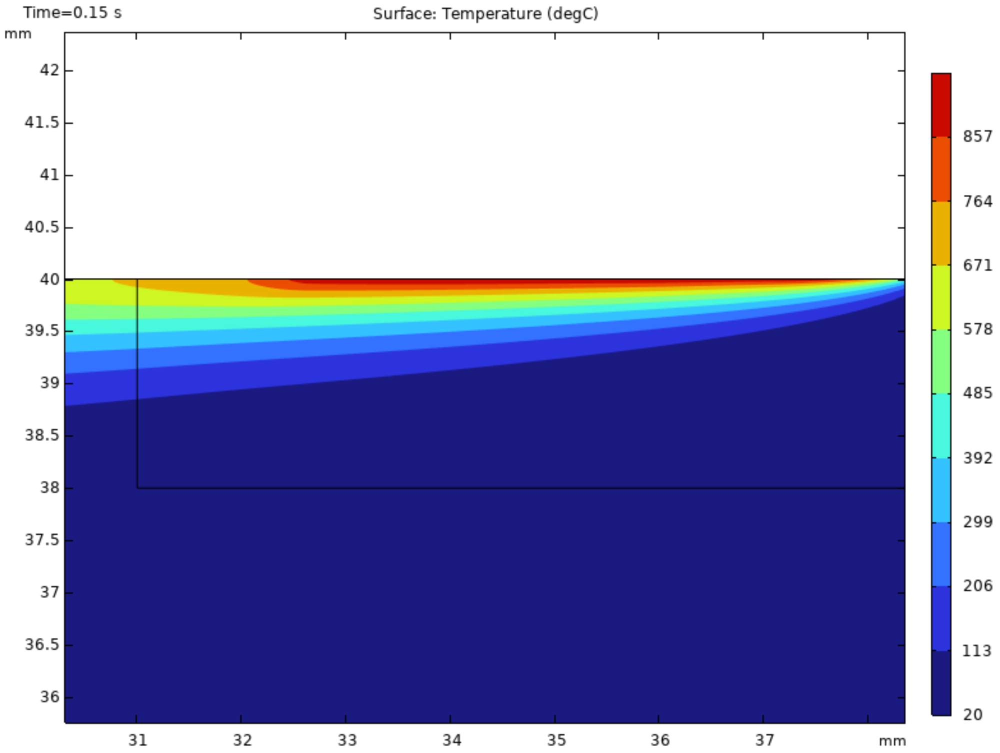

Figure A.12: Feedrate: 15000 mm/min, depth of cut: 0.09 mm, Material: R350HT

B

Results from analytical calculations

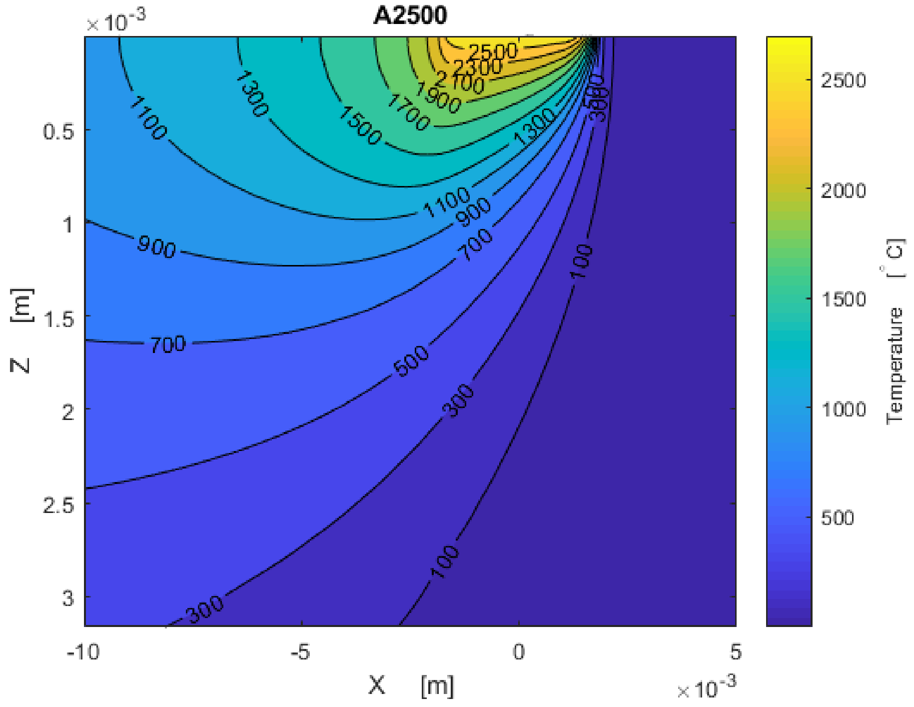

Figure B.1: Feedrate: 2500 mm/min, depth of cut: 0.03 mm, material: R260, Power given by the grinding machine.

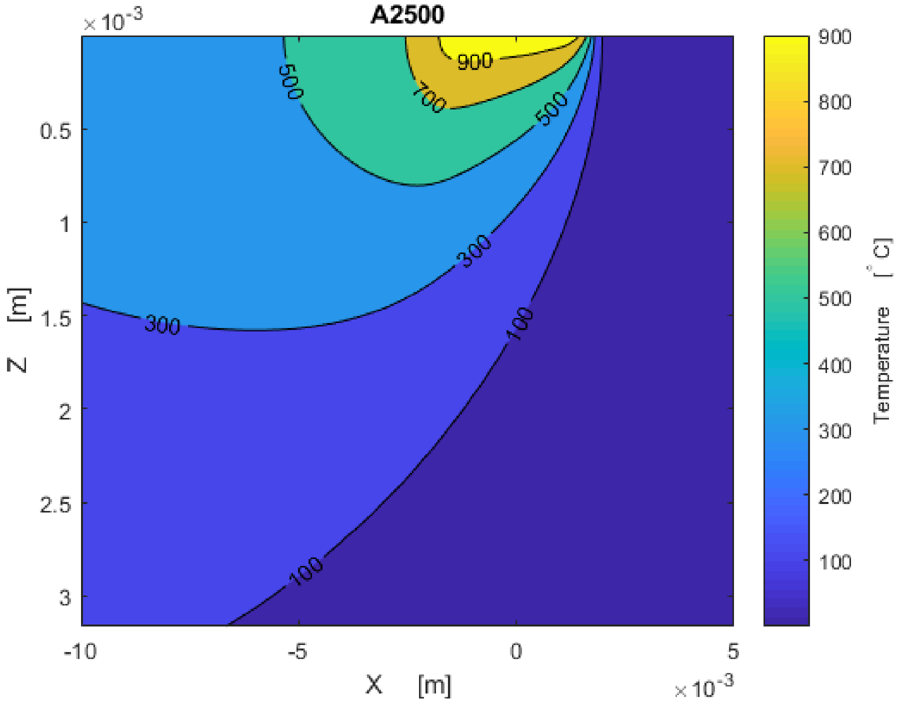

Figure B.2: Feedrate: 2500 mm/min, depth of cut: 0.03 mm, material: R260, Power adjusted to match martensite depth.

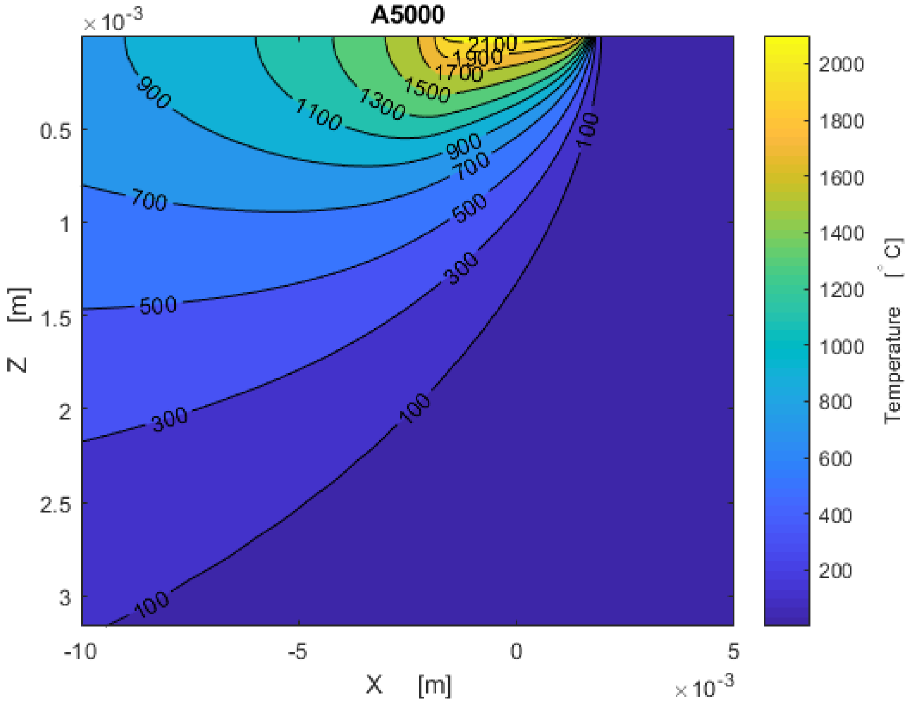

Figure B.3: Feedrate: 5000 mm/min, depth of cut: 0.03 mm, material: R260, Power given by the grinding machine.

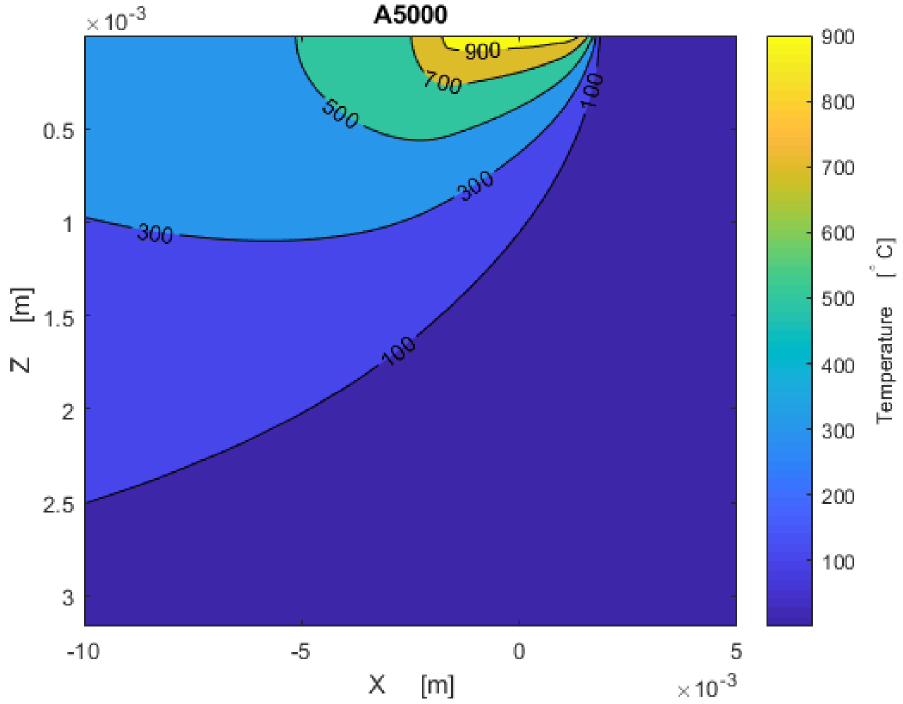

Figure B.4: Feedrate: 5000 mm/min, depth of cut: 0.03 mm, material: R260, Power adjusted to match martensite depth.

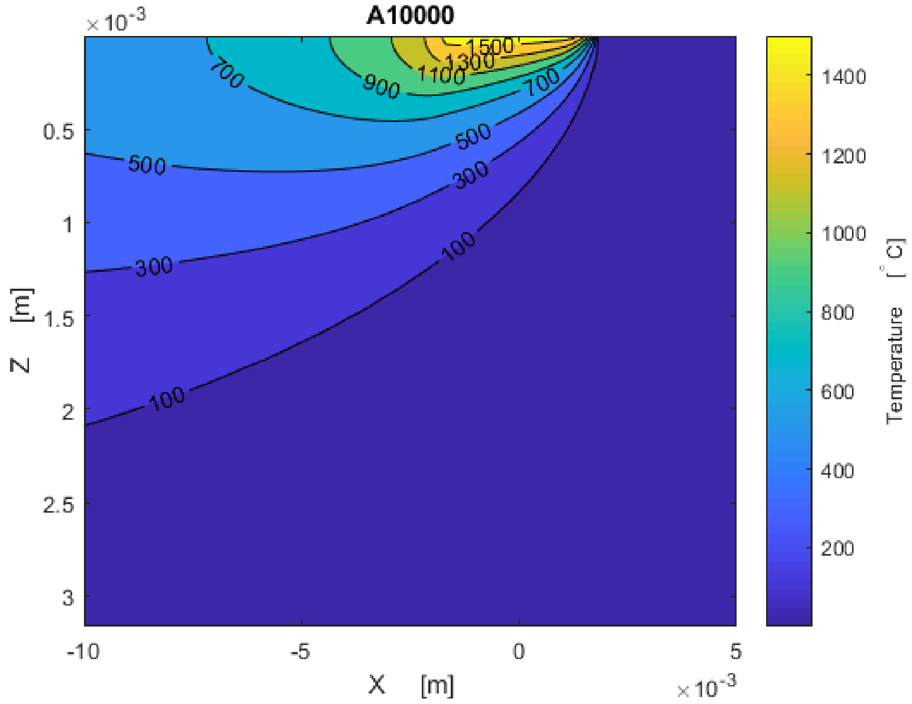

Figure B.5: Feedrate: 10000 mm/min, depth of cut: 0.03 mm, material: R260, Power given by the grinding machine.

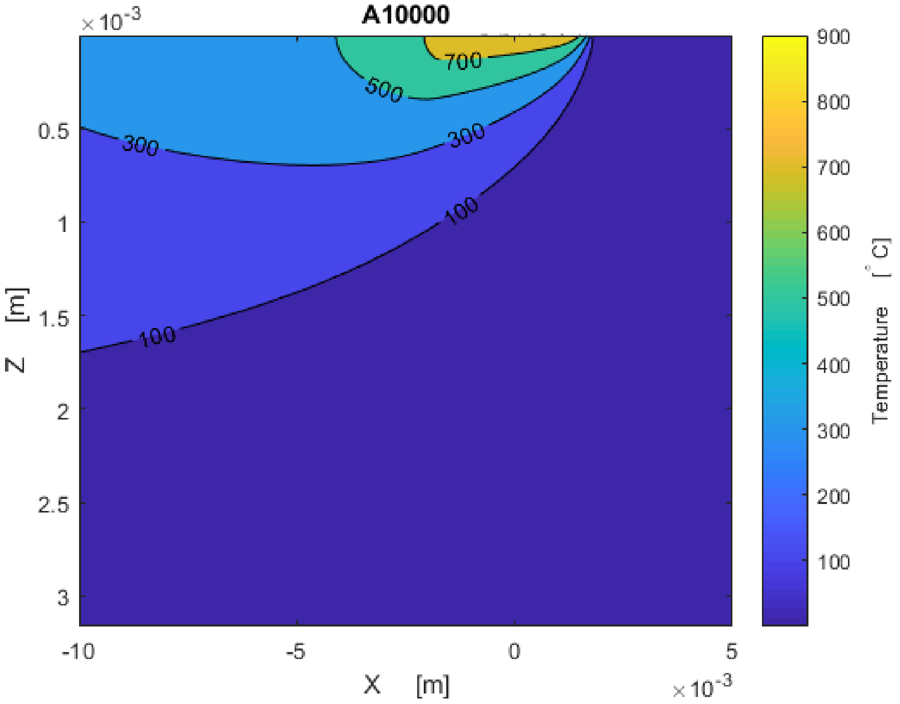

Figure B.6: Feedrate: 10000 mm/min, depth of cut: 0.03 mm, material: R260, Power adjusted to match martensite depth.

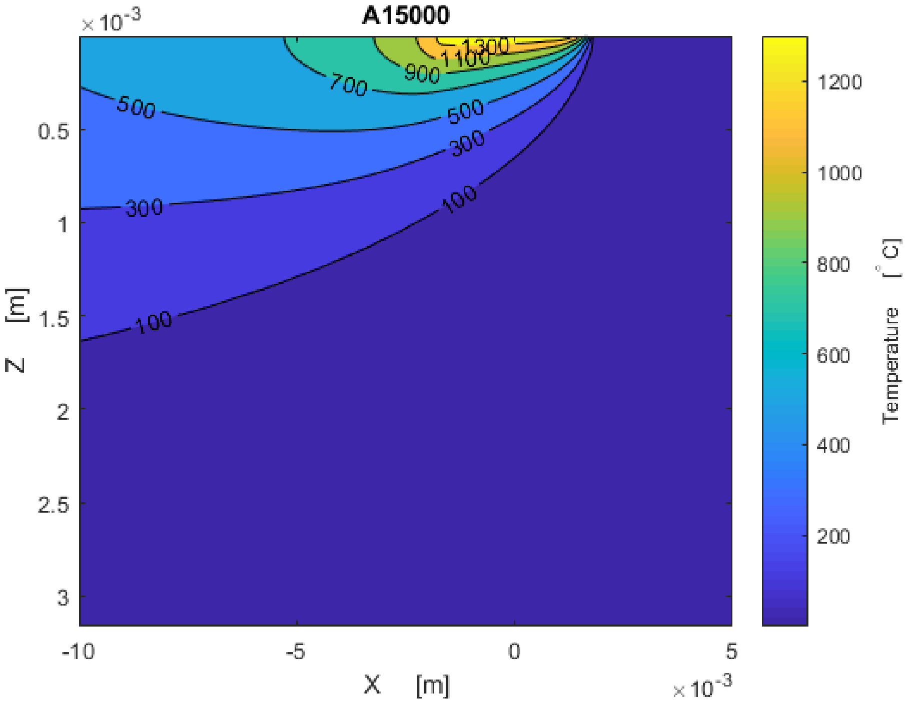

Figure B.7: Feedrate: 15000 mm/min, depth of cut: 0.03 mm, material: R260, Power given by the grinding machine.

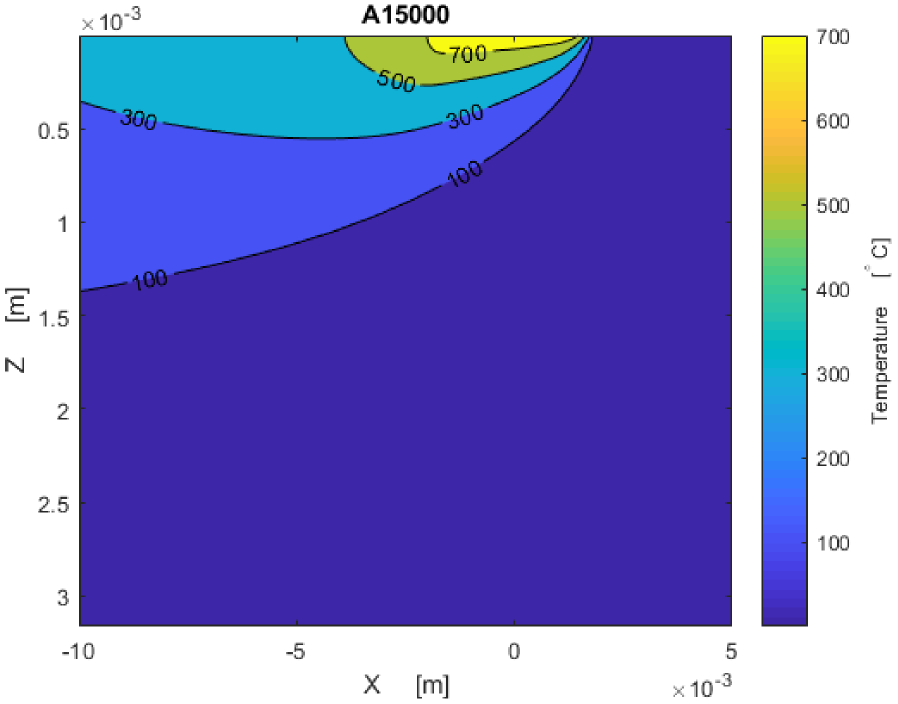

Figure B.8: Feedrate: 15000 mm/min, depth of cut: 0.03 mm, material: R260, Power adjusted to match martensite depth.

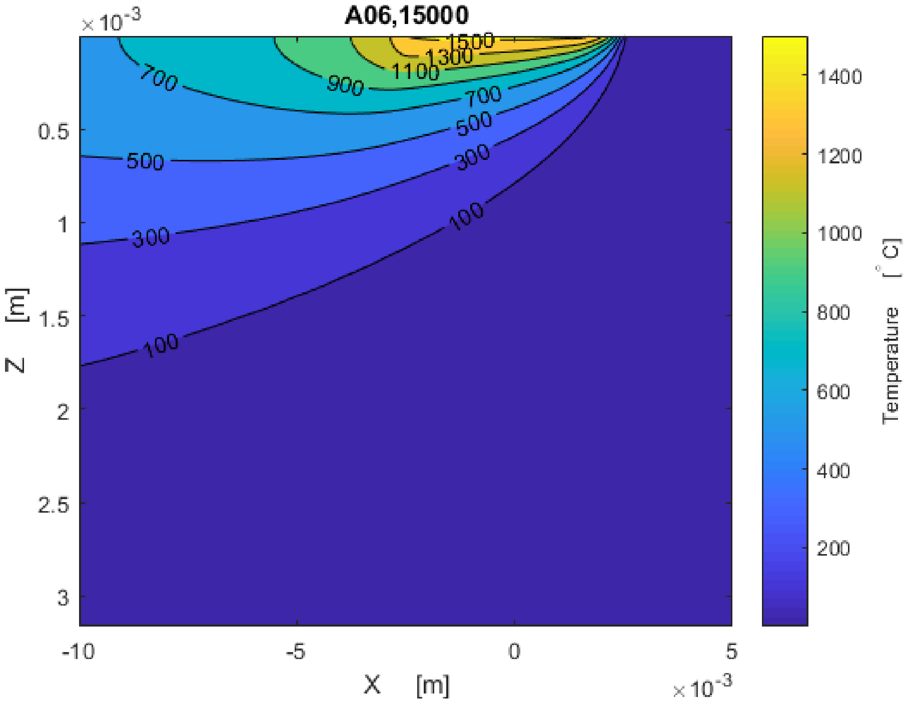

Figure B.9: Feedrate: 15000 mm/min, depth of cut: 0.06 mm, material: R260, Power given by the grinding machine.

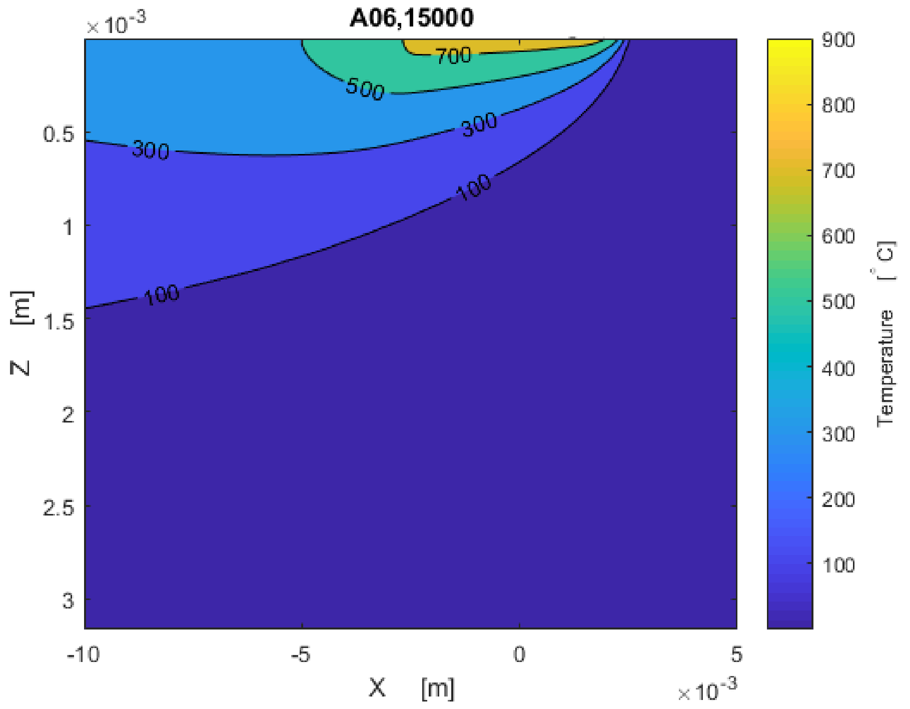

Figure B.10: Feedrate: 15000 mm/min, depth of cut: 0.06 mm, material: R260, Power adjusted to match martensite depth.

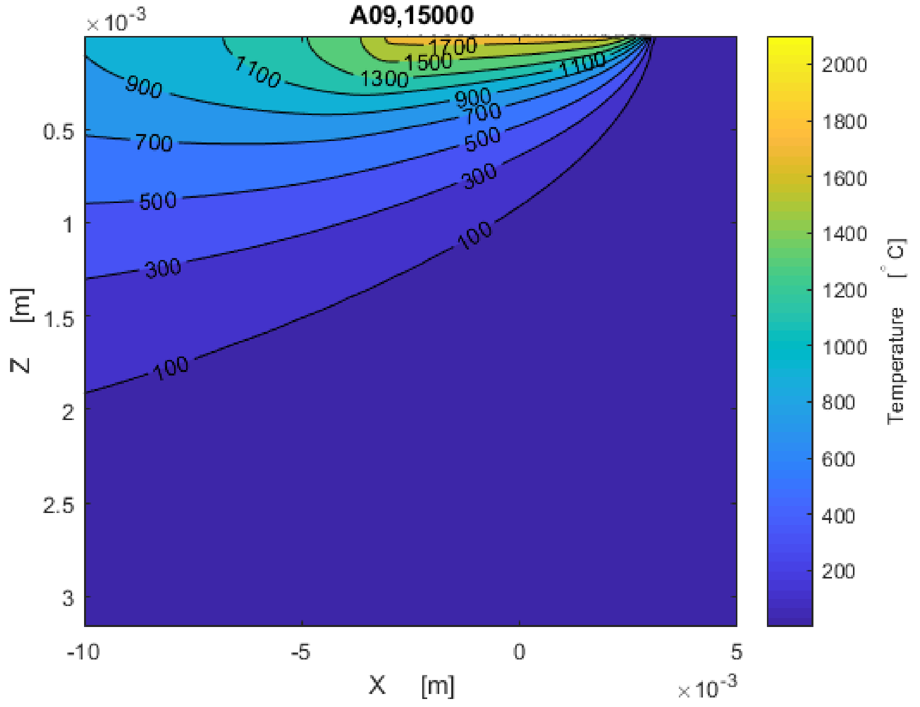

Figure B.11: Feedrate: 15000 mm/min, depth of cut: 0.09 mm, material: R260, Power given by the grinding machine.

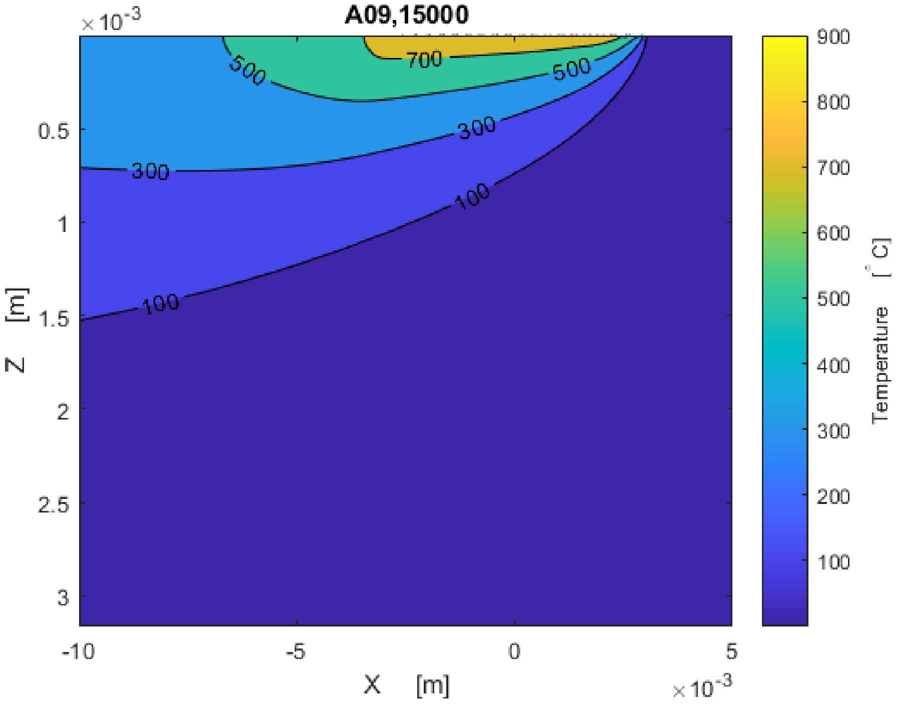

Figure B.12: Feedrate: 15000 mm/min, depth of cut: 0.09 mm, material: R260, Power adjusted to match martensite depth.

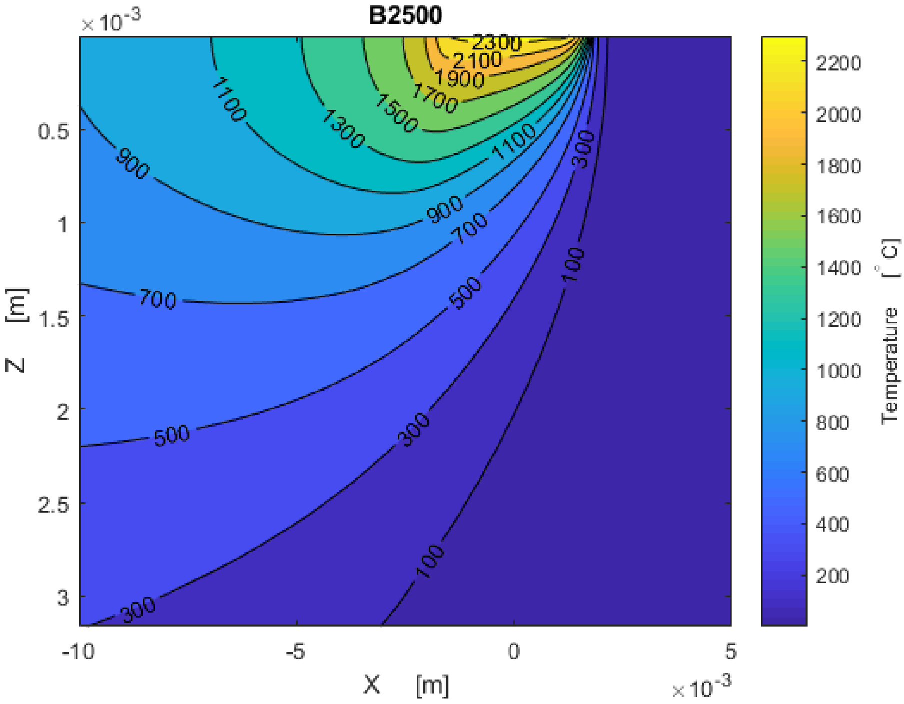

Figure B.13: Feedrate: 2500 mm/min, depth of cut: 0.03 mm, material: R350HT, Power given by the grinding machine.

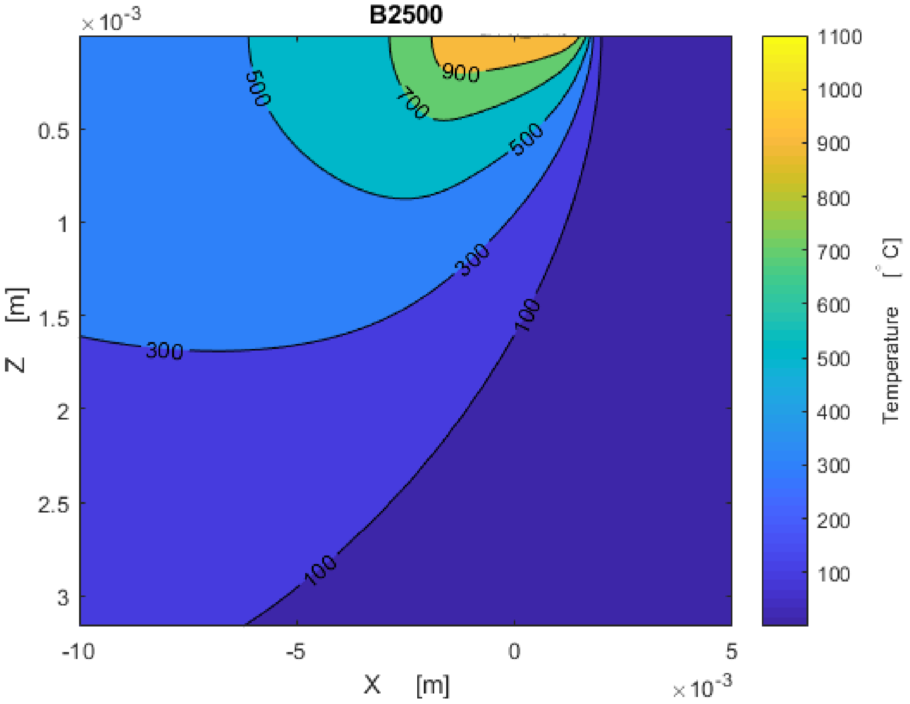

Figure B.14: Feedrate: 2500 mm/min, depth of cut: 0.03 mm, material: R350HT, Power adjusted to match martensite depth.

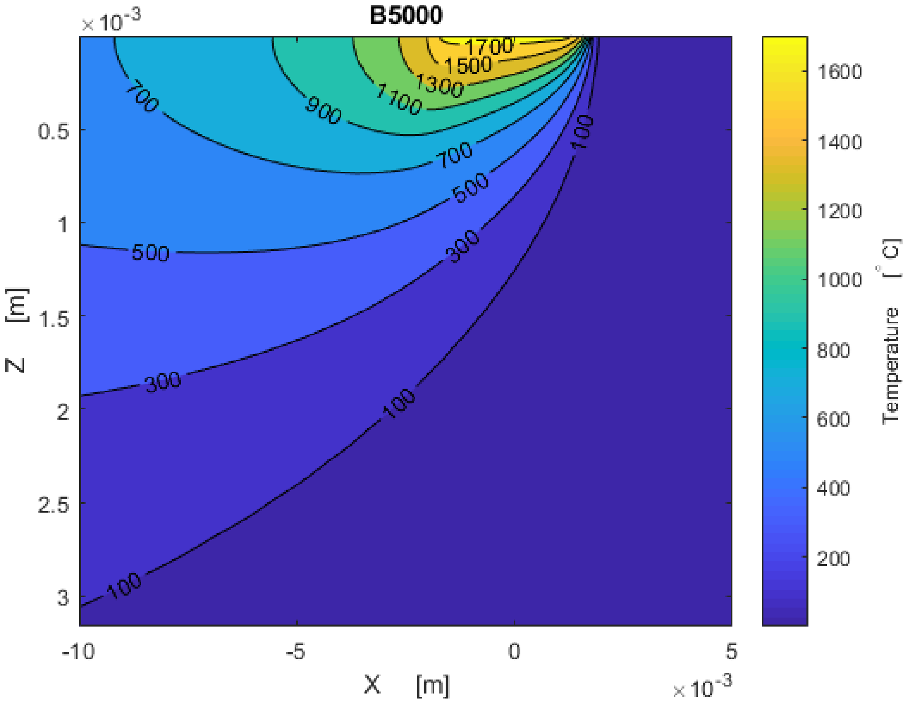

Figure B.15: Feedrate: 5000 mm/min, depth of cut: 0.03 mm, material: R350HT, Power given by the grinding machine.

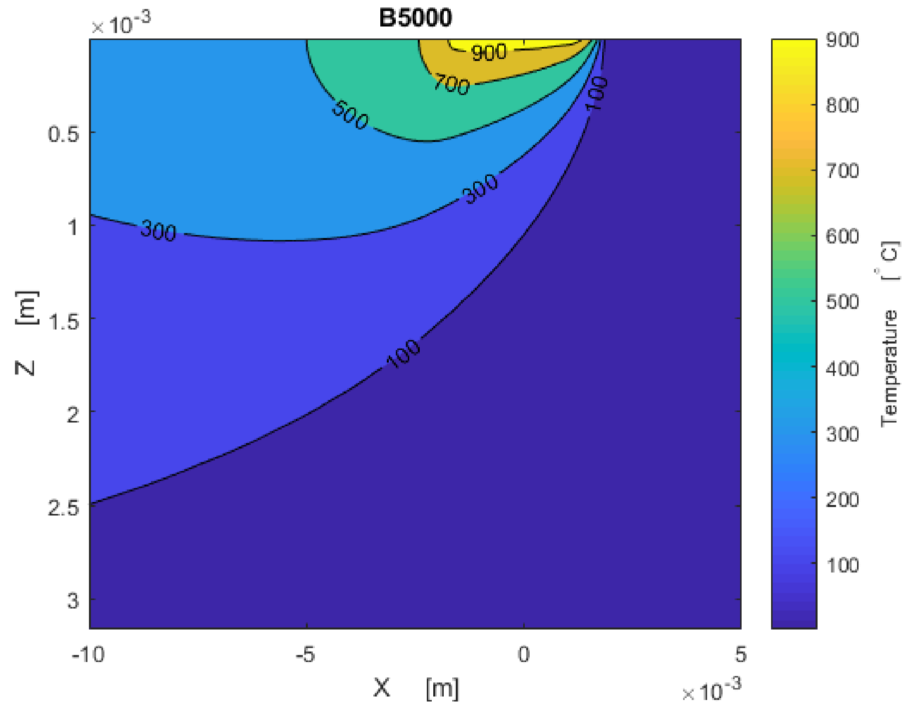

Figure B.16: Feedrate: 5000 mm/min, depth of cut: 0.03 mm, material: R350HT, Power adjusted to match martensite depth.

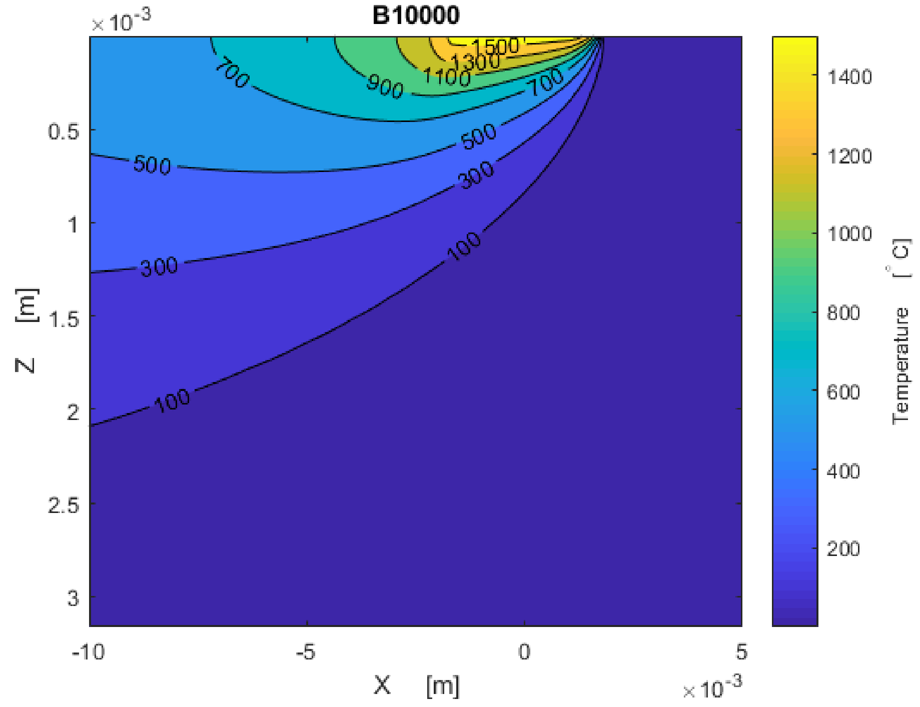

Figure B.17: Feedrate: 10000 mm/min, depth of cut: 0.03 mm, material: R350HT, Power given by the grinding machine.

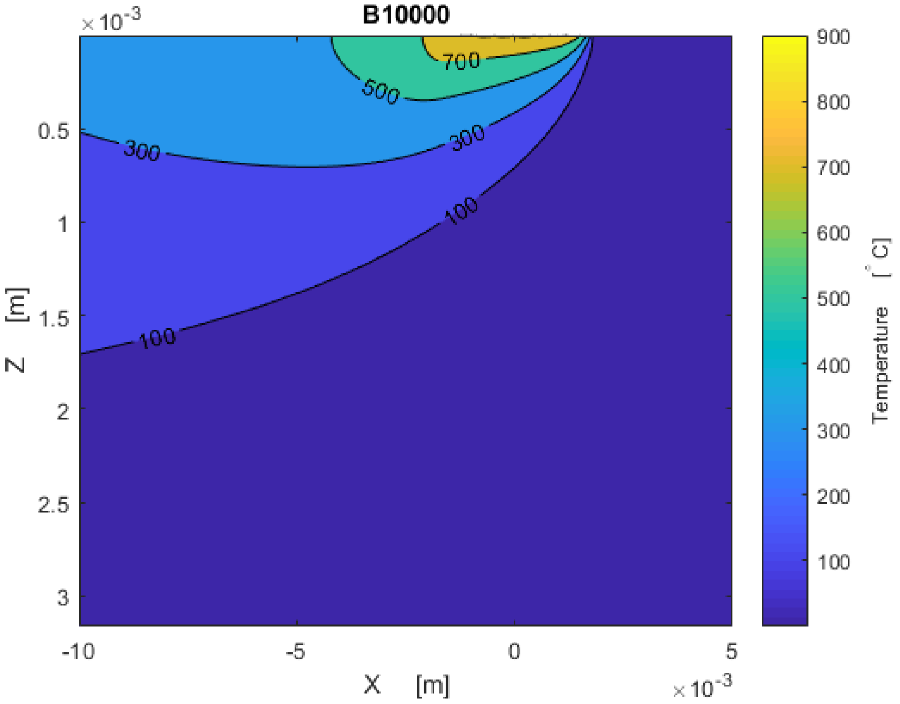

Figure B.18: Feedrate: 10000 mm/min, depth of cut: 0.03 mm, material: R350HT, Power adjusted to match martensite depth.

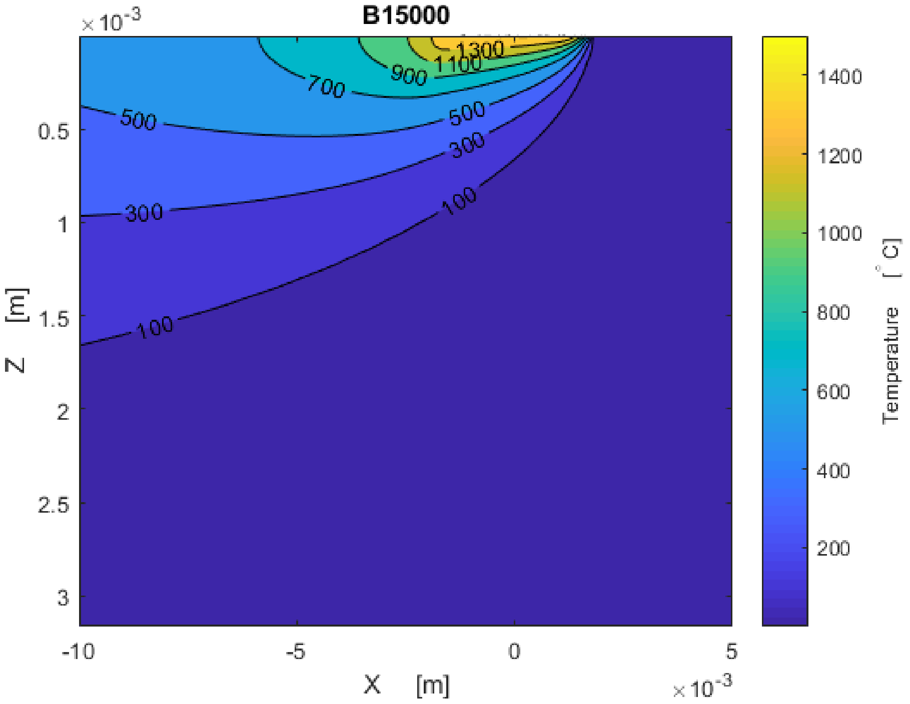

Figure B.19: Feedrate: 15000 mm/min, depth of cut: 0.03 mm, material: R350HT, Power given by the grinding machine.

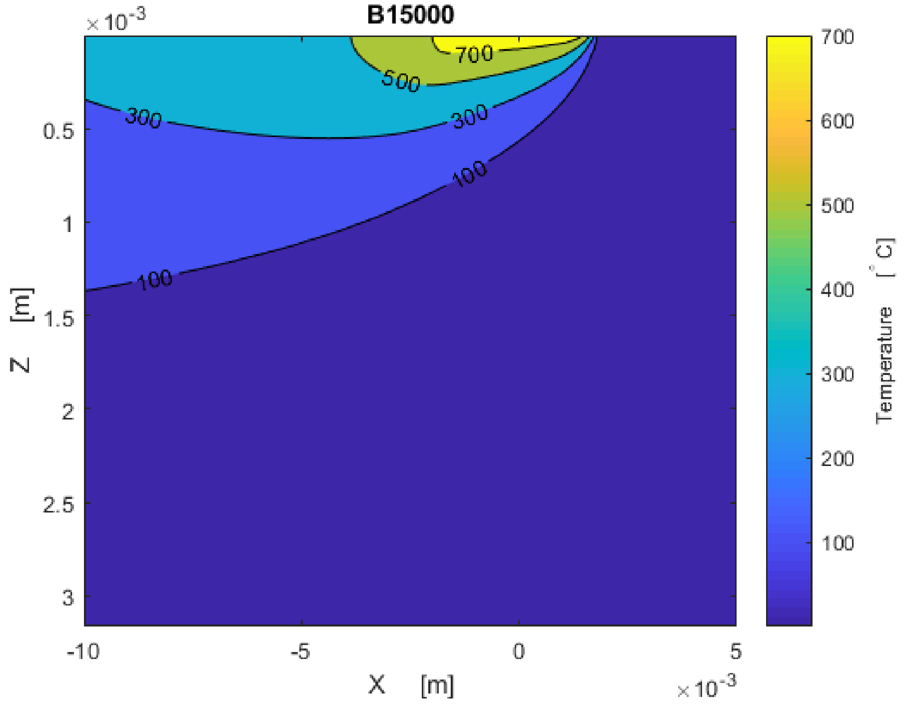

Figure B.20: Feedrate: 15000 mm/min, depth of cut: 0.03 mm, material: R350HT, Power adjusted to match martensite depth.

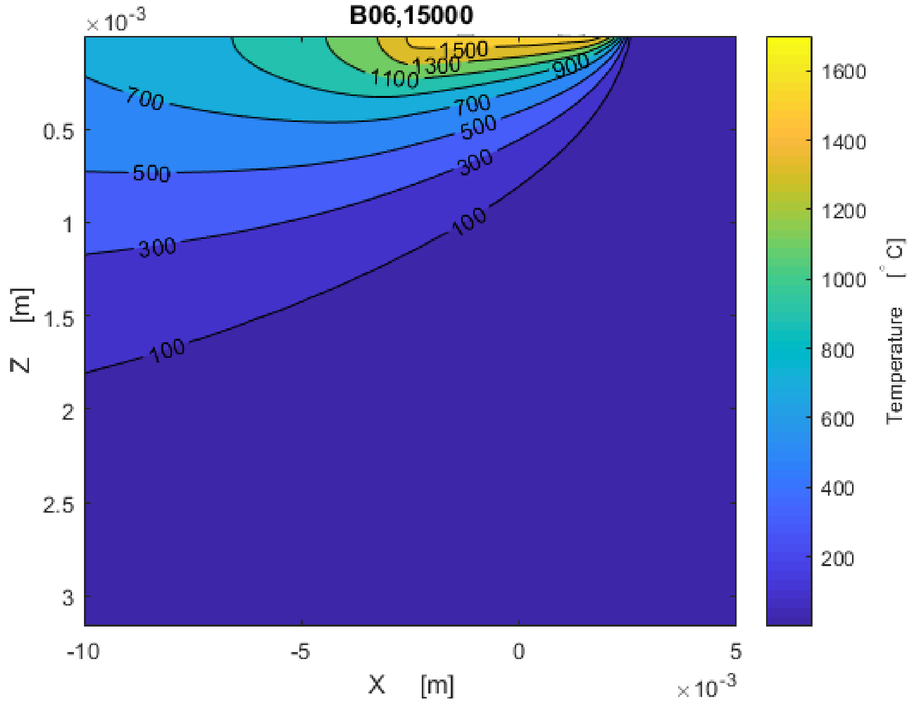

Figure B.21: Feedrate: 15000 mm/min, depth of cut: 0.06 mm, material: R350HT, Power given by the grinding machine.

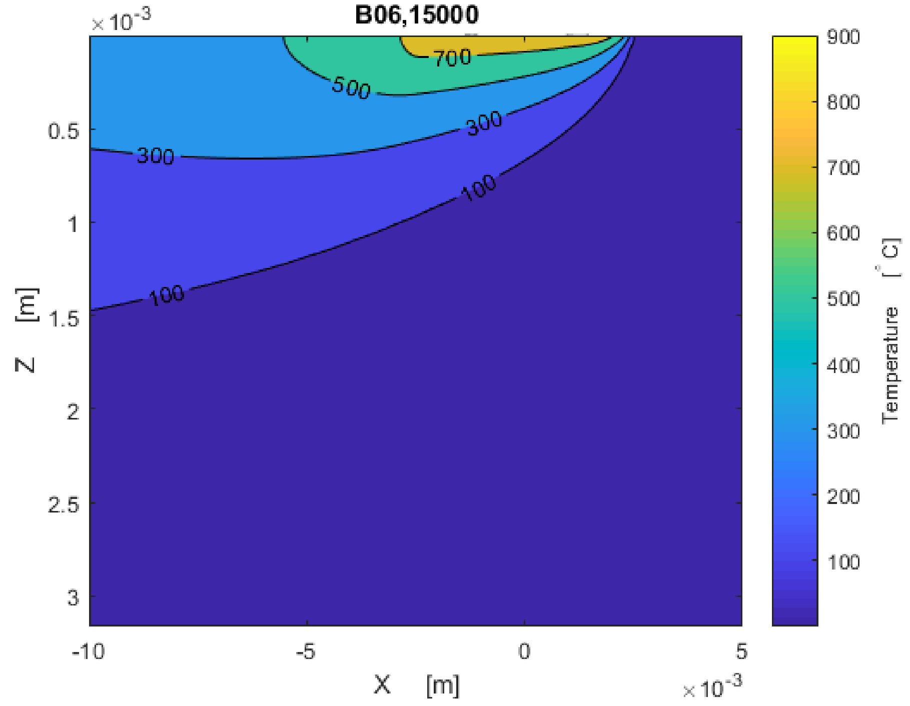

Figure B.22: Feedrate: 15000 mm/min, depth of cut: 0.06 mm, material: R350HT, Power adjusted to match martensite depth.

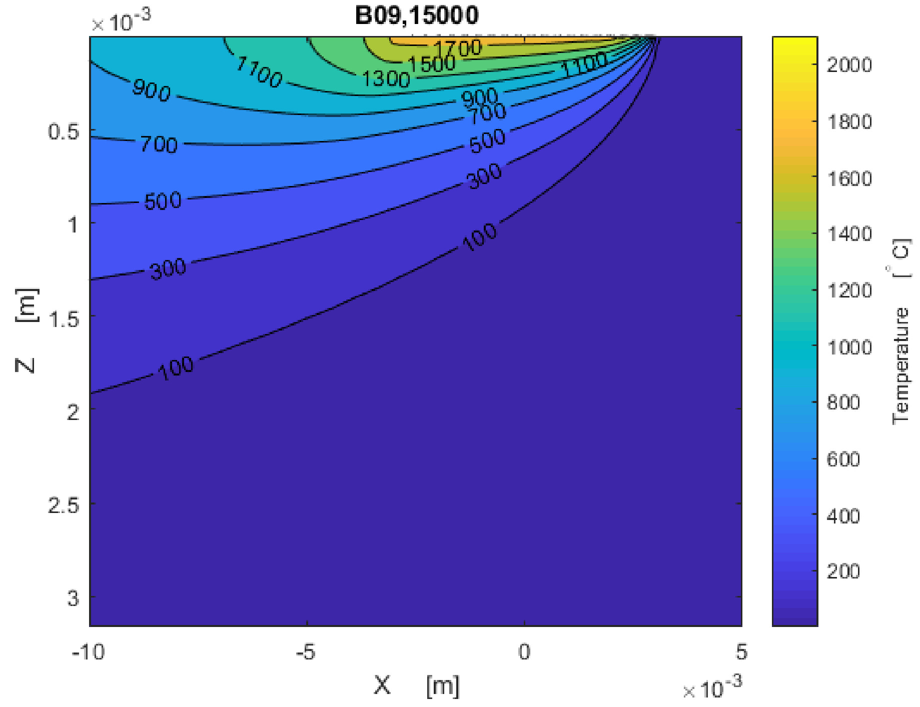

Figure B.23: Feedrate: 15000 mm/min, depth of cut: 0.09 mm, material: R350HT, Power given by the grinding machine.

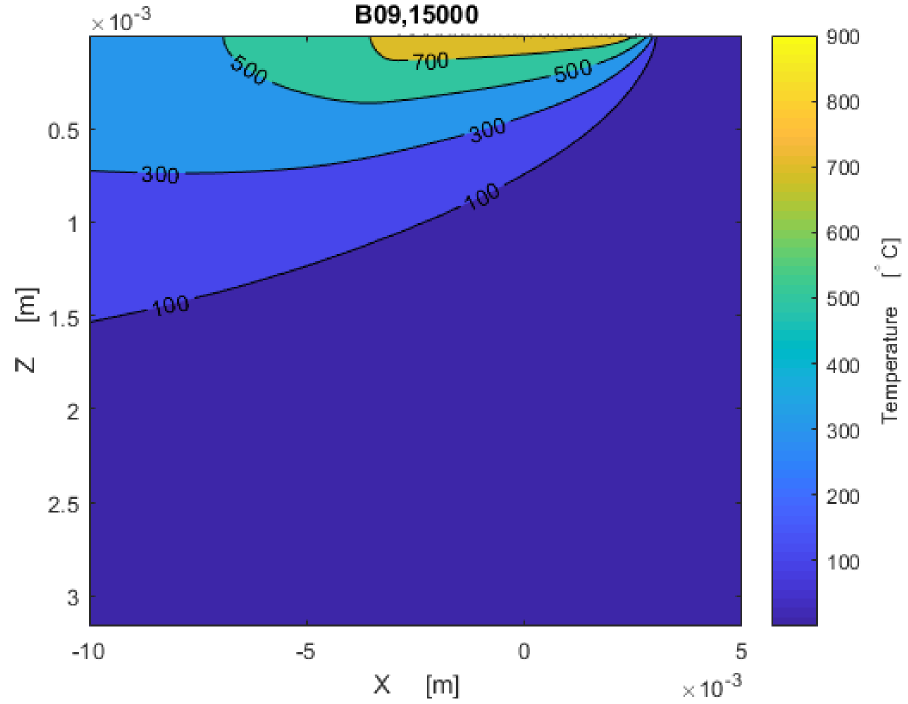

Figure B.24: Feedrate: 15000 mm/min, depth of cut: 0.09 mm, material: R350HT, Power adjusted to match martensite depth.

C

Hardness test on faceted samples

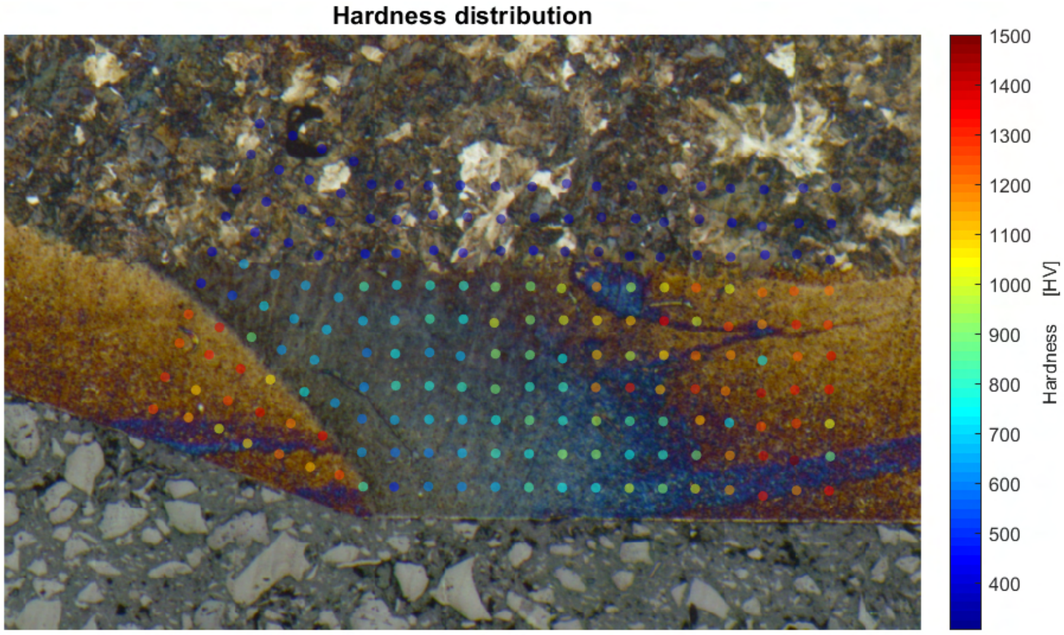

Figure C.1: Feedrate: 2500 mm/min, Depth of cut: 0.03 mm, Material: R260

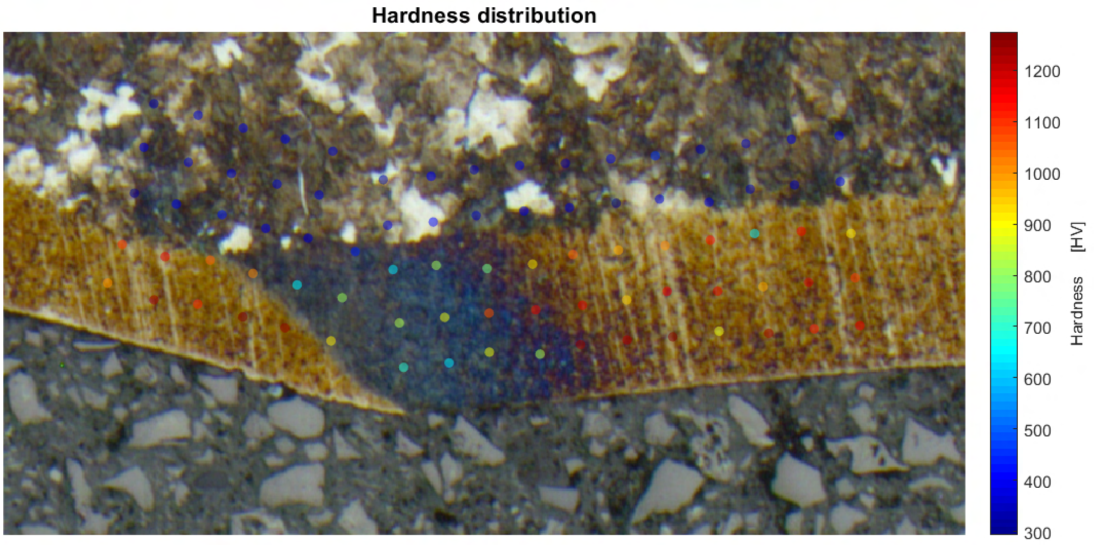

Figure C.2: Feedrate: 15000 mm/min, Depth of cut: 0.09 mm, Material: R260

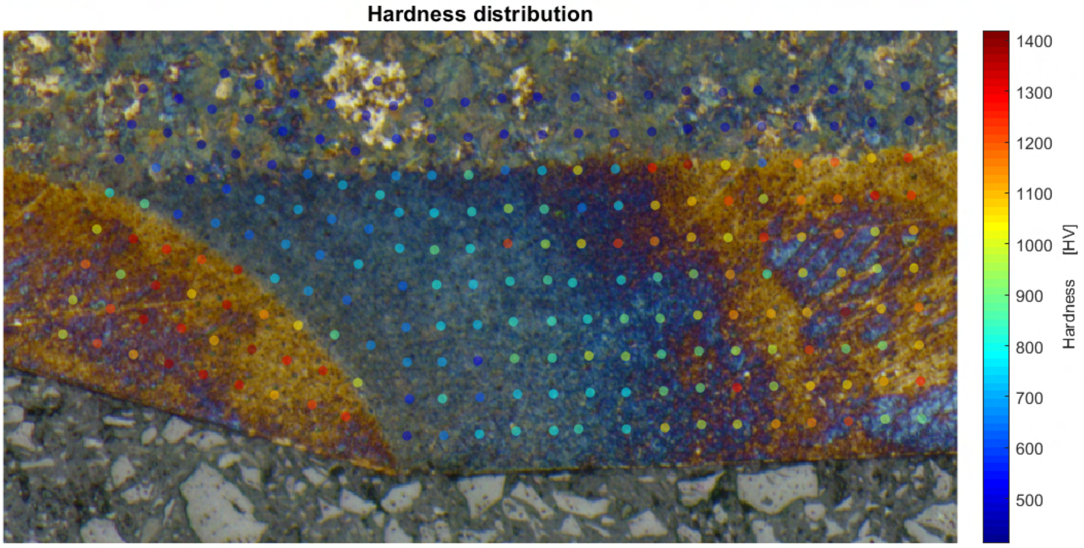

Figure C.3: Feedrate: 2500 mm/min, Depth of cut 0.03 mm, Material: R350HT

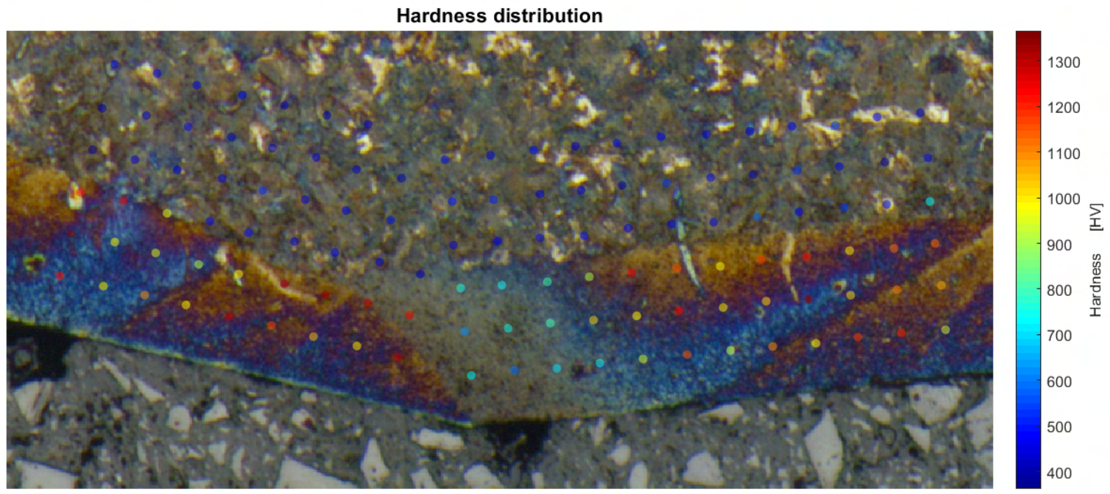

Figure C.4: Feedrate: 15000 mm/min, Depth of cut 0.09 mm, Material: R350HT

CHALMERS UNIVERSITY OF TECHNOLOGY
Gothenburg, Sweden
www.chalmers.se

CHALMERS
UNIVERSITY OF TECHNOLOGY